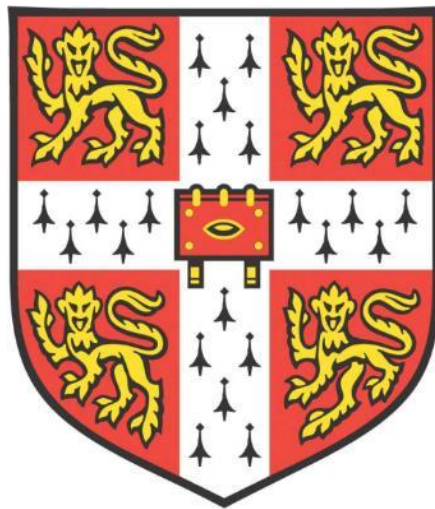


# IONIC CONTROL OF PORIN PERMEABILITY



Santiago Caño Muñiz

Gonville and Caius College

Molecular Immunity Unit, University of Cambridge

Department of Genetics, University of Cambridge

This dissertation is submitted for the degree of Doctor of Philosophy

April 2022



## **DECLARATION**

This dissertation is the result of my own work and includes nothing, which is the outcome of work done in collaboration except where specifically indicated in the text. It has not been previously submitted, in part or whole, to any university or institution for any degree, diploma, or other qualification.

In accordance with the Department of Medicine guidelines, this thesis does not exceed 60,000 words, and it contains less than 150 figures.

Signed: [Signature redacted]

Date: 19 / 04 / 2022

Santiago Caño Muñiz

Cambridge, United Kingdom

## **ABSTRACT**

Porins are transmembrane proteins within the outer membrane of gram-negative bacteria that allow nutrients, and small molecules, including antibiotics, to enter the cell. Electrophysiological studies on porins reconstituted in lipid bilayers have suggested a dynamic regulation of porin conductance through changes in the ionic environment. Thus, this thesis focuses on understanding porin permeability regulation in live bacteria, employing *Escherichia coli* as a model organism.

Firstly, using a flow cytometric method that I developed, I showed that the uptake of a fluorescent glucose analogue, and other porin-dependent compounds, was modulated by changes in the internal  $H^+$  and  $K^+$  levels (achieved using ionophores and different external solutions). I then exploited an optically activated proton pump to increase periplasmic  $H^+$  and demonstrate that this reduced porin permeability (monitored by live single-cell imaging). In support of a model dependent on changes in periplasmic ions, molecular dynamic simulations suggest that the pore diameter of porins is predicted to be reduced by increased periplasmic  $H^+$  ions.

Secondly, I examined the dynamic regulation of internal ions in live bacteria by expressing a wide range of genetically encoded fluorescent ion sensors in cells trapped in a microfluidic device. I found that the periplasmic ionic environment is partially insulated from the external ion concentrations and observed oscillations in periplasmic and cytosolic  $H^+$  and cytosolic  $K^+$  ions. I observed that inner membrane voltage is principally controlled by  $H^+$  and  $K^+$  gradients and is characterised by spikes (or action potentials) driven by activation of the voltage-gated potassium channel Kch, which acts to increase periplasmic  $H^+$  and  $K^+$  levels and, as a consequence, increases porin permeability.

By examining ion changes and porin permeability of bacteria under starvation or in minimal media supplemented with low or high glucose levels or lipids, I developed a model for metabolic control of porin function. Under starvation (with predicted low levels of periplasmic  $H^+$  and  $K^+$ ), porins are open. Porins shut when bacteria are exposed to low glucose or lipid media (where periplasmic  $H^+$ , but not  $K^+$  levels rise). However, under conditions of high metabolism, porins open again (since Kch is activated, leading to low  $H^+$  and high  $K^+$  levels in the periplasm).

Thirdly, I tested my model's predictions and clinical relevance by examining the permeability and susceptibility of ciprofloxacin (an antibiotic known to rely on porins for entry into bacteria). As expected, uptake and subsequent activity of ciprofloxacin was significantly lower in lipid compared to glucose media and could be increased by increasing bacterial  $H^+$  levels. Ciprofloxacin uptake was higher in wild type bacteria cells exposed to high rather than low glucose, and this phenomenon relies on Kch activity. My work demonstrates dynamic regulation of porin permeability, which will have important clinical implications for antibiotic development and for potentially explaining the increase in antibiotic resistance seen in lipid media (and intracellular bacteria) and the development of deleterious mutations in central metabolism genes during adaptation to antibiotic treatment.

Finally, I examine the biological impact of the only intrinsically produced protonophore, indole. I describe two patterns of indole production depending on the carbon source: glycolytic sugars trigger a strong indole pulse, while gluconeogenic carbon sources result in steady indole production. These behaviours are mainly controlled by modulating the synthesis of tryptophanase, which is responsible for indole production. I show that indole production modulates the membrane potential, suggesting a potential role in regulating porin permeability and other bacterial processes.

The work presented here constitutes a great leap forward in our understanding of the role and functions of the periplasmic space. Future research could use our results for the development of adjuvant molecules that take advantage of our framework to increase permeability to antibiotics.

## **ACKNOWLEDGEMENTS**

First and foremost, I would like to thank my supervisor, Professor Andres Floto. I will never say thank you enough for giving me the opportunity to embark on this PhD. Thanks for your guidance throughout the years and your support. I would also like to thank Dr David Summers, with whom I started working at the Department of Genetics with the help and mentoring of Dr Ashraf Zarkan.

This research has involved the help of multiple collaborators both inside and outside the Floto Lab. First, I would like to thank Ali Alsulami for his great work on Molecular Dynamics. Then, I would like to thank Dr Ieuan Evans for his contribution. Finally, I would like to thank Dr Anja Hagting for her endless hours dedicated to help and support me. You never gave up.

In addition, I want to thank everyone in the Floto group, past and present, for your help and support throughout the years. You are the heart of the lab: Divya Aurora, Vitor Mendes, Louise Ellison, Dr Charlotte Passemar, Dr Sophie Burbaud, Dr Sina Krokowski, Karen Brown, Lucas Boeck, Catherine Klapholz, Dr Yu Zhang, Judy Younts-Ryan. You have all contributed to my growth, both personally and professionally. Special thanks to Dr Aaron Weimann and Jasper Sangen, to whom I am incredibly happy to have shared this entire experience. Also, thank you to my friend Rhys for his time and patience.

Finally, I would like to thank my family, father, and mother, who made the impossible possible. Lastly, I am most thankful to my wife Erjona, who has been my pillar and my light throughout this journey.



# CONTENTS

CHAPTER 1: INTRODUCTION .....	1
INTRODUCTION .....	2
1.1 <i>Bacteria</i> .....	2
1.2 <i>The definition of Gram-negative bacteria</i> .....	2
Escherichia coli .....	3
1.3 <i>The bacterial outer membrane</i> .....	4
1.3.1 The evolution of double membranes.....	5
1.3.2 The function of the outer membrane .....	6
1.3.3 The periplasmic environment .....	7
1.3.4 Porins and pore-like proteins.....	8
1.3.4.1 Structure and function of porins.....	8
Protonation effect on porin.....	9
Ionic modulation of porins .....	10
1.3.4.2 Solute specific porins .....	11
1.3.4.3 Genetic regulation of porins .....	12
1.4 <i>The inner membrane</i> .....	13
1.4.1 Inner membrane molecular composition .....	13
1.4.2 Transport across the inner membrane .....	14
1.4.2.1 The PTS transport system .....	14
1.4.2.2 ABC transporters .....	16
1.4.3 Efflux pumps .....	16
1.4.3.1 ABC efflux pumps.....	17
1.4.3.2 RND efflux pump .....	18
1.4.3.3 MFS efflux pumps .....	18
1.4.4 Ion transport and membrane potential .....	19
1.4.4.1 Sodium transport.....	19
Melibiose:Na symporters .....	19
Amino acid sodium symporters.....	20
Sodium-proton pumps .....	20
1.4.4.2 Potassium transport .....	21
Kdp .....	21
Trk .....	22

Kup .....	22
Kch.....	22
MscK mechano-sensitive potassium channel.....	23
1.4.4.3 Calcium pumps .....	23
1.4.4.4 Chloride transport channels .....	24
1.4.4.5 Non-selective ion channels.....	24
MscL.....	25
MscS.....	25
1.4.4.6 Proton transport and the proton motive force .....	26
<b>1.5 Bacterial metabolism .....</b>	<b>26</b>
1.5.1 Glycolysis and fermentation .....	27
1.5.2 The tricarboxylic acid cycle .....	28
1.5.3 The electron transport chain .....	29
1.5.3.1 Proton pumps .....	30
1.5.3.2 Terminal oxidases .....	30
1.5.3.3 The ATP synthase.....	32
1.5.4 Metabolic oscillations .....	32
1.5.4.1 Carbon metabolism oscillations.....	32
1.5.4.2 Cell growth oscillations.....	33
1.5.5 Membrane potential modulation in bacteria .....	33
1.5.5.1 Indole effect on membrane potential .....	34
Indole regulation .....	35
<b>1.6 The study of single-cell microbiology.....</b>	<b>35</b>
1.6.1 Microfluidics devices for bacterial microbiology .....	36
1.6.2 Design and fabrication of microfluidics devices.....	37
1.6.3 The mother machine.....	38
<b>RESEARCH AIMS &amp; OBJECTIVES .....</b>	<b>39</b>
<b>CHAPTER 2: GENERAL METHODS .....</b>	<b>41</b>
<b>2.1 Strains.....</b>	<b>42</b>
2.1.1 Strains list .....	42
<b>2.2 Medium and growth conditions.....</b>	<b>43</b>
2.2.1 Rich medium .....	43
2.2.2 Minimal medium composition and preparation .....	43
2.2.3 Growth conditions .....	44
<b>2.3 Cloning of fluorescent reporters .....</b>	<b>44</b>
2.3.1 Cloning techniques .....	44
2.3.2 Genetic material .....	46

2.4 Chemicals and probes.....	47
2.4.1 Antibiotics .....	47
2.4.2 Ionophores and other chemicals .....	47
2.4.3 Fluorescent probes .....	47
2.5 Microfluidics .....	48
2.5.1 Chip design.....	48
2.5.2 Chip preparation .....	49
2.5.3 Cell trapping in chip .....	49
2.6 Statistical analysis and data analysis.....	50
2.7 Statistical analysis .....	50
2.8 Image analysis .....	50
<b>CHAPTER 3: PERIPLASMIC IONS MODULATE BACTERIAL PERMEABILITY .....</b>	<b>52</b>
SUMMARY .....	53
INTRODUCTION .....	55
MATERIAL AND METHODS.....	57
3.1 Flow cytometry protocol for permeability estimation .....	57
3.2 Treatment optimisation.....	58
3.3 Cloning and expression of ArchT .....	58
3.4 ArchT validation.....	60
3.5 2NBDG uptake in the Mother Machine.....	60
3.6 Molecular dynamics simulation .....	61
RESULTS .....	62
3.7 Optimisation of bacterial permeability assay .....	62
3.7.1 Time optimisation of bacterial permeability assay .....	63
3.7.2 Porin deletion decreases 2NBD, BFL and Hoechst uptake .....	64
3.8 Ionophore effect on membrane potential.....	66
3.8.1 Ionophore optimisation .....	66
3.8.2 CCCP and valinomycin modulate permeability .....	67
3.9 High internal potassium increases porin permeability .....	68
3.10 The decrease in internal pH reduces permeability.....	69

3.11 ArchT activation increases cytoplasmic pH .....	71
3.12 ArchT activation decreases 2NBDG uptake .....	72
3.13 2NBDG uptake correlates with membrane depolarisation .....	74
3.14 Porin protonated periplasmic residues lead to pore contraction .....	75
DISCUSSION .....	77
3.15 Membrane permeability estimation .....	77
3.16 Potassium increases permeability.....	77
3.17 Proton decreases of permeability .....	78
3.18 Membrane depolarisation correlates with 2NBDG uptake .....	79
3.19 Porin pore diameter narrows with protonation.....	79
3.20 Conclusion .....	80
<b>CHAPTER 4: TRANS-MEMBRANE ION OSCILLATIONS .....</b>	<b>81</b>
SUMMARY .....	82
INTRODUCTION.....	83
MATERIAL AND METHODS .....	85
4.1.1 Ion sensor calibration .....	85
4.1.2 Ion oscillations .....	85
4.1.3 Carbon source switching.....	86
4.2 Agar pads .....	86
4.3 Permeability analysis.....	86
RESULTS .....	88
4.4 Cloning and expression of pelBCpHuji.....	88
4.5 Ion sensors calibration .....	89
4.5.1 Periplasmic pH sensor validation.....	89
4.5.2 pHluorin pH calibration.....	90
4.5.3 GINKO1 K <sup>+</sup> calibration .....	91
4.6 Spontaneous ion oscillations.....	92
4.7 Carbon sources drive ion oscillations .....	93
4.8 Carbon sources induce membrane potential spikes .....	95
4.9 Ionophore effect on membrane potential spikes.....	98

4.10 KO strains have different QuasAr2 expression.....	99
4.11 Resting membrane potential in different knockout strains .....	100
4.12 Deletion of the Kch channel reduces the spike size.....	100
4.13 Kch deletion causes periplasm acidification .....	101
4.14 Changes in the carbon metabolism influence bacterial permeability ..	102
DISCUSSION AND CONCLUSION .....	104
4.15 Cytoplasmic and periplasmic pH.....	104
4.16 Buffering of the cytoplasmic K <sup>+</sup> .....	105
4.17 Ion oscillations and carbon source.....	106
4.18 Carbon source drives permeability.....	108
4.19 Conclusion.....	109
<b>CHAPTER 5: THE CARBON SOURCE INFLUENCES ANTIBIOTIC RESISTANCE THROUGH MEMBRANE PERMEABILITY.....</b>	<b>110</b>
SUMMARY .....	111
INTRODUCTION .....	113
MATERIAL AND METHODS.....	115
5.1 Ciprofloxacin uptake in the Mother Machine .....	115
5.2 MIC and EC50 calculation .....	115
RESULTS .....	117
5.3 Porin mediates ciprofloxacin uptake.....	117
5.4 Periplasmic pH drives the carbon source effect.....	118
5.5 Kch effect on permeability depends on carbon source.....	119
5.6 The $\Delta kch$ strain and porin knock-outs are more resistant to ciprofloxacin but not to colistin.....	119
5.7 Carbon source modulates ciprofloxacin MIC .....	120
DISCUSSION AND CONCLUSION .....	123
5.8 Carbon source drives membrane permeability.....	123

5.9 Carbon source affects antibiotic susceptibility .....	124
5.10 Conclusion .....	126
<b>CHAPTER 6: INDOLE PRODUCTION REGULATES MEMBRANE POTENTIAL.....</b>	<b>127</b>
SUMMARY .....	128
INTRODUCTION.....	129
MATERIAL AND METHODS .....	130
6.1 Indole measurements.....	130
6.2 Tna-GFP fluorescent measurement .....	130
6.3 Membrane potential estimation with Oxonol-VI.....	130
6.4 Measurements of cytoplasmic pH .....	131
RESULTS .....	133
6.5 Regulation of indole production.....	133
6.5.1 Glycolytic flux controls indole production .....	133
6.5.2 Indole pulse is regulated via TnaA synthesis.....	134
6.6 Indole regulation on membrane potential.....	135
6.6.1 TnaA synthesis happens during the entrance of the stationary phase.....	135
6.6.2 Indole causes a proton leak .....	136
6.6.3 The strain $\Delta tnaA$ has a higher pH than WT .....	137
DISCUSSION AND CONCLUSION .....	139
6.7 Regulation of indole synthesis.....	139
6.8 Indole effect on membrane potential .....	140
<b>CHAPTER 7: GENERAL DISCUSSION AND CONCLUSION.....</b>	<b>142</b>
DISCUSSION .....	143
7.1 Regulation of porin permeability by periplasmic ions .....	143
7.2 Periplasmic ion isolation .....	145
7.3 Carbon source drives ion oscillations.....	146
7.4 Carbon metabolism drives ciprofloxacin uptake.....	147
7.5 Regulation of indole and membrane potential.....	148
<b>CHAPTER 8: APPENDIX AND REFERENCES .....</b>	<b>151</b>

REFERENCES.....152

## LIST OF TABLES

TABLE 1: LIST OF STRAINS USED IN THIS WORK. ....	42
TABLE 2: LIST OF PLASMIDS USED FOR THIS WORK. ....	46
TABLE 3: LIST OF PRIMERS USED IN THIS WORK. ....	46
TABLE 4: ANTIBIOTICS USED FOR THIS WORK. ....	47
TABLE 5: IONOPHORES USED FOR THIS WORK. ....	47
TABLE 6: LIST OF FLUORESCENT PROBES USED FOR THIS WORK. ....	47
TABLE 7: ILLUMINATION CONDITION FOR EACH FLUOROPHORE. ....	48
TABLE 8: ILLUMINATION CONDITIONS OF EACH FLUORESCENT SENSOR. ....	85
TABLE 9: FULL DESCRIPTION OF THE PARAMETRIC MODEL FOR SPIKE COUNT. ....	97

## LIST OF FIGURES

FIGURE 1.1: GRAM-NEGATIVE OUTER MEMBRANE STRUCTURE.....	4
FIGURE 1.2: CARTOON DIAGRAM OF THE OMPF CRYSTAL STRUCTURE. ....	9
FIGURE 1.3: PTS TRANSPORTER DIAGRAM .....	15
FIGURE 1.4: ABC EFFLUX PUMP DIAGRAM.....	17
FIGURE 1.5: DIAGRAM OF THE GLYCOLYTIC PATHWAY.....	27
FIGURE 1.6: DIAGRAM OF THE ELECTRON TRANSPORT CHAIN .....	29
FIGURE 2.1: DIAGRAM OF THE MOTHER MACHINE. ....	48
FIGURE 3.1: EXPRESSION VECTOR PBAD-ARCHT.....	59
FIGURE 3.2: TRACER UPTAKE BY BACTERIA DEPENDS ON EXTERNAL CONCENTRATION. ....	63
FIGURE 3.3: FLUORESCENCE TRACER UPTAKE OVER TIME.....	64
FIGURE 3.4: FLUORESCENT TRACER UPTAKE IS MEDIATED BY PORINS. ....	65
FIGURE 3.5: IONOPHORE TREATMENTS IMPACT MEMBRANE POTENTIAL.....	66
FIGURE 3.6: IONOPHORES MODULATE TRACER UPTAKE. ....	67
FIGURE 3.7: PERMEABILITY OF VALINOMYCIN TREATED CELLS DEPENDS ON POTASSIUM CONCENTRATION.....	68
FIGURE 3.8: THE PORIN OMPC MEDIATES THE POTASSIUM EFFECT ON PERMEABILITY. ....	69
FIGURE 3.9: PERMEABILITY OF CCCP TREATED CELLS CORRELATES WITH PH.....	70
FIGURE 3.10: THE PH PERMEABILITY EFFECT OF CCCP TREATED CELLS DEPENDS ON BACTERIAL PORINS. ....	71
FIGURE 3.11: ILLUMINATION WITH 561 NM LIGHT LEADS TO A DECREASE IN CYTOPLASMIC PH OF CELL EXPRESSION ARCHT. ....	72
FIGURE 3.12: LIGHT ACTIVATION OF ACHT LEADS TO A DECREASE IN 2NBDG UPTAKE. ....	73
FIGURE 3.13: UPTAKE OF 2NBDG CORRELATES WITH AN INCREASE IN Q2 FLUORESCENCE.....	74
FIGURE 3.14 PROTONATION OF THE PERIPLASMIC RESIDUES COMPRESSES THE PORE DIAMETER OF OMPC AND OMPF. ....	75

FIGURE 4.1 EXPRESSION VECTOR PBAD-PELBC::PHUJI.....	88
FIGURE 4.2: PELBC::PHUJI SENSOR CALIBRATION .....	89
FIGURE 4.3: PHLUORIN CALIBRATION.....	90
FIGURE 4.4: CYTOPLASMIC GINKO1 CALIBRATION.....	91
FIGURE 4.5: <i>IN VIVO</i> DYNAMICS OF PHYSIOLOGICAL IONS IN <i>E. COLI</i> ARE DOMINATED BY K <sup>+</sup> AND PERIPLASMIC PH.....	93
FIGURE 4.6: REPRESENTATIVE TRACES OF THE ELECTROPHYSIOLOGICAL SENSORS. ....	94
FIGURE 4.7: VOLATILITY OF ELECTROPHYSIOLOGICAL IONS ON DIFFERENT CARBON SOURCES. ...	95
FIGURE 4.8: CARBON SOURCE DRIVES MEMBRANE POTENTIAL SPIKES. ....	98
FIGURE 4.9: IONOPHORE MODULATION OF MEMBRANE POTENTIAL BASELINE. ....	99
FIGURE 4.10: KCH AND OMPC HAVE HIGHER QUASAR2 MAXIMUM SIGNAL.....	100
FIGURE 4.11: DELETION OF MEMBRANE VOLTAGE REGULATORS AND PORINS MODULATES MEMBRANE POTENTIAL SPIKES.....	100
FIGURE 4.12: THE $\Delta KCH$ STRAIN PRESENTS DIMINISHED SPIKE SIZE.....	101
FIGURE 4.13: POTASSIUM AND PERIPLASMIC PH BASELINE DIFFERENCE BETWEEN WT AND KCH STRAIN. ....	102
FIGURE 4.14: CARBON SOURCE DRIVES BACTERIAL PERMEABILITY.....	103
FIGURE 4.15: DIAGRAM FOR THE REGULATION OF THE PERIPLASMIC IONS AND PERMEABILITY	108
FIGURE 5.1 INDIVIDUAL CIPROFLOXACIN ACCUMULATION EXPERIMENTS FOR THE BACTERIAL KO INVESTIGATED.....	117
FIGURE 5.2: CARBON SOURCE DRIVES CIPROFLOXACIN PERMEABILITY.....	118
FIGURE 5.3: CIPROFLOXACIN UPTAKE ON $\Delta KCH$ AND WT STRAIN AT DIFFERENT GLUCOSE CONCENTRATIONS. ....	119
FIGURE 5.4: EFFECTIVE CONCENTRATION OF CIPROFLOXACIN AND COLISTIN .....	120
FIGURE 5.5: SUSCEPTIBILITY OF THE <i>E. COLI</i> STRAINS (WT, $\Delta PTH$ AND $\Delta ACEA$ ) TO CIPROFLOXACIN IN GLUCOSE, LIPID AND MIXED MEDIA. ....	122
FIGURE 6.1: CARBON SOURCE DETERMINES THE KINETICS OF INDOLE SYNTHESIS IN <i>E. COLI</i> . ...	133
FIGURE 6.2: THE TYPE AND CONCENTRATION OF CARBON SOURCE REGULATE TNA <sup>A</sup> SYNTHESIS. ....	134

FIGURE 6.3: TNAA PRODUCTION IS CORRELATED WITH MEMBRANE DEPOLARIZATION. ....135

FIGURE 6.4: THE ADDITION OF INDOLE ALLOWS PROTONS TO CROSS THE BACTERIAL MEMBRANE.  
.....137

FIGURE 6.5: THE  $\Delta$ TNAA HAS A HIGHER PH THAN WT .....138

## LIST OF ABBREVIATIONS AND ACRONYMS

Acronym	Full name
CCCP	Carbonyl cyanide 3-chlorophenylhydrazone
PMBN	Polymyxin B nonapeptide hydrochloride
ATP	Adenosine 5'-triphosphate
ThT	Thioflavin-T
OxVI	1,5-Bis(5-oxo-3-propylisoxazol-4-yl)pentamethine oxonol
H <sup>+</sup>	Hydrogen ion
K <sup>+</sup>	Potassium ion
2NBDG	2-(N-(7-Nitrobenz-2-oxa-1,3-diazol-4-yl)Amino)-2-Deoxyglucose
BFL	Bocillin FL
ETC	Electron Transport Chain

# **Chapter 1:**

# **INTRODUCTION**

## **Introduction**

### **1.1 Bacteria**

Bacteria are one of the most diverse domains of life. The number of different species ranges between 10-1000 billion approximately<sup>1-3</sup>. A great deal of their success emerges from their structural simplicity<sup>4</sup>. The basic components of a bacteria are a DNA chromosome, the ribosomal machinery and a semi-crystal fluid called cytosol, where enzymes and proteins carry out the metabolic activity. This microcellular structure is then surrounded by a lipid membrane that isolates these internal components from the environmental changes and a cell wall of peptidoglycan, a strong polymer that protects the cell from osmotic changes<sup>5</sup>. Upon this cell wall, we find that all but three of the 30 bacteria phyla also have an outer layer<sup>6</sup>.

### **1.2 The definition of Gram-negative bacteria**

The classification of Gram-negative and Gram-positive species was proposed for the first time in 1884 by Hans Gram, who described the Gram staining method<sup>7</sup>. This technique stained bacteria with crystal violet. When this pigment contacts the bacterial cell wall, it strongly binds the peptidoglycan chains and thus makes bacteria visible on a light microscope. Interestingly, a quick wash with alcohol removes most of the dye from some bacteria – these are then called gram-negative, but not other. The bacteria that retain the crystal violet attached to their cell wall, the gram-positive, is due to their much thicker peptidoglycan compared to gram-negative.

Even though this classification does not represent a monophyletic group (deriving from one common ancestor), it is still widely used today. Gram-negative bacteria are classified into ten super-groups: *proteobacteria*, *cyanobacteria*, *spirochetes*, *green-sulphur bacteria*, *chloroflexi*, *bacteroides*, *planctomycetes*, *chlamydia*,

*micrococci*, and *thermotogae*<sup>8</sup>. Of all these groups, the most relevant to humans is the *proteobacteria* because they are the most numerous and relevant.

The phylum of *proteobacteria* is by far the largest and most metabolically diverse of all bacterial phyla<sup>9</sup>. Due to this incredible diversity, they were named *Proteobacteria*, after Proteus, a Greek god capable of assuming many different shapes<sup>10</sup>. For example, it is possible to find chemolithotrophic, chemoorganotrophic, and phototrophic species among them<sup>9</sup>. Thus, the phylum is defined primarily in terms of the highly conserved ribosomal 16S-RNA (rRNA) sequences. Nevertheless, our understanding of bacteria comes from very few species that are used as model organisms with the hope that data, models and theories generated will be applicable to other organisms. Among them, the most prominent and widely studied is the  $\gamma$ -proteobacteria *Escherichia coli* (*E. coli*).

### ***Escherichia coli***

The prominence of *E. coli* as a major model organism in biology stems from how easy it is to work with it, isolate, and genetically manipulate it. Most of the strains can quickly grow on many different nutrients<sup>11</sup>. As a result, it became the organism of choice for many pioneering works in biology, including deciphering the genetic code, the beginnings of molecular biology on transcription and the research of cellular replication<sup>12–14</sup>. Another interesting feature of this model organism is that we can find examples of both pathogenic strains such as *E. coli* H157:H7 and mild human symbionts such as the variant *E. coli* K-12. This means it is possible to study many properties of clinical strains using a safer close relative species. In nature, *E. coli* mainly lives in the lower guts of mammals, where it typically constitutes between 0.1–5% of the community. It is also found, albeit less commonly, as part of the microbiomes of other animals as well as on the soil<sup>15,16</sup>.

### 1.3 The bacterial outer membrane

#### Gram negative bacteria cell wall structure

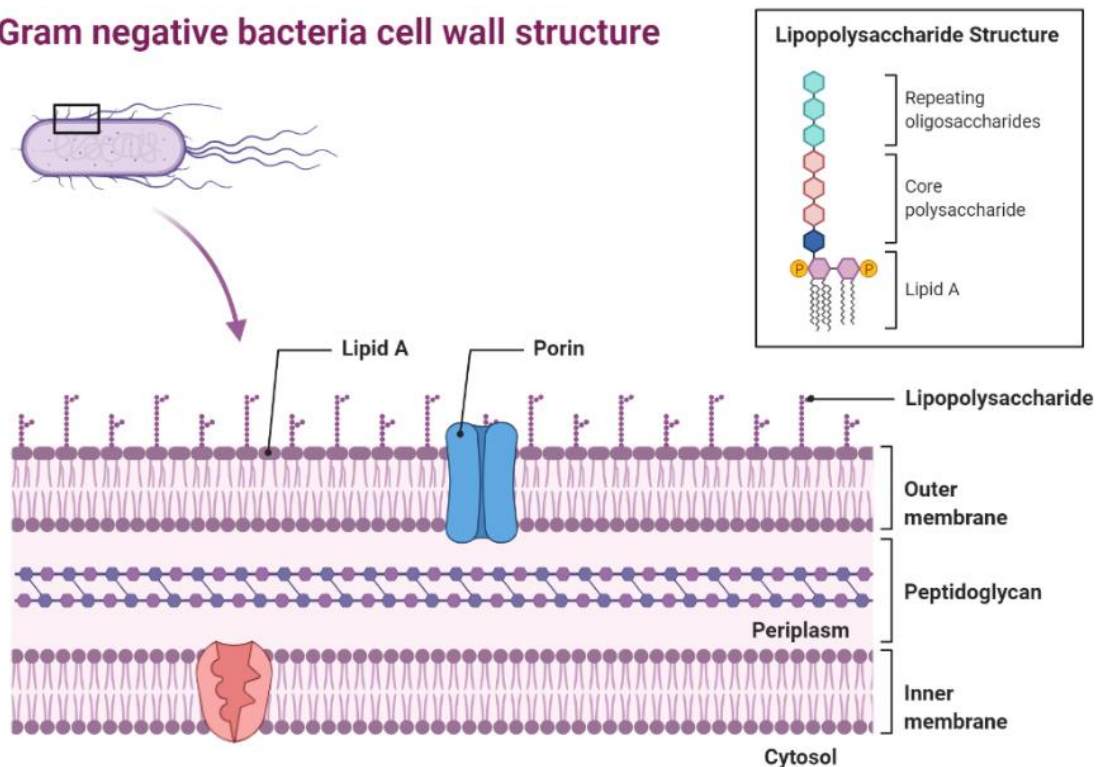


Figure 1.1: Gram-negative outer membrane structure.

The outermost layer of the cell envelope is composed primarily of lipo-polysaccharides (see upper box). Porins (represented in blue) are required for the uptake of small molecules. These channels work as passive transporters. The periplasm (PM) contains the peptidoglycan layer. Finally, the transport across the inner membrane is tightly controlled by active transporters and antiporters (pink). Diagram prepared with BioRender.

The defining feature of gram-negative bacteria such as *Escherichia coli* (*E. coli*) is the presence of an outer membrane<sup>17</sup>. The outer membrane acts as a selective permeability barrier protecting the cell from harmful chemicals and antibiotics. In contrast to the inner membrane, this lipid bilayer is asymmetric, which means the inner leaflet composition differs from the outer (Figure 1.1)<sup>18</sup>. The upper side is populated with long lipopolysaccharide (LPS) chains covalently bound to a lipidic core composed of phospholipids and Lipid A<sup>8</sup>. Due to the bulky size of the LPS chains, divalent cations such as calcium and magnesium intercalate between the LPS molecules to stabilise the membrane<sup>19</sup>. In addition, a lateral cross-binding network seals any gap on the membrane. On the lower leaflet, the lipid composition results are more similar to the inner membrane<sup>20,21</sup>.

The thickness of the outer membrane generates a thick barrier that slows down the traffic of many solutes. Unlike other biological membranes, the outer membrane also excludes hydrophobic compounds due to the long carbohydrate chains of LPS<sup>22-24</sup>. As a consequence, the bacteria express a set of pores, called porins, that facilitate the transport of nutrients and small molecules to the inside<sup>25,26</sup>. This dependence is evident by the co-evolution of porins with the outer membrane<sup>17</sup>.

### **1.3.1 The evolution of double membranes**

Although the bacterial envelope is one of the oldest and most essential bacterial components<sup>27</sup>, its evolutionary emergence is not clear cut. Even today, it remains disputed whether gram-positive (monoderm) or gram-negative (diderm) came first<sup>8,17,28-30</sup>. The enormous variability in gram-negative and outer membrane compositions also blurs the origins of double membranes.

Early hypotheses tried to explain the outer membrane's development through an endosymbiotic event between an ancient actinobacterium and an ancient clostridium<sup>29,31,32</sup>. However, the current leading theories are that a single membrane organism developed a secondary membrane in response to chemical stress<sup>30,33</sup>. A plausible mechanism for this would be the formation of endospores<sup>8,30,34,35</sup>. This idea finds support in the highly conserved sequence of  $\beta$ -barrel porins, which form an integral part of the outer membrane, and Hps70 proteins, which constitute the most conserved protein family present in all organisms<sup>33,36-38</sup>. Moreover, cryo-electron microscopy images have revealed that some double membrane bacteria can form endospores<sup>39</sup>. Still, the outer membrane could have evolved independently on more than one occasion because of the selective advantage it confers<sup>40</sup>. This theory would explain why the

*Corynebacterium* phyla have such a distinct double-membrane despite having close genetic proximity to other gram-positives<sup>8,39,40</sup>.

Another possibility is that a double membrane organism sits at the root of the gram-positives so that dropping the outer membrane gives way to monoderm organisms<sup>8,17,27</sup>. This hypothesis finds support in the fact that some firmicutes, considered as the classic example of monoderm bacteria, do actually contain a mixture of monoderm and diderm cell envelopes<sup>17</sup>.

### **1.3.2 The function of the outer membrane**

As I have mentioned above, the outer membrane is the first line of defence against environmental threats. The dense LPS cover effectively reduces the rate at which toxins and antibiotics can cross to the inside<sup>41,42</sup>. In fact, it has been demonstrated that bacteria can remodel the LPS composition as a response to chemical treatments, leading to the emergence of resistant bacteria<sup>22,23</sup>. Therefore, most drugs access the cell through the mediation of porins<sup>25,26,43</sup>. As expected, mutations in the porin structure or their regulatory regions are frequently found in antibiotic-resistant bacteria. These kinds of adaptation in bacteria are so frequent that they can be easily induced in the lab by exposing bacteria to antibiotic treatment during a few generations<sup>44-46</sup>.

The outer membrane porins are wide, non-specific pores that facilitate the transport of nutrients and other small molecules, including most antibiotics, across the membrane<sup>25,26</sup>. In addition, there are some cases of molecule specific porins, such as the siderophore *fhuA*, specialised in metal ion uptake, and phospholipid transporters such as *mlaC*<sup>25,26,47,48</sup>.

Beyond its role as a barrier against external molecules, the outer membrane also has other vital functions. It also plays a crucial role in the cellular adhesion to abiotic surfaces and living cells<sup>49,50</sup>. This interaction is essential for both pathogen's

adhesion and symbiont colonisation<sup>51–54</sup>. Moreover, when interacting with other bacteria, the outer membrane mediates the cell-to-cell contact and promotes biofilm formation<sup>55–59</sup>.

Finally, the outer membrane creates an inter-membrane space called the periplasm. The presence of this extra membrane creates a space where the bacteria can potentially accumulate ions independently of the environment. This ion accumulation in the periplasm generates a membrane potential across the inner membrane that can be used by the cell as a source of energy<sup>9</sup>.

### **1.3.3 The periplasmic environment**

The periplasmic chamber represents the space between the two membranes of the cell. In general, this area accounts for 15–20% of the total bacterial volume<sup>60</sup>. Here is where the peptidoglycan cell wall is located. This polymer is mainly composed of alternating N-acetylglucosamine and N-acetylmuramic acid<sup>61</sup>. However, it also contains non-conventional amino acids such as D-glutamic acid and D-alanine, which protects the structure from the degradation of most peptidases<sup>62</sup>. Moreover, lateral bonds among chains and the outer membrane strengthen this cellular exoskeleton.

Another significant feature of the periplasm is its lower pH which creates a highly reductive environment. That means the periplasmic space allows the bacteria to perform chemical transformation requiring extreme conditions, performing a role similar to the endoplasmic reticulum of eukaryotic cells<sup>63</sup>. The source of high proton concentration lies in the electron transport chain system of the inner membrane<sup>61</sup>. This group of proteins transform the chemical energy of nutrients into a proton gradient between the cytoplasm and the periplasm. This process will be explained in detail in section 1.4.4.6.

### **1.3.4 Porins and pore-like proteins**

Porins are required for hydrophilic molecules to cross the outer membrane. However, porins are not limited to gram-negative bacteria, but they also appear in other bacteria species, such as the genus *mycobacterium*<sup>8,33,64</sup>. Depending on the bacteria species and the growth conditions, the average gram-negative have about  $10^5$  porins on their outer membrane<sup>65</sup>. These proteins are mostly found as trimers, and although the term porin refers to non-specific channels, some solute specific porins have been described. Within the context of *E. coli*, the most relevant selective porins are LamB, FcaA and BtuB<sup>25,26</sup>. Regarding the non-specific channels, the most relevant are OmpF, OmpC, and PhoE<sup>25,26</sup>. Initially, porins were described as simple open channels, but recent works on their electrochemical characteristics have revealed their interesting properties beyond simple passive diffusion<sup>66</sup>.

#### **1.3.4.1 Structure and function of porins**

The defining characteristic of all porins is their  $\beta$ -barrel structure that forms the pore. This cylinder shape is formed by 16 or 18 anti-parallel strands<sup>67-69</sup>. Generally, porins with 18 strands act as specific channels, while non-specific channels have 16. Each of these single pores aggregates spontaneously into homo-trimers (**Figure 1.1A and B**). Molecular dynamics simulation has shown that LPS molecules may support the trimeric assembly of OmpF<sup>70</sup>.

Moreover, the crystal structure of many porins has been reported<sup>71,72</sup>. The 3D model shows that the anti-parallel  $\beta$ -strands are connected by highly mobile long loops that protrude into the extracellular side and short loops towards the periplasmic side. Interestingly, the third periplasmic loop, the L3-loop, folds into the channel and creates a constriction zone (**Figure 1.1C**)<sup>44,67,73-77</sup>. This narrow tunnel favours the interaction between the amino acid charges of the L3 loop and the solute, which effectively creates an electrostatic filter<sup>73</sup>.

The filtering properties of the constriction zone are specific for each porin. For example, OmpF has a weak cation bias, while PhoE selects for anions<sup>78-80</sup>. Nevertheless, the pore size compromises the filter efficiency because the wider the pore, the less pore solute interaction. The OmpC porin also has a cation bias, yet the difference in charged amino acids on the L3 loop and the wider pore size decreases its cation selectivity<sup>81</sup>. Finally, it is important to bear in mind that ion selectivity is dependent on both the protein channel and the medium flowing through it.

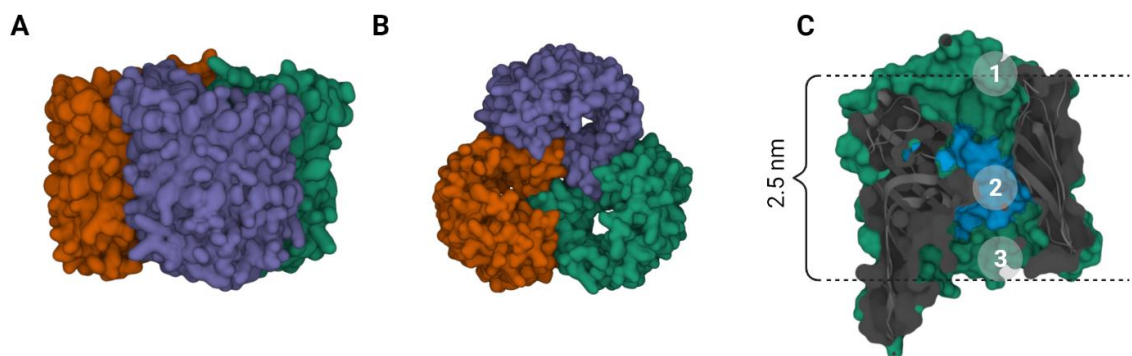


**Figure 1.2: Cartoon diagram of the OmpF crystal structure.**

**A)** Cartoon representation of an OmpF porin triplet lateral view. **B)** Top representation of OmpF triplet **C)** Sideview of a monomer cut midway through the protein. Area 1 indicates the external “vestibule”, area 2 the constriction region, and 3 the periplasmic vestibule. Around the constriction region, the pore diameter reaches a minimum between 2-1 nm. The internal L3 loop is highlighted in blue. This structure was taken from 2ZFG PDB<sup>82</sup>. Diagram was prepared with the PDB 3D viewer.

### ***Protonation effect on porin***

Numerous studies have shown the influence of protonation and ionisation on porin permeability<sup>66</sup>. The first factor associated with porin permeability was pH. The study of porins at different pHs showed that changes in the amino acid's protonation altered its filter bias. For example, OmpF behaves as a weak cation filter at pH 7 but reverts to an anion filter in acidic conditions<sup>83,84</sup>. The effect of pH is not limited to OmpF because it was also found in OmpC<sup>79,85</sup> and subsequently

PhoE<sup>86,87</sup>. These experiments paved the way for the study of porin gating. Initial studies on the crystal structure of OmpF suggested that the L3 loop was flexible enough to occlude the pore cavity<sup>88</sup>. However, experiments immobilising this loop by creating disulphide bonds to the pore wall failed to block the gating behaviour<sup>89,90</sup>. Accordingly, this theory was discarded. Later research has focused on other potential mechanisms. For example, a recent study proposed that the gating mechanism in OmpF depended on the periplasmic loops. At pH7, these loops interact with the surrounding lipids, which stabilise the porin in an open state. However, when the pH decreases below 4, the periplasmic loops interact with each other, thus closing the pore<sup>91</sup>.

### ***Ionic modulation of porins***

Another mechanism proposed for porin gating is the mediation of multivalent cations. The current flow through OmpF is blocked by the addition of multivalent cations such as Mg<sup>2+</sup> ions<sup>92</sup> or La<sup>3+</sup> to the medium<sup>93</sup>. Although this implies that polycations could modulate porin permeability, none of these ions seems to play a relevant role in *E. coli*'s periplasm physiology.

An alternative theory suggested the mediation of organic polyamines. These compounds are polycationic molecules with a hydrocarbon backbone and multiple amino groups<sup>94</sup>. Although they are generally found in the cytoplasm associated with RNA and ribosomes<sup>95-98</sup>, they may also physiologically regulate porin permeability. This hypothesis was supported by experiments where the external addition of spermine, spermidine or putrescine decreased the conductance of porins. Still, the external concentration required to trigger porin blockage was well outside the physiological range<sup>99</sup>. In contrast, if the polyamines are produced from within the cell through plasmid overexpression, tiny concentrations of polyamines can completely block bacteria's permeability<sup>100</sup>. The idea is that internally

produced polyamines could interact with the periplasmic residues of the porins, creating a blockade at the porin, hence reducing membrane permeability.

Finally, it has been reported that a combination of pH (see previous section 1.3.4) and monovalent cations such as potassium have a substantial effect on porin permeability<sup>101</sup>. Experiments in live cells showed that the addition of monovalent cations caused an increase in porin permeability<sup>102</sup>. A plausible mechanism for the blocking would be a competitive interaction involving both cations and protons. In this case, acidic groups require higher concentrations of protons for effective protonation of the residues<sup>101,103</sup>.

#### **1.3.4.2 Solute specific porins**

The best known outer membrane channel with substrate specificity is LamB<sup>26</sup>. This channel favours the diffusion of maltose and maltodextrins. The protein is organised as trimeric  $\beta$ -barrels, but these consist of 18 transmembrane  $\beta$ -strands, in contrast to the 16 found in classical porins<sup>104</sup>. The L3 loop also folds back into the channel, constricting the pore to 0.5-0.6 nm diameter<sup>67</sup>. This region is packed with many charged residues that form hydrogen bonds with the sugars' hydroxyl groups and repel other types of molecules<sup>104</sup>.

Other specific porins described in *E. coli* are siderophores (FecA) and cobalamin transporters (BtuB)<sup>105-107</sup>. The size of metal chelators and cobalamin are too large to pass through generic porins. Nevertheless, the expression of wide pores on its outer membrane would compromise its permeability towards toxins and antibiotics<sup>26</sup>. Therefore, the evolutionary pressure on bacteria led to incorporating a variety of ingenious mechanisms to open and close on these transporters. The primary mechanism relies on a conformation change when the "ligand" binds to the transporter. Then, a mechanism depending on the proton motive force

displaces the plug and allows the solute to cross the membrane to then immediately close<sup>105</sup>.

### **1.3.4.3 Genetic regulation of porins**

The regulation of non-specific porins in *E. coli* is tightly regulated. The gene *phoE* is in the phosphate regulon, and it is mainly expressed during phosphate starvation<sup>108</sup>. This response is achieved through the PhoB-PhoR two-component system that, under phosphate limitation, the inner membrane sensor kinase PhoR autophosphorylates. Subsequent transfer of the phosphate group to PhoB activates the transcription factor<sup>109</sup>.

Furthermore, the two main porins in *E. coli* (OmpF and OmpC) are controlled under the same regulatory mechanism. Their expression responds to three environmental factors: temperature, osmotic pressure and carbon source<sup>26</sup>. High osmotic pressure activates the sensor EnvZ, which phosphorylates OmpR<sup>110</sup>. When OmpR binds to the *ompF* regulatory region, it reduces *ompF* expression while simultaneously promoting *ompC* expression. Warm temperature, on the other hand, increases the transcription of an antisense RNA, *micF*<sup>111</sup>. This short RNA sequence binds to *ompF* mRNA and blocks its translation. Finally, starvation induces the expression of *ompF* through CRP (catabolite repression protein)<sup>112</sup>. In combination, these expression patterns suggest that OmpC is the preferred porin when *E. coli* is living within the host and OmpF is expressed when the bacteria has been expelled from the body and finds itself in low nutrients low-temperature environments.

Other secondary factors affecting porin expression are pH and oxidative stress. At an acidic pH, such as 5.2<sup>113</sup>, the production of OmpF porin becomes strongly repressed, whereas the expression of OmpC increases. The likely transcription factor behind this behaviour is the two-component system CpxR-CpxA<sup>114</sup>. Also, some empirical evidence suggests that porin expression correlates with oxidative

stress<sup>115,116</sup>. The regulation of porin expression mediated by the oxidative stress response seems to respond to chemical toxins and antibiotics in the medium. This effect has been demonstrated to be part of the general SoxR-S (Superoxide Response protein) and MarA (multiple antibiotic resistance) operons<sup>115,116</sup>. It is worth mentioning that these two networks also activate the main multi-drug efflux pump, AcrAB. In combination, this regulatory strategy results in a decreased concentration of toxic molecules in the cytoplasmic through reduced uptake and increased efflux<sup>117</sup>.

## **1.4 The inner membrane**

### **1.4.1 Inner membrane molecular composition**

The inner membrane is considered to be well described by the so-called fluid mosaic model<sup>118,119</sup>. This model describes the membrane as a two-dimensional “liquid” layer of about 5-10 nm thickness, in which lipids and transmembrane proteins can displace laterally<sup>120</sup>. In turn, the movement or fluidity of the membrane depends on its composition. The primary lipids found in the inner membrane of bacteria are phosphatidylglycerol and phosphatidylethanolamine<sup>61,121,122</sup>. Nevertheless, it is important to note that Gram-negative display a great diversity over the inner membrane composition<sup>61</sup>. The lipid composition also varies within the same strain depending on the media conditions because it is part of their adaptative strategy to their environment.

Regarding the protein fraction, it has been estimated that there is one protein per each hundred lipids molecules<sup>123</sup>. The primary functions associated with these proteins are structural support, metabolite transport and energy generation. Within the scope of this work, I will deal only with the last two classes. This section

will cover the transport of molecules across the membrane, while energy will be dealt with in section 1.5.3.1.

### **1.4.2 Transport across the inner membrane**

Membrane transporters can roughly be classified into two groups: transporters and channels<sup>124</sup>. On the one hand, channels form water-filled holes with an opened and a closed state. When the channel opens, substrates freely diffuse across the membrane down their electrochemical gradient<sup>125</sup>. The opening or closing is controlled by a "gate" that responds to external stimuli such as membrane voltage, ligand binding, or stress on the membrane itself<sup>126</sup>. Therefore, channels efficiently dissipate pre-existing electrochemical gradients but do not move a substrate uphill<sup>126,127</sup>. On the other hand, transporters consume energy, which generally is in the form of ATP or an electrochemical gradient, to shuttle the metabolites to the other side. The use of energy allows the transport to flow against the concentration gradient of the metabolite<sup>127</sup>.

#### **1.4.2.1 The PTS transport system**

The phosphoenolpyruvate transport system (or PTS) is a carbohydrate permease<sup>61,128,129</sup>. Its name comes from its peculiar mechanism of action, which uses phosphoenolpyruvate (PEP) as phosphate donor<sup>128</sup>. This clever mechanism ensures, first, that the sugar cannot leave the cell because it has a high negative charge and, second, that the rate of glucose uptake stays in line with the glycolytic rate<sup>61,130</sup>. The genome of *E. coli* encodes more than 38 unique PTS proteins, targeting ten different sugars<sup>131</sup>.

Each functional PTS complex consists of three sugar specific units (EIIA, EIIB and EIIC) and two generic components (EI and HPr)<sup>132</sup>. The first component of the system is the transmembrane protein EIIC, which has a binding site for the sugar on the periplasmic side. Once the sugar is grabbed by the EIIC enzyme, the EIIB

becomes susceptible to phosphorylation, which will trigger the conformational change necessary for the uptake. This phosphate group is later transferred to the sugar, trapping it into the cytoplasm and leaving it ready for glycolysis. This metabolic pathway will further break the sugar into PEP. At this point, the PEP molecule can continue the catabolic digestion (via TCA cycle or fermentation, see section 1.5.1), or it can donate the phosphate radical to the EI enzyme to transport another sugar molecule. If it reacts with the EI enzyme, then the EI will transfer the phosphate to the HPr, which can interact with any sugar specific EIIA. When the HPr-P protein phosphorylates the peripheral domains of EIIA, it can catalyse the phosphate's transfer to the EIIB and repeat the cycle once again (see **Figure 1.3**).

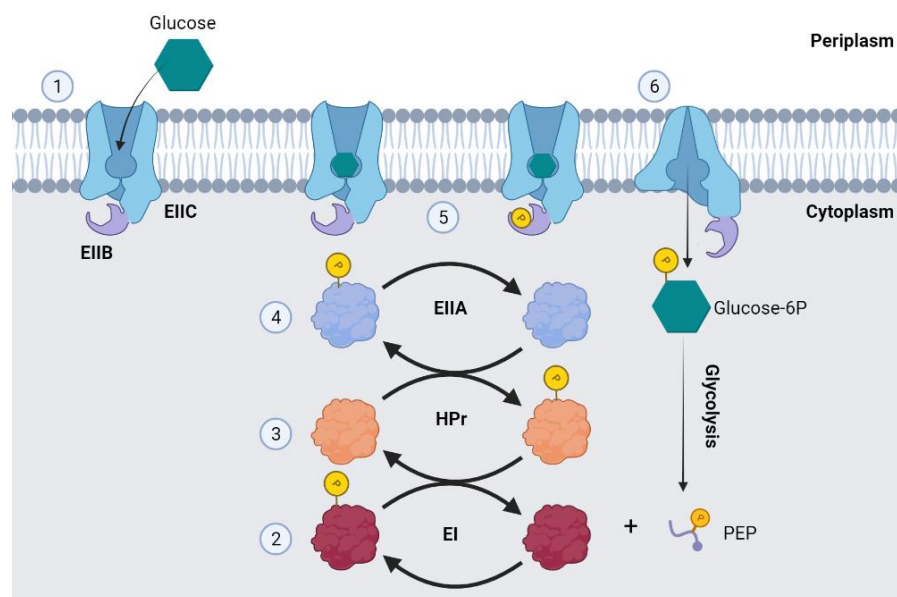


**Figure 1.3: PTS transporter diagram**

In its resting state, glucose binds to the outer membrane site of EII C (1). Now, the activation energy for the uptake comes from the PEP that transfers its phosphoryl group to the EI (2). In turn, the EI enzyme passes this phosphate to HPr (3), and from the HPr, the phosphoryl moves on to EIIA (4). This enzyme is sugar specific, and it further transfers the phosphoryl group to EIIB (5). Finally, EIIB phosphorylates glucose as it crosses the plasma membrane through the transmembrane Enzyme II C (EII C), forming glucose 6-phosphate. Diagram modified in Biorender from Prescott<sup>61</sup>.

### **1.4.2.2 ABC transporters**

The ABC transporter family (from ATP-binding cassette transporter) are transmembrane proteins that actively shuttles molecules across cell membranes<sup>133,134</sup>. This type of protein has great diversity because they have high solute specificity. The most recent reviews estimate that *E. coli* has more than 550 different transporters, representing between 5-10% of its whole genome<sup>135,136</sup>. Their general architecture consists of two transmembrane domains and two nucleotide-binding domains that are in the cytoplasm<sup>134</sup>. The transmembrane domain binds to the nutrients from the periplasmic side while the cytoplasmic side catalyses the hydrolysis of ATP, which triggers a change in conformation to shift the nutrient inside<sup>134,135</sup>.

### **1.4.3 Efflux pumps**

Efflux pumps perform the opposite role to transporters. They are membrane-associated protein assemblies that move molecules from the cytoplasm to the extracellular medium<sup>137</sup>. They are relatively non-specific and pump many different drugs and other chemicals; therefore, they often confer multi-drug resistance. Currently, three pump families have been found in *E. coli*<sup>138</sup>. These are the ATP-Binding Cassette (ABC), the Resistance-Nodulation-cell Division (RND), and the Main Facilitator Superfamily (MFS)<sup>137</sup>. Of these, only the ABC family directly utilises ATP as the energy source to drive transport, while the other two depend on electrochemical ion gradients. Since these proteins are essential for the defence against drugs and toxins<sup>137-139</sup>, this section will give a general overview of the main efflux pump families in *E. coli*.

### 1.4.3.1 ABC efflux pumps

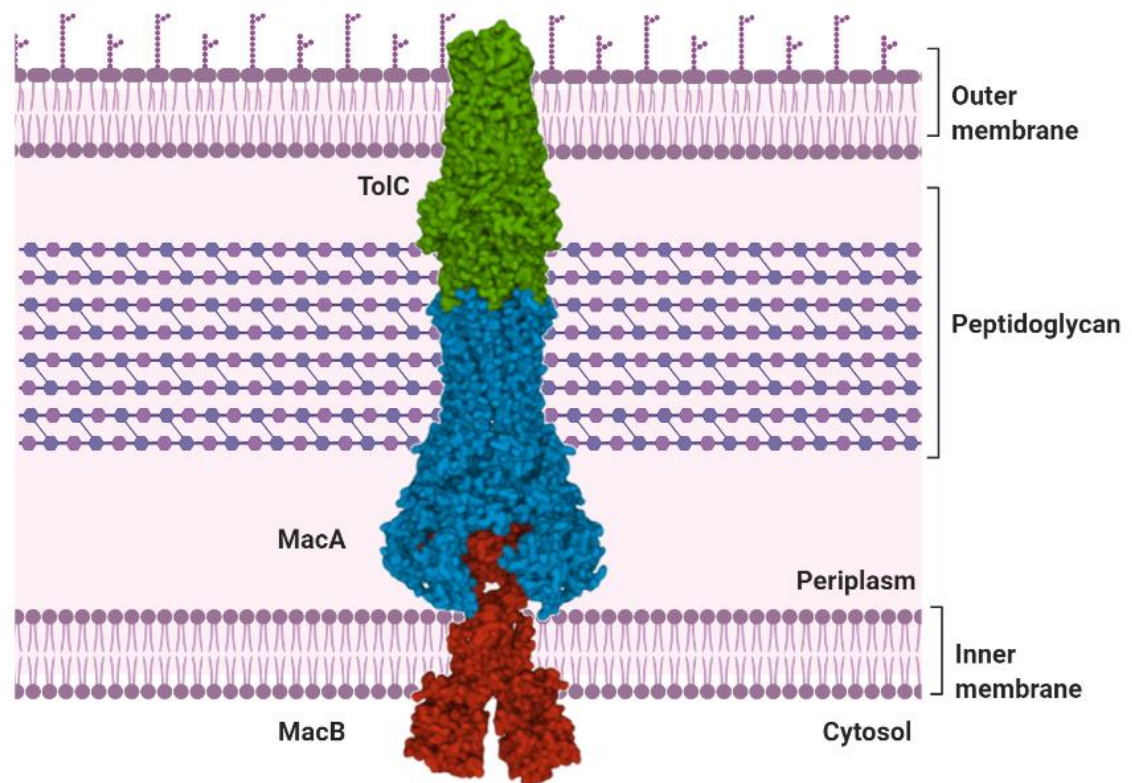


Figure 1.4: ABC efflux pump diagram

In red, the MacB dimer traverses the inner membrane. In blue the MacB complex connecting MacB and TolC. Finally, in green, the TolC crosses the outer membrane. Diagram adapted in Biorender from Fitzpatrick et al<sup>140</sup>.

The ABC efflux pumps have a conserved nucleotide-binding domain, which generates power through ATP hydrolysis and the transmembrane domain that determine transporter function<sup>141</sup>. The substrate-binding site is on the cytoplasmic side, and their periplasmic side is associated with a long tubular protein, TolC, that reaches the outer membrane<sup>142–144</sup>. The bacterium *E. coli* only has the MacAB system<sup>140,145</sup>. The protein MacB is a homodimer inserted in the inner membrane that binds to the drug. Then, MacA acts as a connector between MacB and TolC. The naming of *macA* and *macB* refers to their ability to confer resistance to macrolide antibiotics via plasmid overexpression, though in standard laboratory culture conditions, *macAB* is not expressed<sup>146,147</sup>.

### **1.4.3.2 RND efflux pump**

The Resistance-Nodulation-cell Division (RND) protein family is distinguished for its ability to bind multiple drugs<sup>137</sup>. Therefore, overexpression of these pumps increases drug resistance to numerous drugs<sup>146</sup>. The classic example in *E. coli* is the AcrAB-TolC system<sup>139,148–150</sup>. This protein consists of 12  $\alpha$ -helices which in turn assemble in homotrimers at the inner membrane. The periplasmic side is the conduit for proton movement that fuels the drug efflux through the pore domain<sup>151–153</sup>. This domain is the primary point of drug entry and consists of the subdomains which extend into the periplasm<sup>151,152</sup>. Once the drug enters the pore domain, the AcrB undergoes marked conformational change, fuelled by a proton gradient<sup>154</sup>. Finally, the toxins are funnelled through the TolC pipe outside the cell<sup>151,152</sup>. Several assemblies of the whole AcrAB–TolC complex have been crystallised<sup>155,156</sup>. Its crystal structure suggests that the general principle for poly-specificity comes from compromising the binding affinity towards any particular molecule.

### **1.4.3.3 MFS efflux pumps**

The Major Facilitator Superfamily (MFS) antibiotic efflux pump is the largest and most diverse transporters' family. Overall, they are monomers of 400 to 600 amino acid residues in length and folded into 12 or 14 transmembrane helices<sup>137</sup>. These helices then aggregate in groups of six, forming two domains<sup>157</sup>. The available structural models support an alternating active cycle: open-inwards-bind, open-outwards-release. This transport cycle involves the ordered binding and release of the substrate and protons, but the stoichiometry of drug–proton exchange varies between family members<sup>158</sup>. Three members of the MFS family in *E. coli* has been crystallised: YajR, EmrD and MdfA<sup>159–161</sup>. Overexpression of any of these genes leads to increase resistance to particular drugs but not cross resistance<sup>146</sup>.

### **1.4.4 Ion transport and membrane potential**

The movement of ions across the membrane plays a distinctive role compared to other metabolites. Ions are charged particles, so an asymmetric distribution of ions generates a membrane voltage<sup>162</sup>. This electrical potential across the membrane (also called membrane potential or membrane voltage) becomes an energy source for other cellular processes. For example, we have seen in the previous section how the sodium and proton gradient are frequently used for metabolite transport. On top of that, the membrane potential also plays a main role in flagella motility, cell signalling and especially ATP synthesis<sup>163–165</sup>.

The most relevant ions in bacterial physiology are Na<sup>+</sup>, K<sup>+</sup>, Cl<sup>-</sup>, H<sup>+</sup>, and to some extent, free Ca<sup>2+</sup>. This section will deal with the transport of all ions except H<sup>+</sup> due to their significant role in energy generation. The role of protons will be explained in-depth in section 1.4.4.6.

#### **1.4.4.1 Sodium transport**

All bacteria maintain a lower concentration of Na<sup>+</sup> in the cytoplasm than in periplasm<sup>166</sup>. Thus, sodium enters the cell down an electrochemical concentration gradient. In turn, this favourable flow is used for the co-transport of multiple metabolites. In total, the genome of *E. coli* encodes around 16 sodium co-transporters. The most relevant cases are the sodium-proton antiporters, the melibiose symporters and the amino acid sodium symporters<sup>136,167</sup>.

#### ***Melibiose:Na symporters***

The melibiose-sodium symporter (MelB) of *E. coli* belongs to the Glycoside-Pentoside-Hexuronide:cation symporter family<sup>167,168</sup>. Two-dimensional crystal models of *E. coli* MelB show 12 transmembrane helices transporter<sup>169–171</sup>. There

are two binding sites on the periplasmic side, one for  $\beta$ -galactosides and the second the cations. Interestingly, the  $\beta$ -galactoside site presents some promiscuity, which means it also binds to tri and tetra-galactosides and several other monosaccharides<sup>172-175</sup>. Finally, MelB is temperature-sensitive in *E.coli* because it stops being active at 30 °C, suggesting that this system plays an important role when bacteria is outside the host.

### ***Amino acid sodium symporters***

Early observations already suggested that the addition of Na<sup>+</sup> to the medium increased the uptake of several amino acids, among them proline, glutamate, serine, and threonine<sup>167</sup>. This finding was later confirmed by finding six different genes in *E. coli* encoding for sodium-aminoacid transporters, but many more have been described in other species<sup>167,176</sup>. These proteins are classified as the sodium:solute symporter family<sup>177</sup>. The reference model is the proline:sodium symporter PutP<sup>167</sup>. Although the whole protein has not been crystalised, computational models revealed a backbone based on 13 transmembrane  $\alpha$ -helices with the N-terminus on the periplasmic side and the C-terminus facing the cytoplasm<sup>178</sup>. When reconstituted into lipid membranes, the protein effectively carried proline in response to a Na<sup>+</sup> gradient and a 1:1 stoichiometry<sup>179</sup>. Interestingly, it also responds to a lithium gradient but not hydrogen, which indicates the presence of an exclusion size ring<sup>180</sup>. Nevertheless, the role of this protein within the cell is still poorly understood.

### ***Sodium-proton pumps***

The bacterium *E. coli* express two very different sodium:proton antiporters: NhaA<sup>181</sup> and NhaB<sup>182</sup>. The NhaA is the main Na:H antiporter. This protein has a prominent role in ion and pH homeostasis as it can uptake two protons per each sodium ion pushed out<sup>181</sup>. This activity is regulated by pH because it becomes inactive at acidic pH and fully active at pH 8<sup>183</sup>. Structurally, NhaA exists as a dimer

within the membrane<sup>184–186</sup>. NhaA monomers are also functional for Na<sup>+</sup>:H<sup>+</sup> antiport, but dimers are important under conditions of extreme stress, possibly due to increased stability<sup>187,188</sup>. Each NhaA monomer is composed of two five-transmembrane topology-inverted repeats that intertwine. Together they form two distinct structural domains, the translocation core and an interface domain<sup>189,190</sup>. Finally, a cytoplasmic-facing surface that contains many negatively charged residues is located between the core and dimer domains<sup>191,192</sup>.

Our knowledge of NhaB is much more limited than NhaA. Although it is clear NhaB exchanges Na<sup>+</sup> for H<sup>+</sup> at a 2:3 ratio, the mechanism of this reaction remains unknown<sup>193</sup>. Sequence analysis predicts a 12 TM domain, but this has yet to be confirmed with the crystal models<sup>182</sup>.

#### **1.4.4.2 Potassium transport**

Potassium is often the principal cation in the cytoplasm of all living organisms. Indeed, the intracellular potassium concentration in *E. coli* reaches 200 mM, which makes it the main inorganic cation<sup>194</sup>. The influx of this ion is mediated both by a constitutive system with a low affinity for potassium (Trk) and an inducible high-affinity system (Kdp) and Kup<sup>195,196</sup>. The outflux of K<sup>+</sup> is regulated by a voltage-activated channel Kch and a mechano-sensitive channel (MscK)<sup>197</sup>.

#### ***Kdp***

Kdp shuttles K<sup>+</sup> across the membrane at the cost of ATP hydrolysis. Its structure consists of three large protein subunits (A, B, and C). KdpA contains 12 predicted transmembrane regions which form the K<sup>+</sup> transporting channel. The subunit KdpA contains a conserved signature sequence SKT, also present in TrkH and KtrB, suggesting a binding K-motif<sup>198,199</sup>. The KdpB is phosphorylated by ATP to trigger the conformational change that propels K<sup>+</sup> transport<sup>198</sup>. KdpC seems to form an

oligomer, but its function remains unknown<sup>200,201</sup>. The whole Kdp system is encoded in two operons, one with the active protein (*kdpFABC*) and the second with a sensing system (*kdpDE*), forming what is called a two-component sensor<sup>202</sup>. Therefore, this system activates the Kdp system under extreme K<sup>+</sup> starvation<sup>203</sup>.

### **Trk**

Trk are a family of low-affinity K<sup>+</sup> transporter that uses the proton gradient energy to uptake K<sup>+</sup><sup>204–206</sup>. The bacterium *E. coli* has four constitutive Trk systems: TrkG, TrkH, Kup (formerly TrkD) and TrkF. When the bacterium is in an environment containing >1 mM K<sup>+</sup>, then Trk becomes the predominant uptake system<sup>205</sup>. This process is mainly mediated by TrkG and TrkH. Contrarily to the Kdp system, these two proteins rely on proton gradient to move K<sup>+</sup> across the membrane<sup>207</sup>. Nevertheless, the exact mechanism is not clearly understood. They might require a cytoplasmic associated protein TrkA to work, which in turn could use NAD(H) as a cofactor, hypothetically to accept the incoming proton<sup>208</sup>.

### **Kup**

The Kup system (formerly known as TrkD) is a low-affinity K<sup>+</sup> uptake system. The distinguishing factor with respect to the other Trk systems is its ability to transport caesium and rubidium<sup>209</sup>. Although it is not well characterised, sequence analysis indicates that it is composed of an integral membrane domain with 12 putative transmembrane helices and a hydrophilic C-terminal domain<sup>210</sup>. Like the other Trk systems, Kup likely operates as a potassium-proton symporter<sup>210,211</sup>.

### **Kch**

Kch belongs to the Voltage-gated Ion Channel (VIC) Superfamily of transporters<sup>197</sup>. These proteins encode for two transmembrane domains that aggregate in homotetramers<sup>212</sup>. When inserted in the membrane, the channel resembles an inverted triangle, with the gate closing towards the cytoplasmic end and the filter located

at the other end. This filter is highly specific for potassium with a bias  $K^+$  1,000 : 1  $Na^+$ <sup>126</sup>.

The role of Kch in *E. coli* remains poorly understood. The best-characterised homologue is *yugO*, a potassium channel in *B. subtilis*. This protein is a voltage-activated potassium channel. That means it allows the leakage of potassium when the membrane voltage crosses a certain threshold. Functionally, this protein showed an interesting correlation with cell signalling within biofilms<sup>213</sup>. The biofilm structure entails an asymmetric distribution of nutrients between the periphery and the centre<sup>214</sup>. Thus, bacteria can employ potassium oscillations in order to regulate the growth rate of cells (see section 1.5.4.2). These waves are mediated by *yugO* because its deletion disrupts the potassium oscillations<sup>213</sup>.

### ***MscK mechano-sensitive potassium channel***

MscK is the only ion-specific mechanosensitive channel. Under mechanic tension, the channel allows the flow of potassium<sup>126</sup>. Indeed, MscK is highly regulated because gating requires both membrane tension and high external  $K^+$  concentration<sup>215</sup>. Although this channel has a very low conductance (0.8 - 1nS), it can remain open indefinitely<sup>216,217</sup>. These features mean the channel can release small amounts of potassium for long periods in response to mechanic tension. As a result, the potassium leak leads to membrane depolarisation which halts the formation of the FtsZ<sup>164</sup> ring and prevents cell divisions<sup>126</sup>.

### **1.4.4.3 Calcium pumps**

*Escherichia coli* maintains the concentration of cytosolic free calcium near the 0.1  $\mu$ M range<sup>218,219</sup>. However, the mechanism of calcium uptake remains unknown. To the date, four genes (*calA*, *calC*, *calD*, and *chaA*) have been proposed as calcium

pumps<sup>220</sup>. The three *cal* loci could work as a calcium-phosphate symporter, while the *chaA* gene might encode for a calcium-proton antiporter<sup>220,221</sup>.

#### **1.4.4.4 Chloride transport channels**

Chloride is a very common anion in cell biology, yet chloride's physiological role has not been deeply investigated<sup>222</sup>. In general, chloride concentration is greater in the medium than in the cellular cytoplasm, so the anion naturally moves into the cytoplasm. The genome of *E. coli* encodes for two Clc channels, ClcA and ClcB, that allow the free flow of chloride.

Although both channels are homologues of the super-family of chloride channels (also known as Clc), their structure and function are not well characterized<sup>223</sup>. They are suspected to be voltage-activated channels, but others have proposed activation at low pH<sup>224,225</sup>. Indeed, a recent report suggested that ClcA might work as a chloride:proton antiporter because they found that ClcA channels reconstituted in liposomes generated a Cl<sup>-</sup> at the cost of a proton gradient and vice versa<sup>224</sup>. This mechanism could play a role in low pH adaptation<sup>223</sup>.

#### **1.4.4.5 Non-selective ion channels**

Non-selective cation channels are characterised by low ion discrimination<sup>126</sup>. This low bias is the result of the big pore size. Therefore, they do not serve as ionic channels but *solute* channels that act as mechanic sensors and osmotic pressure regulators<sup>226</sup>. In general, these channels are known as mechanosensitive channels. *E. coli* has three main mechanosensitive channels: MscL, MscS. Nevertheless, wide-genome inference studies suggest there could be up to 7 mechanosensitive channels<sup>227,228</sup>. In this work, I will focus on the role of MscL, MscS, because in all other instances, information is sparse.

***MscL***

MscL is a mechanosensitive channel of large conductance ( $> 2.5$  nS) with no selectivity and no saturation<sup>226</sup>. This channel converts mechanical tension in the cell membrane into an electrochemical response. For example, upon osmotic downshift, water flows into a cell, increasing pressure on the membrane, activating MscL and allowing all types of solutes to exit the cytoplasm<sup>229</sup>. Consequently, MscL acts as a pressure release valve, preventing the rupture of the membrane. Nevertheless, the structure of the sensor has not been fully elucidated. Recently,<sup>230</sup> a two-dimensional crystal model suggested MscL is a homo-oligomer. Each monomer consists of two transmembrane regions connected by a periplasmic loop with the N and C termini located in the cytoplasm<sup>231</sup>.

***MscS***

MscS is a mechanosensitive channel of small conductance (0.8-1 nS) with adaptative response<sup>216</sup>. Therefore, its conductivity declines during continuous stimulation<sup>232</sup>. It has been reported that the activation mechanism depends on tension, but inactivation responds to both tension and membrane voltage dependent<sup>233</sup>. The sensor structure is organised as a homoheptamer, forming a large spheric structure in the cytoplasmic region<sup>234,235</sup>. The interaction between this complex with the transmembrane domain is essential to open the channel, but the exact mechanism is still in dispute<sup>236,237</sup>. It has been proposed that a cytoplasmic sphere swells during the opening, yet the pore gating seems to rely on the rigid transmembrane domain's movement<sup>236,237</sup>.

#### **1.4.4.6 Proton transport and the proton motive force**

The flow of protons across the membrane is essential in cell physiology. I have presented several examples of how the proton gradient serves to transport metabolites, efflux toxins, or exchange for other ions; it also takes part in chemotaxis, signal transduction and, of course, energy generation<sup>238–243</sup>. All this is accomplished through a gradient of protons from the periplasm to the cytoplasm. In standard conditions, the intracellular pH ranges between 7.5 and 8 (10-100 free protons per cell), and the periplasmic pH is relatively lower than the cytoplasm<sup>162</sup>. Still, the precise proton concentration in the periplasm remains elusive<sup>244</sup>. Bulk cell measurement of *E. coli* expressing a gene-encoded pH sensor suggested that the periplasmic pH was equal to the medium pH, but the question was not explored further<sup>245,246</sup>.

Despite the absence of an exact reference value for the periplasmic pH, the bacterial proton gradient has been widely studied<sup>247</sup>. Early measurements in *E. coli* spheroplast – bacterium without the outer membrane – suggested that the electron transport chain could generate a proton gradient between 0.5 to 2 pH units<sup>242</sup>. This value was variable depending on the carbon source and oxygen availability. For example, measurements in live cells in the presence of glycerol and O<sub>2</sub> produced a proton gradient of approximately 0.3 pH difference, while a medium with glucose only generates ~0.2 pH difference<sup>248</sup>. The mechanism causing changes in the proton gradient is mainly the electron transport chain<sup>247</sup>. The following section will deal with bacterial metabolism and how the electron transport chain works.

### **1.5 Bacterial metabolism**

All bacteria require energy to do work and build their cellular components. These processes happen through a network of chemical reactions called metabolism<sup>9</sup>. The metabolic processes implicated in the generation of energy (or catabolism)

produce ATP, the cell's primary energy currency, through the oxidation of organic molecules. The two major routes for energy generation in *E. coli* are glycolysis, implicated in sugar fermentation, and the tricarboxylic acid cycle (TCA), which relies on the electron transport chain<sup>9,61</sup>.

### 1.5.1 Glycolysis and fermentation

Glucose is the preferred carbon source of *E. coli*, but other sugars can also be incorporated into the glycolysis pathway. Overall, the pathway can be divided into two parts: a 6-carbon phase and a 3-carbon phase (see **Figure 1.5**)<sup>9</sup>. During the first stage, the glucose-6P phosphorylated by the PTS system (see section 1.4.2.1) receives another phosphate yielding fructose 1,6-bisphosphate. Then, the 3-carbon stage begins with the cleavage of the fructose 1,6-bisphosphate into two halves producing dihydroxyacetone phosphate and glyceraldehyde 3-phosphate (GAP)<sup>249</sup>.

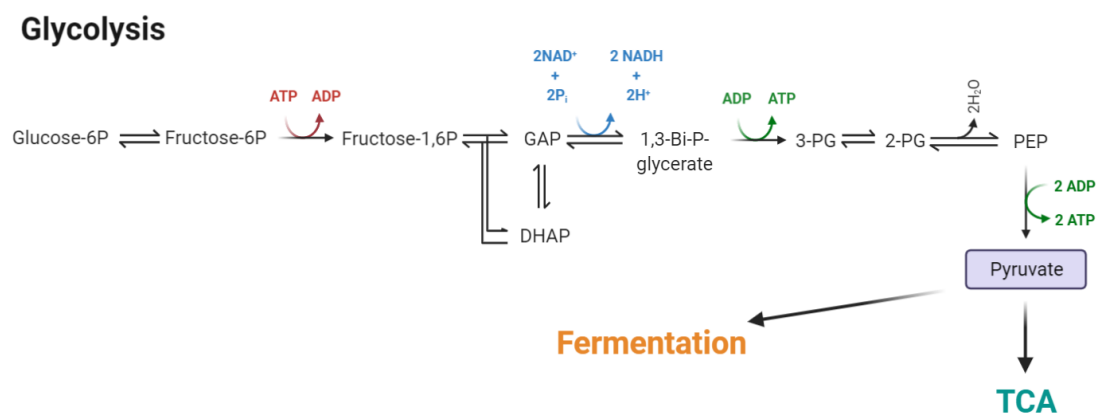


**Figure 1.5: Diagram of the glycolytic pathway**

The abbreviations showed stands in the figure are: P, phosphate; GAP, Glyceraldehyde-3-phosphate; DHAP, Dihydroxyacetone-phosphate; Bi-P-glycerate, 1,3-Bisphosphoglycerate; 3-PG, 1,3-Bisphosphoglycerate; 2-PG, 2-Phosphoglycerate; PEP, Phosphoenolpyruvate. Finally, the pyruvate can feed into the fermentation of the TCA cycle.

The first step of the 3-carbon phase consists in the addition of inorganic phosphate to the GAP. The catalysis of this reaction requires an inorganic phosphate and a

NAD molecule. The resulting compound, 1,3-biphosphoglycerate, is ready for ATP production. Now, our high energy compound can transfer a phosphate group to two ADP molecules, following what is called substrate-level phosphorylation<sup>249</sup>. The final product of the glycolysis yields two NADHs, ATPs and two pyruvate molecules per glucose<sup>250</sup>. At this point, energy production can continue through the tricarboxylic acid cycle in the presence of oxygen or other electron acceptors. Otherwise, *E. coli* needs to balance its redox state produced via the fermentative process (see **Figure 1.5**)<sup>250,251</sup>.

### **1.5.2 The tricarboxylic acid cycle**

The first step after glycolysis is pyruvate decarboxylation. This process is catalysed by the pyruvate dehydrogenase complex, which cleaves pyruvate, releasing carbon dioxide and forming an *activated* compound called acetyl-CoA<sup>252</sup>. This molecule is then ready to enter the TCA cycle.

The TCA is widely recognised as the central metabolic hub of the cell because it produces intermediates that are important in gluconeogenesis, lipolysis, amino acid synthesis, etc<sup>253</sup>. However, this section will focus on the oxidative process for energy production, also called Oxidative Phosphorylation (OXPHOS). The OXPHOS extracts protons from the TCA cycle intermediate molecules to generate a proton gradient across the inner membrane. In turn, this energy is used for the formation of ATP through the ATP synthase. The group of enzymes that participate in the proton transfer across the membrane from the Electron Transport Chain (ETC, see **Figure 1.6**)<sup>252–255</sup>.

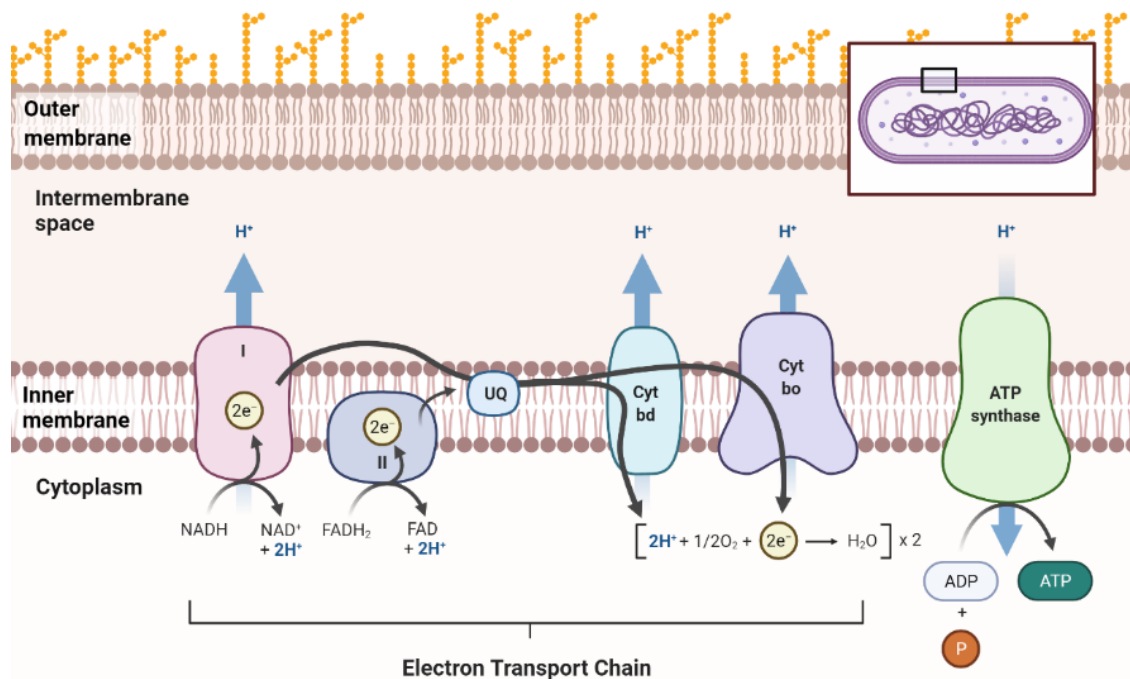


Figure 1.6: Diagram of the electron transport chain

Protons are transported through complex I and complex II. The quinone pool (UQ) can transfer electrons between the components. Cytochromes can transfer electrons to O<sub>2</sub>, forming a water molecule. They also have some proton pump ability. The periplasmic space acts as a reservoir for the proton gradient. Finally, the ATP synthase transforms the proton gradient energy into chemical energy catalysing the P + ADP reaction to form ATP. Diagram prepared with BioRender.

### 1.5.3 The electron transport chain

The ETC comprises a series of electron carriers that coordinate the transfer of electrons from donors, such as NADH and FADH<sub>2</sub>, to acceptors, generally O<sub>2</sub><sup>9,61</sup>. As these electrons flow towards their acceptors, protons are detached and shuttle to the periplasmic side, generating the proton motive force. The *E. coli* ETC (Figure 1.6) has three main components: proton pumps (complex I and II), terminal oxidases (cytochrome-bo, bd-I, and bd-II), and the electron carriers between elements (coenzyme-Q)<sup>256–259</sup>. Finally, the last enzymatic group, the complex V or ATP synthase, consumes the proton gradient to synthesise ATP<sup>260–263</sup>. This section will overview each component of the ETC.

### **1.5.3.1 Proton pumps**

The *E. coli*'s complex I include 13 different subunits encoded in the *nuo* operon<sup>257</sup>. This protein catalyses the transfer of two electrons from NADH to quinone while translocating protons across the membrane<sup>264,265</sup>. It represents the main entry point for electrons from NADH into the respiratory chains<sup>266–268</sup>. Due to its incredible complexity, the complete electron transport mechanism is still not fully understood<sup>257,268</sup>.

The complex-I expression seems to depend on the oxygen because low concentration increases the expression<sup>269,270</sup>. This effect is mediated by the transcription blocker FNR (fumarate and nitrate reduction) that senses oxygen in the medium. In aerobic conditions, the oxygen reacts with the Fe-S cluster of FNR, resulting in the factor inactivation<sup>271</sup>, which allows the expression of the *nuo* operon<sup>272</sup>.

Complex II transfers electrons and protons into the quinone pool using FADH as substrate<sup>273–275</sup>. The expression of complex II proteins is organised in two operons: *frd* and *sdh*<sup>253,276</sup>. The *frd* operon is expressed during anaerobic conditions, and the *sdh* is the preferred form in the presence of oxygen<sup>253,276</sup>.

### **1.5.3.2 Terminal oxidases**

The *E. coli* K-12 encodes three terminal oxidases, cytochrome-bo oxidase (CyoABCD), cytochrome-bd I oxidase (CydABXH), and one cytochrome-bd II oxidase (AppCB)<sup>277–279</sup>. Although all cytochromes can theoretically contribute to the PMF, they are not considered proton pumps because their primary role consists in transferring electrons to the oxygen molecule<sup>258</sup>. Moreover, a growing number of experiments suggest that, beyond its role in cell bioenergetics, the different cytochromes function as O<sub>2</sub><sup>-</sup> scavengers<sup>280–283</sup>.

First, the cytochrome-bd I becomes the primary cytochrome under microaerophilic conditions<sup>258</sup>. This protein complex has two transmembrane subunits and three heme groups<sup>284–286</sup>. These heme groups coordinate the transfer of electrons from the quinone pool to oxygen. In addition, this cytochrome plays a variety of roles as a response to oxidative stress<sup>287,288</sup>. Regarding the expression of the cytochrome-bd, it has been reported that in stressful environments such as high pH, high temperature, presence of cyanides or uncouplers-protonophores lead to an increased gene expression and synthesis<sup>287,289–291</sup>. Interestingly, it appears to exist a positive correlation between virulence and the expression level of the cytochrome-bd. This effect has been attributed to the fact that cytochrome-bd increases tolerance to nitrosative stress and contributes to the detoxification of hydrogen peroxide<sup>258,292–294</sup>.

Second, the cytochrome-bo is predominant during high aeration conditions. This regulation is achieved via FNR. Moreover, the presence of the CRP promoter region also suggests an increased expression at the stationary phase<sup>295–297</sup>. The enzyme structure consists of four subunits with two copper ion kernels<sup>298</sup>. They catalyse the oxidation of ubiquinol and the reduction of oxygen to water<sup>279,299,300</sup>. Two prominent roles have been ascribed to this enzyme: generate a proton motive force and to catalyze the ROS<sup>301</sup>.

Finally, our knowledge of the physiological role of cytochrome-bd-II is less definite. The complex consists of two subunits, AppC and AppB, which is akin to the two subunits of cytochrome-bd-I terminal oxidase<sup>302,303</sup>. Its expression becomes dominant during anaerobiosis, phosphate and carbon starvation, and entry into stationary phase<sup>302,304</sup>.

### **1.5.3.3 The ATP synthase**

The electron transport chain's final element is the ATP synthase (ATPase or complex V)<sup>305</sup>. This complex transforms the potential energy of the PMF into ATP<sup>305–307</sup>. The ATPase structure consists of a transmembrane F<sub>0</sub> complex that carries out the proton-translocation and the F<sub>1</sub> complex that catalyses the synthesis of ATP<sup>305</sup>. The F<sub>1</sub> complex consists of four different subunits ( $\alpha_3\beta_3\gamma\delta\epsilon$ ) while the F<sub>0</sub> region is usually formed by three different subunits ( $ab_2c_{9-15}$ )<sup>308</sup>. This complex's function is much like a rotary engine, in which protons descend through the F<sub>0</sub> complex, pushing the rotation of the c-ring<sup>305,308</sup>. Then, this rotation catalyses the synthesis of ATP from ADP and inorganic phosphate. Interestingly, in anaerobic conditions, this reaction can also play in reverse so that ATP is consumed to maintain a proton gradient, which can then be used to transport other metabolites or ions<sup>309</sup>. Moreover, recent improvements in live-cell imaging have revealed that the ATP synthase works in pulses of 10-80s and in turn, these pulses correspond to oscillations in the PMF<sup>310–312</sup>.

### **1.5.4 Metabolic oscillations**

The metabolism of *E. coli* comprises a myriad of interconnected enzymatic reactions. Thus, oscillatory dynamics emerge quite naturally from the interaction of multiple pathways. Early studies have established that metabolic oscillation can arise due to the allosteric effect between substrates and enzymes of different reactions or regulatory feedback loops<sup>313,314</sup>. This section will examine the emergence of oscillations in central carbon metabolism and cell growth.

#### **1.5.4.1 Carbon metabolism oscillations**

Glycolytic oscillations have been extensively studied in computational models. Most of these works suggest that the oscillatory behaviour originates from the allosteric effects on the enzyme phosphofructokinase<sup>313–315</sup>. However, it has also been suggested that the requirement of ATP for glycolysis might create a feedback

loop mechanism<sup>316–318</sup>. Logically, the characteristics of these oscillations (period and amplitude) depend on both external (environmental) and internal (genomic) factors<sup>319</sup>. For example, an in-silico model of *E. coli* glycolysis has demonstrated that a rise in external glucose leads to an increased wave amplitude and decreased frequency<sup>319</sup>. In addition, live monitoring of NAD(P)H and ATP levels within the cytoplasm showed a robust correlation between the frequency oscillations and the carbon source<sup>320,321</sup>. Surprisingly, the metabolic clock seems to run autonomously from the cell cycle.

#### **1.5.4.2 Cell growth oscillations**

The cell growth has an intrinsic cyclical component to it. The cell must uptake some nutrients, grow and divide. Thus, a sufficiently large number of cells require a coordinated behaviour to avoid competition for nutrients<sup>322</sup>. The best-studied case is biofilm growth waves, where the patch extension creates an asymmetric distribution of nutrients between the centre and edges. Here, the consumption of nutrients by peripheral cells starves the cells in the interior cells. Thus, the biofilm grows on waves so that nutrients can reach cells in the inner core.

It is worth noting that the coordination between cells happens via membrane potential depolarisation<sup>214,322</sup>. A decay in membrane potential can trigger a potassium signal via a potassium voltage-dependent channel. When the channel opens, cytoplasmic potassium decreases and local environmental potassium increases, depolarising neighbouring cells and propagating the signal<sup>213</sup>.

#### **1.5.5 Membrane potential modulation in bacteria**

As described in section 1.4.4, membrane potential depends on the gradient of ions across the membrane, particularly the proton motive force. Bacterial cells can use the membrane potential for metabolite transport (section 1.4.2), ATP synthesis

(section 1.5.3.3), flagellar motion or cell signalling. Interestingly, *in vivo* fluorescent measurements of the bacterial membrane potential showed cell-wide spikes consistent with electrical spiking, similar to that of firing neurons<sup>323</sup>. These spikes were abolished upon chemical disruption of the proton gradient or the electron transport chain perturbations, suggesting that the two processes were intrinsically coupled<sup>323</sup>. A major factor determining the membrane potential is the carbon source and carbon metabolism<sup>248</sup>. Cells growing on glucose have a lower membrane potential of  $\sim -100$  mV, compared to glycerol ( $\sim -140$  mV) or cells in the stationary phase<sup>248</sup>. Another mechanism of membrane potential modulation already discussed in this work is voltage-dependent channels (section 1.4.4). The most common example is the activation of the mechanosensitive channels<sup>324</sup>, see section 1.4.4.5. Finally, the last mechanism for membrane potential modulation is through ionophores. Still, this method does not appear to be very common. The main naturally occurring ionophore is indole, which is produced by  $\sim 100$  different bacterial species<sup>325–327</sup>.

#### **1.5.5.1 Indole effect on membrane potential**

Indole is a benzene-pyrrolic ring, which makes it a highly hydrophobic compound<sup>328</sup>. Therefore, it tends to accumulate in the lipidic membranes of the cells. Once there, this molecule can transport protons in favour of gradient<sup>329</sup>. In bacteria, indole synthesis occurs very quickly, which generates an indole pulse. This pulse depolarises the cell membrane while the indole propagates to neighbouring cells<sup>329–331</sup>. This signal has been correlated with stress resistance, antibiotic resistance, and biofilm regulation<sup>332–336</sup>. The regulation of the indole signal is controlled by the tryptophanase (TnaA), the enzyme that synthesises indole<sup>327</sup>.

### ***Indole regulation***

The tryptophanase catalyses the conversion of tryptophan into indole, pyruvate, and ammonia<sup>327</sup>. The TnaA expression is controlled by two promoters – the catabolite repression protein (CRP) and the TorR – and the TnaC binding factor<sup>337,338</sup>. The TnaC leader peptide blocks the ribosome in the absence of free tryptophan. Therefore, *tnaC* prevents the usage of internal tryptophan and only allows TnaA expression in the presence of tryptophan in the medium<sup>337</sup>. Once that condition is met, TnaA expression depends on its two promoters.

The first promoter, TorR, is the binding box of the two-component system TorR-S. This regulator has been associated with conditions in which *E. coli* is forced to use nitrate and nitrite as electron acceptors<sup>339</sup>. The use of these substrates generally entails high alkaline stress. Thus, the expression TnaA and, in turn, indole production could mitigate the alkaline stress, yet the precise mechanism is still unknown<sup>339</sup>.

The second promoter, CRP, triggers the expression of TnaA when the cell senses exhaustion of the glycolytic flux<sup>340</sup>. Therefore, when cells approach the stationary phase, the TnaA produces an indole pulse that depolarises the cells, pushing them into a dormant state<sup>331,341</sup>. This strategy reduces glucose consumption allowing cultures to survive for extended periods.

## **1.6 The study of single-cell microbiology**

Bacterial physiology has been the subject of endless fascination since the dawn of microbiology as a discipline. Already in the late 40s, Monod<sup>342</sup> started applying quantitative methods in the study of bacterial physiology. His approach was based on the rigorous study of population-level data from bulk cultures, which became the standard method for the whole discipline<sup>343</sup>. Although this technique rendered

very useful over the decades, the study of whole populations sometimes masks meaningful information from cell-to-cell heterogeneity, bacterial sub-populations, or variations within the cell<sup>344,345</sup>. Therefore, the use of light microscopy of living bacteria emerged as a viable alternative for single-cell analyses.

In order to study bacterial physiology with the microscope, one first has to solve the issue of how to maintain the cells alive when they are under the lens. A neat solution for this problem has been the use of agarose pads. These pads allow live imaging of cells over several cell division cycles (typically 4–5) and are an excellent tool for the study of biofilms<sup>346,347</sup>. For instance, this method enabled the discovery of the emergence of bacterial subpopulation during carbon starvation<sup>348</sup>, the stochastic expression of genes during antibiotic treatment<sup>349</sup>, and the role of voltage-activated channels in bacterial mechanosensation<sup>324</sup>.

Nevertheless, the thin agarose layer is prone to drying, limiting the experiments' duration. Experimental imaging during long periods is also hampered because individual cells start to overlap, difficulting the posterior data analysis<sup>344</sup>. Finally, it is unclear for how long exactly, if at all, steady-state growth conditions can be maintained on the pads<sup>345</sup>. Here, microfluidic devices have been able to provide a powerful solution.

### **1.6.1 Microfluidics devices for bacterial microbiology**

Microfluidic technology refers to the study and manipulation of fluids at the submillimetre length scale<sup>350</sup>. The application of microfluidic chemostats provides an ideal environment where the environmental conditions can be tightly controlled. They also keep individual cells in position for live-cell microscopy while the flow of the growth medium constantly provides cells with fresh nutrients and washes away metabolic byproducts and excess cells, thereby creating a highly uniform growth environment<sup>350</sup>. Under these conditions, bacterial physiology becomes isolated from the influence of environmental factors, permitting an

unimpeded view of the internal logic of cells. Moreover, the constant flow prevents the microfluidic device from becoming overcrowded, so observation of single-cell lineages for tens or hundreds of generations becomes possible<sup>351,352</sup>. Lastly, the medium composition flowing through the device can be altered at will, allowing cells to be observed as they respond to the onset of stress or the introduction or removal of a particular compound<sup>353,354</sup>.

### **1.6.2 Design and fabrication of microfluidics devices**

In order to create a microfluidic device, the first step is to design the template with a CAD (Computer-Aided Design) tool<sup>355</sup>. This design will then be carved out on a thin metal layer using a laser or an electron-beam mask writer. The resulting mask is exposed to ultraviolet light with a thin coating of a photoreactive polymer. Exposure to UV light transfers the pattern from the mask to the polymer; the unexposed photoresist is removed using an organic solvent, leaving behind the bas-relief structure in the polymer layer. The final mask serves as the microfluidics master template<sup>355</sup>.

The next step is the casting of the chip itself. A liquid polymer called polydimethylsiloxane (PDMS) is mixed and then poured onto the master template to make a chip replicate. Then, it is cured at a high temperature ( $\sim 100$  °C) for a few hours, which hardens the polymer, producing the chip with the engraved design. The use of PDMS has become the standard for most applications in microbiology because flexible, biocompatible, insulating, unreactive, transparent to ultraviolet and visible light, permeable to gases and only moderately water permeable<sup>356</sup>. The final step is bonding the PDMS chip to the glass cover slide. PDMS contains many methyl groups ( $-\text{CH}_3$ ) and is hence hydrophobic. However, its surface can be rendered hydrophilic by exposure to a plasma of air or oxygen to generate reactive silanol groups ( $-\text{SiOH}$ ) at the surface. When these radicals contact with clean,

oxidized glass, they form a covalent bond (Si-O-Si) between the layers. The bonding of PDMS to glass (or PDMS) makes it possible to form sealed microfluidic devices in which fluids can be pumped at pressures as high as 50 psi (~350 kPa) without failure<sup>355,356</sup>.

### **1.6.3 The mother machine**

From the many microfluidics designs, the most widespread is the mother machine platform<sup>352</sup>. In this device, bacteria grow in short (10–25  $\mu\text{m}$  long) dead-end channels. The main advantage of dead-end channels comes from a longer retention time of cells compared to open ends channels. In addition, the mother machine design allows clones of the mother cell to reside in the dead-end side of the channel. Finally, the number of cells is fixed because the flow in the main channel flushes away extra cells that grow out from the dead-end channels. The same flow also maintains a constant media environment in the growth channels by replenishing nutrients and removing metabolic waste products. Both exchanges are thought to occur via diffusion<sup>352</sup>.

This platform has been used to study cell aging<sup>352</sup>, cell cycle control<sup>357</sup>, and the effects of mechanical forces on cell wall growth<sup>358</sup>. The devices have also been used in studies of gene regulation<sup>344,351,354</sup> and antibiotic resistance<sup>353</sup>.

## Research Aims & Objectives

My research aims to understand the influence of the periplasmic ion environment on outer membrane permeability. I will focus on testing 3 hypotheses:

- A. The periplasmic ionic environment controls membrane permeability. If correct, we should be able to alter bacterial permeability through the modulation of the periplasmic environment.
- B. Bacteria have a dynamic periplasmic environment that responds to cellular metabolism. If true, we should find a correlation between the periplasmic ions and the carbon source supply. Consequently, if the periplasmic ions control permeability and these are dynamically regulated, then we should see that carbon source changes modulate permeability due to their impact on the ETC activity.
- C. Indole regulates membrane potential in response to changes in carbon source. If this hypothesis is correct, we should see varying indole synthesis in different carbon sources and different membrane potential.

With these questions in mind, I split the project into four sections:

- **Chapter 1:** To understand how different physiologically relevant ions affect the permeability of porins.
- **Chapter 2:** To investigate the regulation and homeostasis of the periplasmic ions and their correlation with the metabolic activity of the electron transport chain.
- **Chapter 3:** To examine the effect of carbon sources on the permeability of clinically relevant antibiotics.
- **Chapter 4:** To study the regulation and effect of the naturally produced membrane potential modulator indole.



# **Chapter 2: GENERAL METHODS**

## 2.1 Strains

### 2.1.1 Strains list

Table 1: List of strains used in this work.

Strain	Characteristic genotype features	source
E. coli DH5 $\alpha$	fhuA2::IS2 $\Delta$ (mmuP-mhpD)169 $\Delta$ phoA8 glnX44 $\phi$ 80d[ $\Delta$ lacZ58(M15)] rfbD1 gyrA96 luxS11 recA1 endA1 rphWT thiE1 hsdR17	NEB <sup>359</sup>
E. coli K12 BW25113 (WT)	$\Delta$ (araD-araB)567, $\Delta$ (lacA-lacZ)514(::kan), lacI <sup>p</sup> -4000(lacIq), $\lambda$ -, rpoS396(Am)?, rph-1, $\Delta$ (rhaD-rhaB)568, hsdR514	KEIO collection <sup>360</sup>
$\Delta$ ompF	BW25113 + $\Delta$ ompF746::kan	KEIO col. <sup>360</sup>
$\Delta$ ompC	BW25113 + $\Delta$ ompC768::kan	KEIO col. <sup>360</sup>
$\Delta$ ompG	BW25113 + $\Delta$ ompG756::kan	KEIO col. <sup>360</sup>
$\Delta$ nmpC	Not described	KEIO col. <sup>360</sup>
$\Delta$ phoE	BW25113 + $\Delta$ phoE759::kan	KEIO col. <sup>360</sup>
$\Delta$ kch	BW25113 + $\Delta$ kch-758::kan	KEIO col. <sup>360</sup>
$\Delta$ clcB	BW25113 + $\Delta$ clcB740::kan	KEIO col. <sup>360</sup>
$\Delta$ ptsH	BW25113 + $\Delta$ clcB740::kan	KEIO col. <sup>360</sup>
$\Delta$ aceA	BW25113 + $\Delta$ aceA732::kan	KEIO col. <sup>360</sup>
$\Delta$ tolC	BW25113 + $\Delta$ tolC732::kan	KEIO col. <sup>360</sup>
$\Delta$ tnaA	BW25113 + $\Delta$ tnaA739::kan	KEIO col. <sup>360</sup>
tnaA-GFP	BW25113 + tnaA-GFP:Km <sup>R</sup>	Gaimster <sup>361</sup>

All the strains in this work are derived from the *Escherichia coli* K12 BW25113. Long term stock cells were stored in 20% glycerol at -80 °C. Fresh inoculums were plated monthly in LB with or without antibiotics. Single colonies were resuspended in a 50 mL falcon tube with fresh Super-Optimal Broth (SOB) or minimal medium 9 (M9) for each experiment. The super-optimal broth was prepared following a premix recipe (Fromedium, SOB01CFG). To prepare the minimal medium, I followed the recipe described by Kotte<sup>362</sup> and supplemented it with 1 g/L casamino-acids, 1 mM tryptophan and the specified carbon source. The liquid cultures were incubated in glass test tubes with a breathable lid in a shaking incubator at 37°C. The list of plasmids used in this work can be found in Table 1.

## **2.2 Medium and growth conditions**

### **2.2.1 Rich medium**

The formulation Super Optimal Broth used in this work contains tryptone 35 g, yeast Extract 20 g, NaCl 5 g, 4N NaOH 12.5 mL (5 mM final concentration) per 1 L water (Milli-Q, Millipore). This recipe was prepared from the Fromedium premix (SOB01CFG). The LMB kitchen scientific facility prepared the medium.

### **2.2.2 Minimal medium composition and preparation**

The minimal medium used in this work is based on the M9 recipe described in Kotte<sup>362</sup>. The medium contained the following components: Base salt solution (211 mM Na<sub>2</sub>HPO<sub>4</sub>, 110 mM KH<sub>2</sub>PO<sub>4</sub>, 42.8 mM NaCl, 56.7 mM (NH<sub>4</sub>)<sub>2</sub>SO<sub>4</sub>, autoclaved and prepared by the scientific facilities at LMB), 10 mL of trace elements (final concentration: 0.63 mM ZnSO<sub>4</sub>, 0.7 mM CuCl<sub>2</sub>, 0.71 mM MnSO<sub>4</sub>, 0.76 mM CoCl<sub>2</sub>, autoclaved), 0.1 mL 1 M CaCl<sub>2</sub> solution (autoclaved, prepared by the scientific facilities at LMB) for a final concentration of 0.1 mM, 1 mL 1 M MgSO<sub>4</sub> solution (autoclaved, prepared by the scientific facilities at LMB) for a final concentration of 1 mM, 2 mL of 500x thiamine solution (1.4 mM in ultrapure water from Milli-Q, Millipore and filter sterilized) and 0.6 mL 0.1 M FeCl<sub>3</sub> solution (filter sterilized). The final volume was adjusted to 1 L with ultrapure water (Milli-Q, Millipore) lab water system (Milli-Q Advantage-10, Millipore). For each batch, the medium was filtered through 0.22 µm Millipore stericup and split into 500 mL bottles. The carbon source was added before each experiment.

The carbon sources used in this work were acquired from Sigma-Aldrich in powder form. Then, stock solutions were prepared at a 100 g/L concentration in Milli-Q water. After adjusting the pH to 7.0, 100 mL aliquots were filtrated with a syringe filter, 0.22 µm. For the lipid media preparation, I used 14 mg/L 1,2-

dipalmitoylphosphatidylcholine (DPPC), combined with 0.3 g/L casitone and 0.05% Tyloxapol to allow proper dilution.

When indicated, bacterial cultures were supplemented with casamino acids and tryptophan. The stock reservoir was prepared by dissolving 5 g casamino acids (Difco) and dissolving it in 50 mL Milli-Q water, making a final concentration of 100 g/L. The stock solution was filtered with a syringe filter, 0.22  $\mu\text{m}$  and stored at 4 °C. Tryptophan was acquired as a powder (Sigma Aldrich) and dissolved in Milli-Q water to a 50 mM concentration. After this, the solution was filtrated with a syringe filter, 0.22  $\mu\text{m}$  and stored at 4 °C.

### **2.2.3 Growth conditions**

Bacterial cultures were resuscitated from a – 80 °C 20 % glycerol stock to an LB agar plate. A selection marker was included in the medium if required. The kitchen facilities at the LMB provided the plates. The plate cultures were grown overnight at 37 °C. Once colonies were formed, the plates were stored in the fridge (set at 4 °C) and sealed with parafilm. After every use, plates were re-sealed with parafilm. The stock plates were discarded after 6 weeks.

For each experiment, overnight cultures were inoculated from single colonies using autoclaved wooded toothpicks (LMB facilities). The colony was inoculated in 5 mL of the specified medium and grown overnight at 37 °C in an orbital shaker at 300 rpm.

## **2.3 Cloning of fluorescent reporters**

### **2.3.1 Cloning techniques**

All the plasmids presented in this work were constructed using Gibson assembly<sup>363</sup>. All DNA templates were acquired through Addgene (see Table 2). The primers were designed with the Primer3 algorithm available through the Benchling

platform<sup>364</sup>. The DNA material was amplified by PCR with the PrimeStart HS polymerase kit (Takara), following the manufacturer protocol adjusting the annealing temperature to the suggested by the Benchling cloning algorithm. The amplification cycles were repeated 35 times using a C1000 Touch Thermal Cycler (BioRand).

The resulting DNA fragments were ligated with the following Gibson assembly kit. The concentration of the DNA templates was estimated with UV absorption using a NanoDrop 3300 (ThermoFisher), and the NEBcalculator helped us estimate the required volumes for the Gibson assembly. All assemblies were carried out for 1h at 50 °C using the same thermocycler as the PCR amplification.

Bacterial transformation of the assembled sequence was carried out through a heat-shock using *E. coli* DH5 $\alpha$  as an intermediate strain. Once I verified the plasmid sequence with colony PCR, I inoculated a single colony in a falcon tube with SOB medium to extract the plasmid the next day. Isolated plasmids were stored at -20 °C in Qiagen Elution Buffer. Target strains were electroporated as required for my experimental work.

### 2.3.2 Genetic material

Table 2: List of plasmids used for this work.

Plasmid name	Reporter	marker	promoter	background genotype	source
pSCM001	pHluorin	Amp <sup>R</sup>	araBAD	pBAD-TOPO	Previous work <sup>329</sup>
pSCM002	pHluorin	Chl <sup>R</sup>	araBAD	pBAD-TOPO	Previous work <sup>365</sup>
SLF0079	QuasAr2	Amp <sup>R</sup>	araBAD	pBAD-TOPO	Addgene <sup>366</sup>
pBAD-GINKO1	GINKO1	Amp <sup>R</sup>	araBAD	pBAD-TOPO	Addgene <sup>367</sup>
GCamp6	GCaMpf6	Amp <sup>R</sup>	Sigma 70 promoter	BB118	Donation from Kralj lab
pBAD-ArchT (Chl)	ArchT	Chl <sup>R</sup>	araBAD	pBAD-TOPO	This work. Material from addgene <sup>368</sup>
pBAD-ArchT (Amp)	ArchT	Amp <sup>R</sup>	araBAD	pBAD-TOPO	This work. Material from addgene <sup>368</sup>
pBAD-pelBCpHuji	pelBCpHuji	Amp <sup>R</sup>	araBAD	pBAD-TOPO	This work. Material from addgene <sup>369,370</sup>

All the plasmid and genetic material used in this work can be found in Table 2. Plasmids were stored in DH5 $\alpha$  frozen in -80 °C 20 % glycerol stock. Also, minipreps aliquots using Elution Buffer (H<sub>2</sub>O 10 mM Tris-Cl, pH 8.5) as a solvent for routine cloning were stored in the freezer at -20 °C.

All the primers were acquired from Sigma-Aldrich, dissolved in Milli-Q water, and stored at -80 °C.

Table 3: List of primers used in this work.

name	Sequence (5'-3')
pBAD_fwd	GCCACCCGCAGTTCGAAAAATAAGTTTAAACGGTCTCCAGCTT
pBAD_rev	GCGGTCGGCAGCAGGTA CTTCATGGGTATGTATATCTCCTTCTTAAAG
pebB_fwd	AGAAGGAGATATACATACCCATGAAGTACCTGCTGCCGACCG
pebB_rev	TGATGATGAGAACCCCCATGGCCGGCTGGGCGGCCAGCA
pebB_pHuji_fwd	TGCTGGCCGCCAGCCGGCCATGGGGGGTTCTCATCATCA
pebB_pHuji_rev	AAGCTGGAGACCGTTTAACTTACTTGTACAGCTCGTCCATG
ArchT_fwd	AGGAGATATACATACCCATGATGGACCCAATTGCACTGCAGGCCGGGG
ArchT_rev	AGCCAAGCTGGAGACCGTTTTTACACGGCGGCCGAGGCTCCGGGGCTTCCGT A

## 2.4 Chemicals and probes

### 2.4.1 Antibiotics

All antibiotics in Table 4 except ciprofloxacin were used for the selective growth of strains carrying specific antibiotic-resistant genes.

Table 4: Antibiotics used for this work.

Antibiotic	Provider	Stock Conc.	Solvent
Ampicillin	Formedium	100 mg/mL	Milli-Q water
Kanamycin	Sigma-Aldrich	25 mg/mL	Ethanol
Chloramphenicol	Sigma-Aldrich	50 mg/mL	Milli-Q water
Ciprofloxacin	Sigma-Aldrich	1.25 mg/mL	Milli-Q water, 0.1 N HCl
Colistin	Sigma-Aldrich	50 mg/mL	Milli-Q water

### 2.4.2 Ionophores and other chemicals

Table 5: Ionophores used for this work.

Name	Provider	Stock Conc.	Work Conc.	Solvent
CCCP	Sigma-Aldrich	50 mM	0.25 mM	Ethanol
Valinomycin	Sigma-Aldrich	100 mM	0.1 mM	Ethanol
Nigericin	Sigma-Aldrich	100 mM	0.1 mM	Ethanol
Indole	Sigma-Aldrich	50 mM	5 mM	Ethanol
PMBN	Sigma-Aldrich	5 mM	0.05 mM	Ethanol
Oligomycin	Sigma-Aldrich	10 mM	0.1 mM	Ethanol

### 2.4.3 Fluorescent probes

Table 6: List of fluorescent probes used for this work.

Name	Provider	Stock Conc.	Work Conc.	Solvent
2NBDG	Thermo-fisher	5 mg/mL	20 µg/mL	Milli-Q water
Bocillin-FL	Thermo-fisher	1 mg/mL	1 µg/mL	Milli-Q water
Hoechst 33342	Invitrogen	10 mg/mL	10 µg/mL	Pre-dissolved
Oregon Green	Thermo-fisher	1 mg/mL	20 µg/mL	Milli-Q water
Thioflavin T	Sigma-Aldrich	10 mM	10 µM	Milli-Q water
Oxonol-VI	Sigma-Aldrich	1 mM	10 µM	Ethanol

All fluorophores were stored at -20 °C and split into 200 µL aliquots. For each experiment, aliquots were defrosted and stored at 4 °C for a week.

In addition, I have listed a table with all the details of the illumination conditions used for each fluorophore (Table 7).

Table 7: Illumination condition for each fluorophore.

Name	Excitation (nm)	Emmision
2NBDG	488	510/25
Bocillin-FL	488	510/25
Hoechst 33342	405	450/25
Oregon Green	405	510/25
Thioflavin T	430/30	480/25
Oxonol-VI	561	615/25

## 2.5 Microfluidics

### 2.5.1 Chip design

I used the Mother Machine design described by Wang<sup>352,371</sup>. The microfluidic device was fabricated from an epoxy master template courtesy of Dr Jehangir Cama (University of Cambridge/University of Exeter, UK). The Mother Machine consists of a feed trench (50  $\mu\text{m}$  x 100  $\mu\text{m}$  x 30 mm) with many channels (1.4  $\mu\text{m}$  x 1.4  $\mu\text{m}$  x 25  $\mu\text{m}$ ) attached perpendicular to the trench. These channels hold the cells, and media is supplied to the cells via the trench (see Figure 2.1).

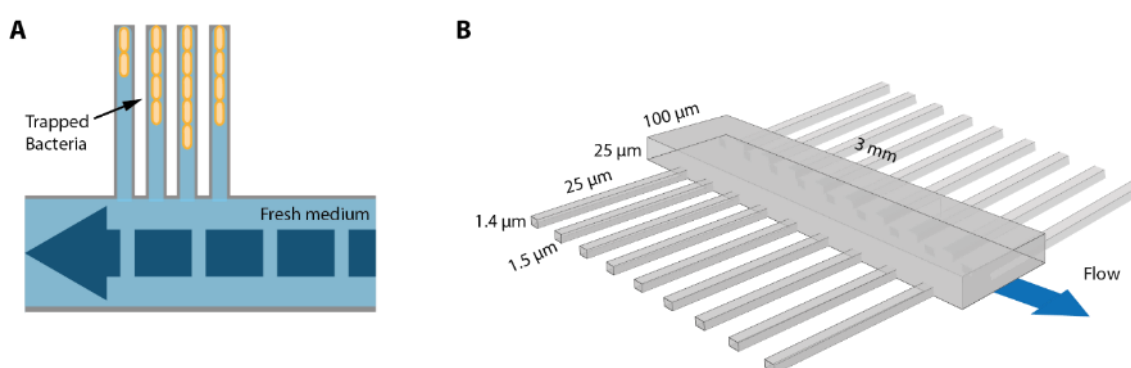


Figure 2.1: Diagram of the Mother Machine.

A) Schematic illustration of the microfluidic Mother Machine. The old-pole mother cell is trapped at the end of the growth channel. B) Isometric schematics of microfluidic channels in which individual bacteria are held. Channels connect to a larger channel through which medium is continuously replaced, and excess cells are washed away

### **2.5.2 Chip preparation**

For each batch of 12 chips, 50 mL of PMDS were mixed with a 5 mL curing agent (10:1) with vigorous stirring. The bubbles formed during the mixing were removed by vacuum degassing for 20 min until all air bubbles disappeared. Then, the gel was poured onto the master template and baked at 65 °C for 1 h. Subsequently, the chip was cut out around the wafer and prepared for bonding with the cover slide. Holes for inlets and outlets were punched using a sharpened 0.6 mm biopsy puncher (from Fisher Scientific), and the chip was cleaned with Scotch tape and 2-propanol. After drying all the excess isopropanol, the coverslip and PDMS with the features upwards were exposed to air plasma in a vacuum for 20 s at 0.4 mBar Oxygen (PlasmaPrep2, Gala Instrumente). This process activated PDMS, which was put on a glass coverslip (24 mm x 50 mm, thickness 0.17 mm+/-0.005, Carl Roth). Finally, the chips were incubated overnight at 65 °C.

Once the chip was ready, I flushed the chamber with 2-iso-propanol and sonicated the chip for 30 min to remove all the debris (FB50, Fisher-Scientific). Then, I coated the internal chip surface to facilitate bacterial attachment with a passivation buffer. The passivation buffer contained 10 mg/mL Bovine Serum Albumin and 10 mg/mL Salmond Sperm in a 3:1 ratio<sup>352</sup>. The process was carried out overnight. Finally, the chips were stored in a dry cupboard for a week until their use.

### **2.5.3 Cell trapping in chip**

The preparation of the bacteria started with an overnight culture in the specified medium. Before injecting the cells in the microchip, 2 mL of cells were washed by centrifugation (Eppendorf 5810R) and resuspended in 2 mL of fresh medium. These cells were incubated for 10 min after and then centrifuged and concentrated to 100 µL. This high-density culture was injected into the microfluidic

chip and set in a plate shaker at 37 °C for 15 min at 300 rpm (Grant-bio, PHMP). Once the cells were trapped in the channels, the chip was connected with an inlet and outlet tubing (Tygon ND-100-80 Medical Tubing - 0.5 mm ID, 1.52 mm OD). Next, I flushed the chip with plain M9 for 10 min so that any cells remaining in the main channel were removed.

## **2.6 Statistical analysis and data analysis**

All the scripts used for the analysis throughout this thesis are available at [www.github.com/phisanti/phd\\_thesis](http://www.github.com/phisanti/phd_thesis).

## **2.7 Statistical analysis**

All statistical analyses, including data plotting, data transformations and models, were performed with the R programming toolkit. The scripts were written on the RStudio IDE. All scripts can be found at [www.github.com/phisanti/phd\\_thesis](http://www.github.com/phisanti/phd_thesis).

Moreover, unless the contrary is indicated, all the experiments were performed on at least three independent occasions (biological replicates) and a minimum of three technical replicates. Also, for every figure, the uncertainty intervals are described with the standard error. This measurement allowed us to accurate estimates of the sample mean.

## **2.8 Image analysis**

All movies were analysed with the ImageJ suite (v1.58) using custom python scripts. The scripts consisted of image registration (module: Template matching, v 2019.06.24.090951), image segmentation (module: Weka Segmentation, v 3.2.35<sup>372</sup>), and cell tracking (module: TrackMate, v7<sup>373</sup>). Once the pixel intensity was measured, I analysed the data within the Rstudio suite.



# **Chapter 3: PERIPLASMIC IONS MODULATE BACTERIAL PERMEABILITY**

## Summary

Lipid bilayer studies of bacterial porins have suggested the dynamic regulation of conductance due to changes in the ionic environment. Thus, in this chapter, I examine the effect of internal ions on porin permeability *in vivo*.

Using a flow cytometry method, I found that the main contributors to membrane permeability are the OmpF and OmpC porins. Then, I assessed the impact of a wide range of ionophores, finding CCCP and valinomycin as potent modulators of permeability. Treating the cells with these ionophores to clamp the internal levels of H<sup>+</sup> and K<sup>+</sup>, I observed that low proton or high potassium concentrations increased permeability. Replication of this work with the porin knock-out (KO) revealed that the potassium influence disappeared in the  $\Delta ompC$  strain, while the proton effect was present in all porin KO strains.

Next, expressing an optically activated proton pump (ArchT), I modulated the periplasmic pH at the single-cell level. Simultaneous expression with a fluorescent pH sensor showed that light activation of ArchT caused a proton flux. Using a microfluidic device, I showed that decreasing the periplasmic pH reduced the cellular uptake of porin dependent fluorescent markers.

Finally, I complemented my empirical observation with a molecular dynamic simulation of OmpF and OmpC at different protonation states. This work revealed that protonation of periplasmic residues caused a pore contraction.

In view of the above, our data suggest that *E. coli* permeability depends on the ion concentration associated with cells. Particularly, I provided evidence for the effect of changes in pH and potassium on membrane permeability.

*I have performed all the experiments and analyses described in this section except for the molecular dynamic simulation. This work was done by Ali Al-Sulami, PhD student in Prof. Sir Tom Blundell's Lab (Department of Biochemistry).*

## Introduction

Porin reconstitution in lipid bilayers or vesicles has been the dominant technique to study the permeability properties of porins. This type of experiment helped to reveal the exclusion size<sup>374</sup>, charge bias<sup>83,87</sup>, and the impact of membrane potential across the pore<sup>86,90,197</sup>. Recently, Cama et al. have developed an optofluidic assay for *in-situ* measurement of auto-fluorescent drug uptake in porin reconstituted on liposomes, showing the effect of pH on permeability<sup>375</sup>.

Nevertheless, the relevance of these findings to the physiology of living bacteria remains poorly understood. The best-studied case is the impact of cations on the permeation of penicillin derivatives through OmpC, where increases in salt concentration in the media lead to increases in permeability<sup>102</sup>. However, the mechanics of this phenomenon at the single-cell level are not completely clear. The aim of this chapter, therefore, is to explore the role of electrophysiological changes on the permeability of live *E. coli* cells, thus addressing objective A of this thesis.

To achieve this, I developed two main strategies: a flow cytometry assay to estimate permeability on several conditions and a microfluidic chip to monitor single-cell permeability *in situ*. I used the flow cytometry method to explore the relation between membrane permeability and ion gradients within the bacterium. The method deployed in this work was based on the reports by Jarzembowski, Hamilton and Jeon<sup>376–378</sup>. Briefly, they used fluorescent-tagged biomolecules such as Bocillin FL (Bodipy-tagged penicillin) or 2NBDG (2-(N-(7-Nitrobenz-2-oxa-1,3-diazol-4-yl)Amino)-2-Deoxyglucose, a green fluorescent glucose analogue) and used the increase in cell fluorescence as a proxy for bacterial uptake of the compound. In addition, flow cytometry allows the analysis of individual cells and large bacterial populations.

Then, I combined the precise control of medium conditions within the microfluidic chip with an optically activated proton pump to confirm my findings at the single-cell level. Genetically encoded optogenetic tools enable the specific modulation of ion channels at the single-cell level<sup>368,379</sup>. The main proteins used for this purpose are microbial opsins. These are transmembrane channels with a retinal co-factor in the centre of the channel<sup>368,379</sup>. When the retinal molecule absorbs light, it triggers a change in conformation that pumps ions across the membrane<sup>380</sup>. In 2011, the optically activated proton pump Arch was published as a tool that induces transiently and repeatedly proton pump in response to light exposure<sup>368</sup>. In general, these proteins are deployed in order to control neuron silencing and action potentials<sup>368,379</sup>, so for the first time, we express them with the aim to control and study the bacterial membrane potential.

Finally, we provide computational evidence from a molecular dynamics simulation to protonate the periplasmic residues of the porins OmpF and OmpC. The data suggest that protonating the periplasmic residues at pH 3 leads to a change in conformation that reduces the pore diameter. This change will then support the reduction of permeability observed in the empirical assays.

## **Material and methods**

### **3.1 Flow cytometry protocol for permeability estimation**

The development of the method for permeability estimation in bacteria was fundamentally derived from Jarzembowski, Hamilton and Jeon<sup>376–378</sup>. In brief, a bacteria culture was set overnight at 37 °C in minimal medium M9, supplemented with casamino acids 1 g/L, tryptophan 1 mM and glucose 1 g/L. Glucose was not added to the medium for 2NBDG experiments. The next day, aliquots of the parent culture were diluted to an OD~0.05 in the same fresh medium. The total volume was 25 mL and placed in a 250 mL conical flask. When the cultures' turbidity reached an OD of 0.1-0.25, the bacteria were split in a 96-well U-shape plate with 180 µL per well. Here, I added 10 µL of the treatment stock solution, sealed the plate with gas-permeable film (4titude, PCR0548) and returned it to the incubator. After 30 min, I added 10 µL of the fluorescent tracer from the reservoir. The concentration of the fluorescent tracer in the reservoir was diluted so that I could keep the final volume constant. After adding the fluorescent probe, the plate was returned to incubation for a specified time. Next, 200 µL were transferred to a V-bottom 96-well plate (Costar), and it was centrifuged 5 min x3900 rpm (Eppendorf 5810R, rotor S-4-104) and washed twice with PBS. Finally, samples were fixed and resuspended in PBS + 4% formaldehyde, stored at 4 °C and analysed after 16 h. Then, I used iCyt Eclipse (Sony) to read the fluorescence from the samples. This device is equipped with 488 nm, 561 nm and 642 nm laser sources along with Hoechst and FITC filter sets.

The data was analysed using the R programming language (see section 2.6). In order to control for the cell size effect on the uptake of the fluorescent tracer, the fluorescent signal of the tracer was divided by the forward scatter (FSC) signal as

this is proportional to cell size<sup>381</sup>. Then, I subtracted the fluorescent intensity value of cells without tracer, considering it as the background.

### **3.2 Treatment optimisation**

Ionophore dosage was optimised by measuring the effect of different concentrations on the membrane potential. First, a bacteria culture was set overnight at 37 °C in minimal medium M9, supplemented with casamino acids 1 g/L, tryptophan 1 mM and glucose 1 g/L. This sample was set overnight at 37 °C in minimal. The next day, an aliquot was diluted to an OD ~ 0.05 and the cultures were returned to the incubator until they reached exponential phase, defined as turbidity between 0.15 and 0.25 OD. At that point, cultures were split in a 96-well plate, flat-bottom for fluorometric assays ( $\mu$ CLEAR, Greiner-bio-one). To each well, I added Thioflavin T (ThT, T3516, Sigma-Aldrich) to a final concentration of 10  $\mu$ M. This fluorophore served as a proxy for membrane potential, as described by Prindle<sup>213</sup>. After adding the ThT, the plate was transferred to a plate reader with orbital shaking and temperature at 37 °C (ClarioStar, BGM LABTECH) for 60 min to allow marker uptake. Then, I took the plate out to add 10  $\mu$ L of the diluted ionophore to each well and transferred the plate back to the plate reader. The intermediate dilution was done in a 96-well plate to reach the desired concentration. The ThT fluorescence was monitored with a CFP filter set 430/20 and 480/20.

### **3.3 Cloning and expression of ArchT**

A pBAD-TOPO vector was employed to express ArchT on *E. coli* K-12 BW25113 cells. In this system, the target gene is cloned into the plasmid under a pBAD promoter sequence (Figure 3.1). Therefore, I could modulate expression through the addition of L-arabinose to the medium. All the strains employed in this work have the  $\Delta$ (araD-araB)<sub>567</sub> mutation (see Table 3); hence this system delivered a tight-controlled expression.



**Figure 3.1: Expression vector pBAD-archT.**

The backbone of this expression system is the pBAD-TOPO which is specifically designed for one-step cloning. The pBAD promoter, along with a T7 ribosomal binding site, controls the expression of the target protein. Thus, expression can be modulated with different L-arabinose concentrations.

The expression system was built using a Gibson assembly protocol<sup>363</sup>. The backbone was amplified using the pSCM001 as a template, and pLenti-CaMKIIa-eArch 3.0-EYFP was used for the ArchT amplification<sup>329,368</sup>. The PCR protocol for the amplification is described in see section 2.3.1. The fragments were validated by DNA electrophoresis. Then, all the DNA parts were assembled using the Gibson assembly kit (kit number E2611, NEB<sup>363</sup>). Finally, the resulting construct was transferred to *E. coli* DH5 $\alpha$  through conventional heat<sup>382</sup>. The next day, colonies

from the positive plate were surveyed with colony PCR using the ArchT primers, and the size was verified with DNA electrophoresis. Finally, the insert sequence was also confirmed via Sanger Sequencing.

### **3.4 ArchT validation**

In order to validate that the ArchT proton pump was operating correctly, cells were transformed with the pBAD-ArchT and the pSCM002 (expressing the pHluorin sensor under arabinose promoter) simultaneously. This setup allowed us to measure changes in cytoplasmic pH while activating the ArchT proton pump. Thus, we grew the cells overnight in SOB supplemented with 0.002 g/L arabinose and 20  $\mu$ M retinal. Ampicillin and chloramphenicol were used to select for both plasmids. Retinal is a cofactor essential for ArchT to work<sup>368</sup>. The following day, I washed the cells with M9 via centrifugation and resuspended them in M9 + 2 g/L glucose. Then, I transfer 1  $\mu$ L of the cells onto a 1,5 % agarose pad<sup>346</sup>. Agarose pads were prepared by mixing PBS + 1 g/L glucose + 1,5 % agarose. Then it was poured into a petri dish, and once dried, disks were cut out with a 6-mm diameter puncher (Harris, Uni-Core-6.00). Once the agarose pads with the cells were dried, they were put on top of a cover slide, as explained by Jong<sup>346</sup>.

### **3.5 2NBDG uptake in the Mother Machine**

For ArchT or QuasAr2 expressing cells, the medium was supplemented with 20  $\mu$ M retinal, 100  $\mu$ g/mL ampicillin and 0.0002 % arabinose, whereas WT cultures were only supplemented with retinal in the same concentration. I then trapped the cells into the Mother Machine as described in 2.5.3. Then, I wash the cells for 30 with plain M9. The flow was set constant at 0.15 mL/h with a syringe pusher (Harvard Apparatus). After the cleansing process, I switched the syringe to the appropriate medium 2 min before the recording and increased the flow to 1 mL/h. Thus, the new medium consistently arrived at the 10<sup>th</sup> minute of the recording. After 15 minutes of recording, I steadily decreased the flow back to 0.15 mL/h.

Then, 2NBDG permeability was estimated by measuring the increase of fluorescent signal of *E. coli* cells trapped in the Mother Machine side channels. The recording set up of the 2NBDG movies was done in a Nikon-N STORM, with a CCD camera (Andor-DU-897) and a 100x/1.49NA lens. The microscope had a closed environment chamber to maintain the temperature constant at 37 °C. For illumination, I used a 488-nm and 561-nm laser light (Aligent Technologies, MLC-400B). The 2NBDG fluorescent signal was captured with a dichroic mirror 525/50 (TRF49909), and for the 561-nm laser excitation experiments, I used a quad-band filter (97335) in combination with a 525/50nm filter.

### **3.6 Molecular dynamics simulation**

This work was performed in collaboration with Tom Blundell's lab by Ali Alsulami. All simulations were performed by GROMACS v4.6 ([www.gromacs.org](http://www.gromacs.org)) with CHARMM36 force fields for 100ns. The trimeric OmpC (2J1N, resolution 2.0 Å, with 346 amino acid residues) and OmpF (2OMF, resolution 2.40 Å, with 340 amino acid residues) was used in this experiment. Both systems were prepared using the CHARMM-GUI web interface. The OmpC 2J1N periplasmic side chains (E2, E43, E189, K6, K308, D7, D48, D135, D141, D268) and OmpF 2OMF side chains (E2, E48, E183, K6, K10, D7, D54, D92, D149, D266, K305) were protonated based on  $pK_a$  value calculated using PROPKA3<sup>383</sup>, whereas all other residues were set as a common state at physiological pH. The OPM server was used for orientation and positioning the protein in the membrane, and each system was embedded in a pre-equilibrated neutral zwitterionic lipid phosphatidylcholine (POPC) bilayer. All the simulations were performed at constant pressure (1 atm) and temperature (300 K). The results were analysed by code written by Ali Alsulami. This code can also be found at [www.github.com/phisanti/phd\\_thesis](http://www.github.com/phisanti/phd_thesis). Molecular graphic images were prepared using PyMol.

## Results

### 3.7 Optimisation of bacterial permeability assay

To quantify porin permeability, I employ a method based on the flow cytometry measurement of the uptake of fluorescent compounds<sup>376–378</sup>. The rationale is that short exposure of the bacteria to a fluorescent compound allows for a limited time uptake. Thus, the fluorescence detected with the flow cytometer is proportional to the bacterial permeability.

Thus, cells were grown in M9 supplemented with glucose 1 g/L + casamino acids 1 g/L and 1 mM tryptophan. When the cultures reached the exponential phase (OD 0.1-0.3), I added a fluorescent tracer. The compounds used in this study were fluorescent penicillin derivative Bocillin FL (BFL), the DNA dye Hoechst 33342 (Hoechst), the glucose analogue 2-(N-(7-Nitrobenz-2-oxa-1,3-diazol-4-yl)Amino)-2-Deoxyglucose (2NBDG), and Oregon Green (see Table 6 for further reference). All these compounds have been previously used in the study of bacterial permeability<sup>377,384–386</sup>. In addition, two of them (2NBDG and Bocillin) resemble relevant biological molecules (glucose and penicillin, respectively). After washing and fixing the cells, I measured the cell fluorescence via flow cytometry (section 3.1).

To evaluate this method, I exposed the cells of a range of tracer concentrations. Here I found that the tracer fluorescence was increased with the external concentration (**Figure 3.2**). Thus, I set the optimal concentration of each tracer as described in Table 6. In general, the optimal concentration was set to the midpoint of the sigmoidal curve (see red line in **Figure 3.2**) in such a way that changes in FL concentration were proportional to changes in fluorescence in an approximately linear fashion. It is relevant to point out that the detection of Oregon Green required a much higher concentration relative to the other tested compounds (**Figure 3.2, H**).

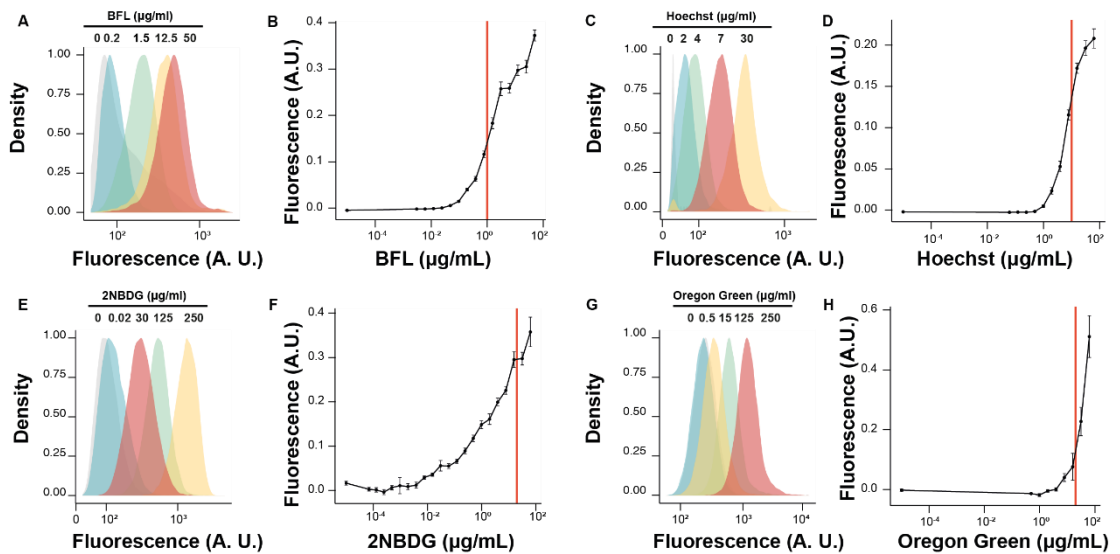


**Figure 3.2: Tracer uptake by bacteria depends on external concentration.**

Fluorescence tracer uptake after 15 minutes by *E. coli* growing in supplemented M9 (section 2.2.2). (A, C, E, G) Increase of raw fluorescence for the fluorescent tracers. The concentration for each histogram is indicated on the top. The X-axis indicates the raw fluorescence detected on the cells-gate, while the Y-axis represents the relative counts for each histogram. (B, D, F, H) Correlation between corrected signal and tracer concentration. Fluorescence was corrected by dividing the fluorescent signal by the forward scatter channel (FSC) signal to compensate by the cell size, and then it was subtracted the background fluorescence (cells signal without tracer). Then the geometric average of the histogram was averaged across replicates for each point. Error bars indicate the standard error. The red line indicates the optimal concentration used throughout the rest of this project.

### 3.7.1 Time optimisation of bacterial permeability assay

After setting the working concentration for each tracer (see red line in Figure 3.2), I studied the time course for their uptake. For this, I added the optimised amount of each tracer (see Table 6) and then incubated the cells for incremental periods. The results revealed that for three of the 4 tested compounds, the uptake flattened after 15 min (Figure 3.3). Therefore, I fixed the optimal duration of the uptake assay as 15 min. The only noticeable exception was the uptake of Oregon Green which peaked at 40 min and then started to decrease (Figure 3.3).

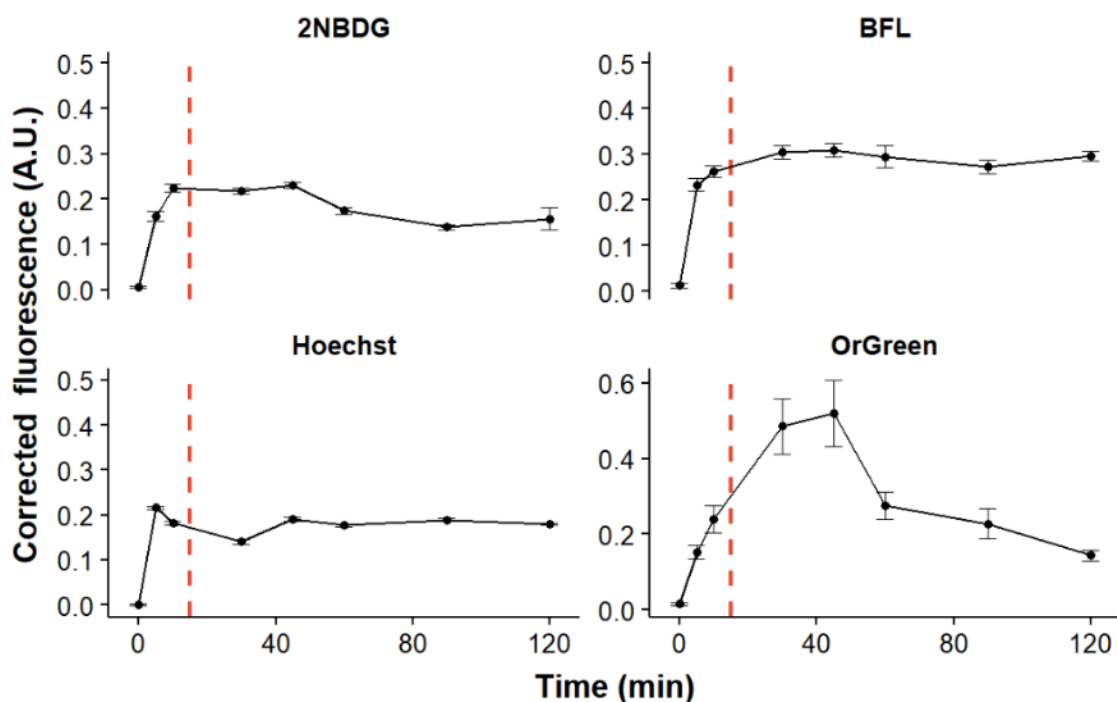


Figure 3.3: Fluorescence tracer uptake over time.

The figure shows the relationship between the tracer uptake (Corrected fluorescence) and time (section 2.2.2). As before, corrected fluorescence was calculated by dividing the tracer fluorescence by the FSC and background subtraction. The red line indicates the optimal time point for the final experimental conditions for further experiments. Notice that all the tracers reach the plateau at approximately 15 min with the exception of Oregon Green.

### 3.7.2 Porin deletion decreases 2NBD, BFL and Hoechst uptake

Once I had established a robust assay to measure bacterial permeability, I aimed to confirm that porins mediated the uptake of these fluorescent tracers. Therefore, I measure porin permeability with the optimized assay (see Figure 3.4). In addition, due to my interest in the participation of ions in bacterial permeability, I added KO strains involved in regulating membrane potential (see Table 1 for the complete genotype details). These included the ion channels ClcB (Cl<sup>-</sup> channel, section 1.4.4.4) and Kch (K<sup>+</sup> channel, section 1.4.4.2), along with the tryptophanase (TnaA, section 1.5.5.1) due to its role in membrane depolarisation.

My results suggested that all knock-out strains included in this study significantly affected 2NBDG uptake (Figure 3.4). In addition, BFL uptake was affected by the deletion of the porins OmpF, OmpC, OmpG, and the putative membrane protein

NmpC (Figure 3.4). Interestingly, the deletion of the ion channels ClcB and Kch also affected BFL uptake (Figure 3.4). Finally, Hoechst uptake was clearly affected by the deletion of all studied strains except TnaA (Figure 3.4). Nevertheless, I did not find any effect of porin deletion on Oregon Green permeability. Thus, I discarded this compound for further study (Figure 3.4).

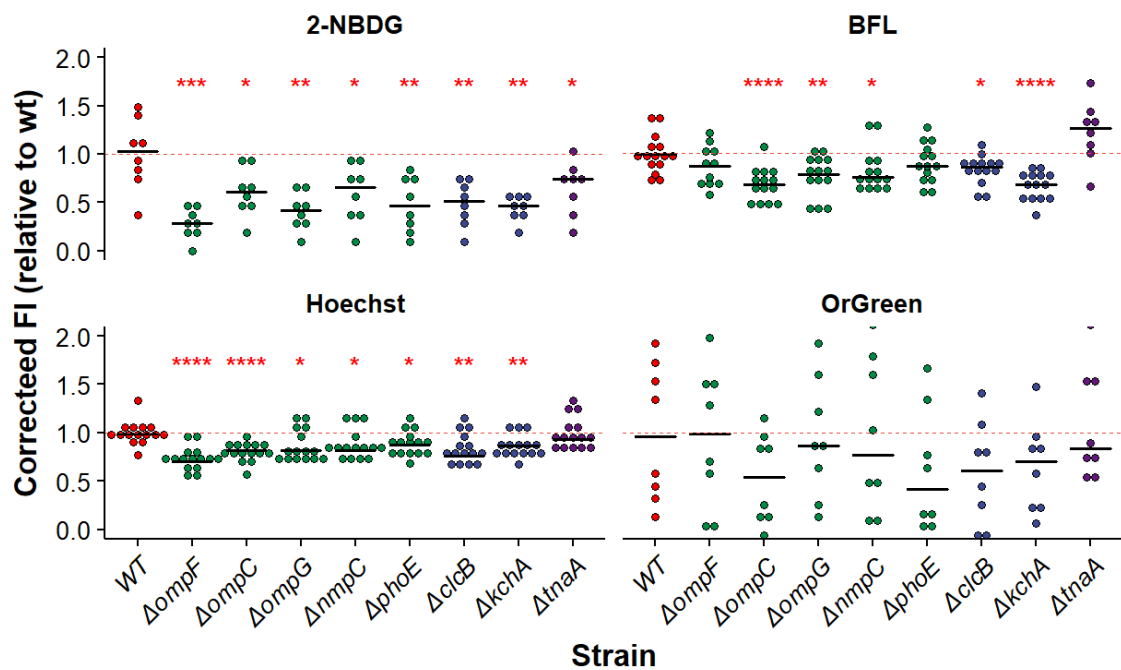


Figure 3.4: Fluorescent tracer uptake is mediated by porins.

Fluorescence tracer uptake after 15 min by *E. coli* mutants growing in supplemented M9 (section 2.2.2). Each dot represents the geometric mean of a biological replicate. The black line indicates the mean value for each strain. The statistical significance was evaluated with a t-test using the WT strain as the reference group. Here, one star denotes p-val. < 0.05, two stars p-val. < 0.01, three stars p-val. < 0.001, and four-stars p-val. < 0.0001. Corrected fluorescence was calculated by dividing the fluorescent signal by the FSC signal to compensate by the cell size, and then I subtracted the background fluorescence (cells signal without tracer). For all the panels, the dashed line indicated the mean WT value.

## 3.8 Ionophore effect on membrane potential

### 3.8.1 Ionophore optimisation

Next, I aimed to determine the influence of individual ions on membrane permeability. For that purpose, I treated cells with different ionophores before adding the fluorescent tracer. In order to determine the optimal concentration for each ionophore, I tested the effect on general membrane potential. To that end, I stained the exponentially growing cells with 10  $\mu\text{M}$  of Thioflavin T (ThT). The fluorescence of this compound increases when the membrane potential decreases (hyperpolarisation)<sup>213</sup>. After 1 h of equilibration, I treated the cells with different ionophore concentrations and measured the ThT fluorescence change (Figure 3.5).

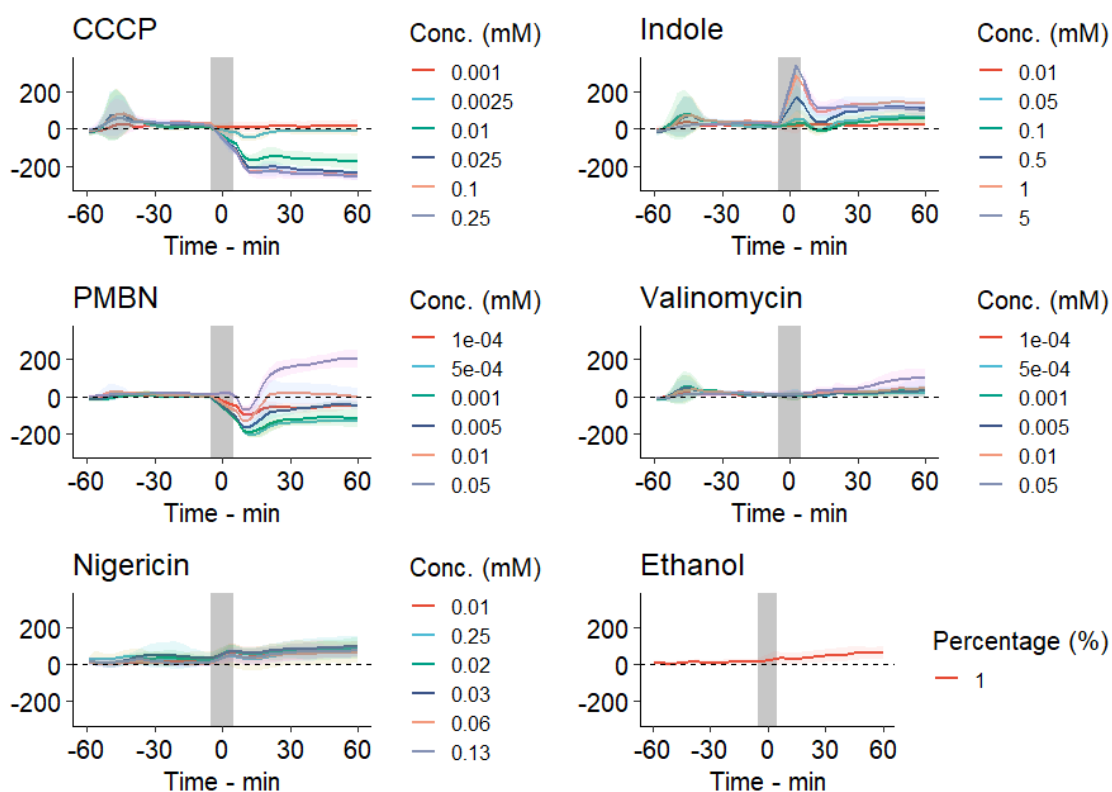


Figure 3.5: Ionophore treatments impact membrane potential.

The y-axis denotes the relative fluorescence of each treatment compared to control (PBS). The dark coloured line represents the average and the shaded area the standard deviation. The grey vertical line represents the time point when the ionophore was added to the sample.

The ionophores studied in this work were the following: the proton ionophore carbonyl cyanide 3-chlorophenylhydrazone (CCCP), the naturally produced

protonophore indole, the pore-forming polymyxin B nonapeptide hydrochloride (PBNP), the potassium ionophore valinomycin, and the proton/potassium antiporter nigericin. All the compounds were dissolved in ethanol. The final ethanol concentration in the sample was kept below 1 % (10 g/L). The results showed that, as expected, CCCP caused effective membrane depolarisation, while nigericin and valinomycin had a mild impact on membrane potential. Interestingly, PMBN at concentrations below 50  $\mu\text{M}$  caused membrane depolarization, but above 50  $\mu\text{M}$ , this compound led to membrane hyperpolarisation. Finally, I found the surprising effect of indole causing a transient membrane hyperpolarisation, which conflicts with previous reports. I will deal with this issue in detail in Chapter 6. The final concentration of each ionophore used throughout the rest of this work can be found in Table 5<sup>330</sup>.

### 3.8.2 CCCP and valinomycin modulate permeability

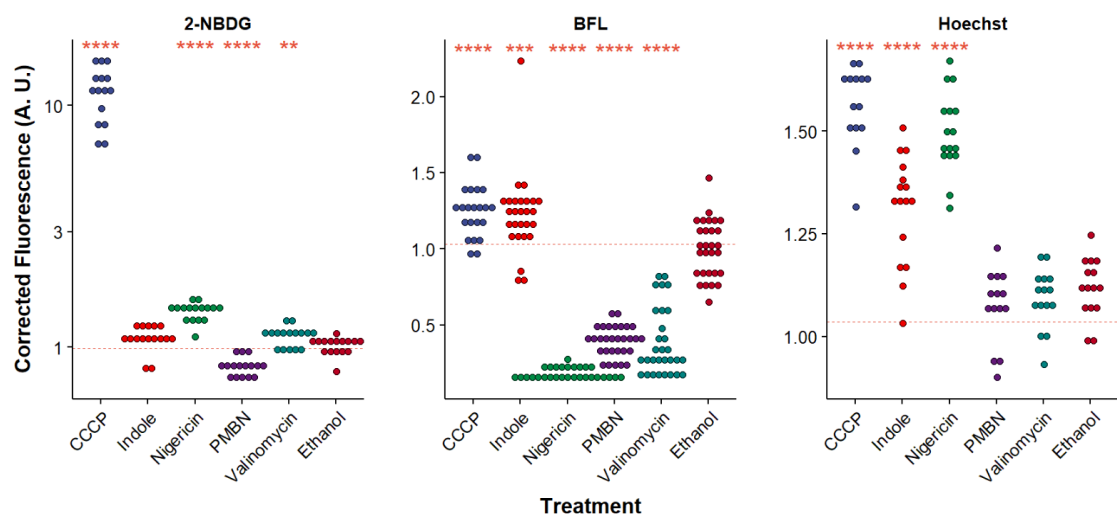
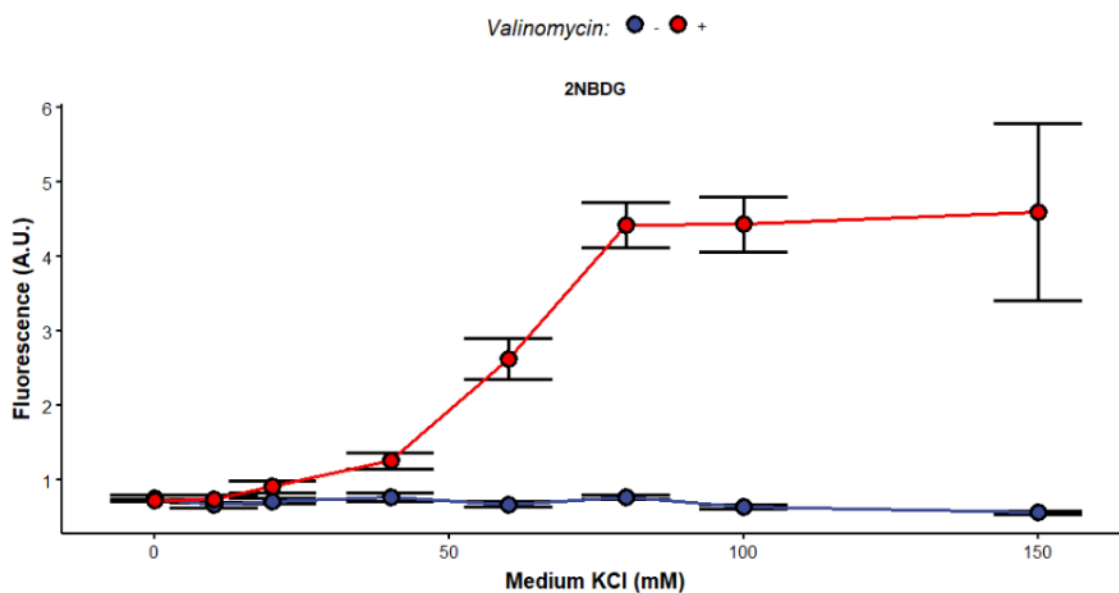


Figure 3.6: Ionophores modulate tracer uptake.

Fluorescence tracer uptake after 15 min by *E. coli* mutants growing in supplemented M9 (section 2.2.2). Each dot represents a biological replicate. The red dotted line indicates the control average. The statistical significance was evaluated with a t-test using the WT strain as the reference group. Here, one star denotes p-val. < 0.05, two stars p-val. < 0.01, three stars p-val. < 0.001, and four stars p-val. < 0.0001. Corrected fluorescence was calculated by dividing the fluorescent signal by the FSC signal to compensate by the cell size, and then I subtracted the background fluorescence (cells signal without tracer).

To measure the impact on membrane permeability, I added a pre-treatment step to my protocol. Consequently, before adding the fluorescent tracer, I treated cells for 30 min with the ionophore or the vehicle alone. A summary of the effect of each ionophore on the membrane permeability is shown in **Figure 3.6**. This experiment showed that the treatment with PMBP, nigericin or valinomycin had a very significant effect on BFL uptake. Surprisingly, valinomycin and nigericin had opposite effects on Hoechst and 2NBDG permeability. In addition, I also found that the proton ionophore CCCP increased the uptake of BFL, Hoechst, and, most drastically, 2NBDG. Therefore, I undertook subsequent analysis mainly using 2NBDG.

### 3.9 High internal potassium increases porin permeability



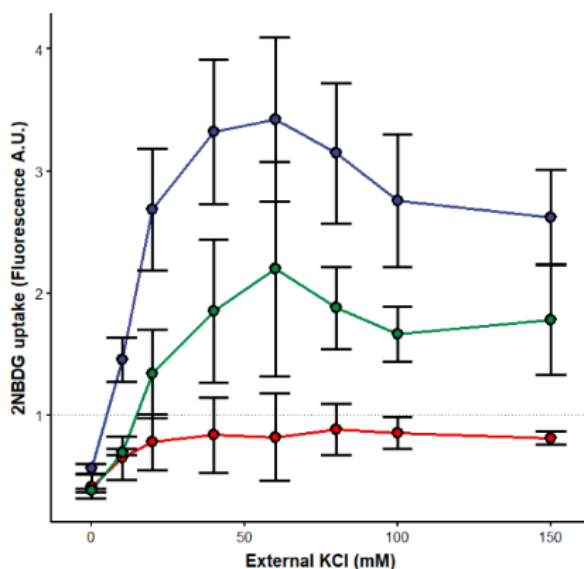
**Figure 3.7: Permeability of valinomycin treated cells depends on potassium concentration.**

Diagram showing the uptake of 2NBDG by *E. coli* after a treatment to modulate their internal potassium concentration. The dots represent the average across replicates, and Error bars denote the standard error. In red, I have the valinomycin treated cells (30 min incubation with 100  $\mu$ M valinomycin), and in blue, the untreated cells. All experiments were carried out in 96-well plates.

Given the remarkably effect of valinomycin on the permeability of 2NBDG, I went on to perform a more detailed study on the effect of potassium on cell permeability. Thus, I compared the uptake of 2NBDG in valinomycin treated cells

at a wide range of external potassium concentrations. Previous studies showed that high salt concentration (>100 mM of any monovalent cations) could significantly affect bacterial permeability<sup>102</sup>. Hence, I used an osmotically neutral medium based on HEPES buffer with NaCl and KCl as counter ions. Thus, the total cation concentration was kept constant at 150 mM for all conditions. This experiment made clear that high internal concentrations of potassium increased 2NDBG permeability (see Figure 3.7).

Subsequently, I replicated the same experiment on KO strains' the main porins: OmpC and OmpF. Surprisingly, this work showed that  $\Delta ompC$  did not show permeability changes with changes in external potassium. The  $\Delta ompF$  strain, however, had a similar increase in permeability with increases in potassium to WT, albeit with generally lower uptake (see Figure 3.8).



**Figure 3.8: The porin OmpC mediates the potassium effect on permeability.**

Uptake of 2NBDG by different *E. coli* strains after a treatment to modulate their internal potassium concentration. The dots represent the average across biological replicates, and error bars denote the standard error. In blue, I have the WT strain against the  $\Delta ompF$  (green) and  $\Delta ompC$  (red). Cells were treated with 100  $\mu$ M valinomycin for 30 min with the indicated KCl concentration. I then harvest the cells as described in 3.1. All experiments were carried out in 96-well plates.

### 3.10 The decrease in internal pH reduces permeability

To further understand the effect of pH on membrane permeability, I exposed bacterial cells to a wide range of pH in the presence or absence of CCCP. Here, CCCP clamped the internal proton concentration with the medium. The data

indicate that 2NBDG permeability changes only in the presence of CCCP (see **Figure 3.9**). This evidence suggests that the internal pH controls the membrane permeability rather than the pH medium.

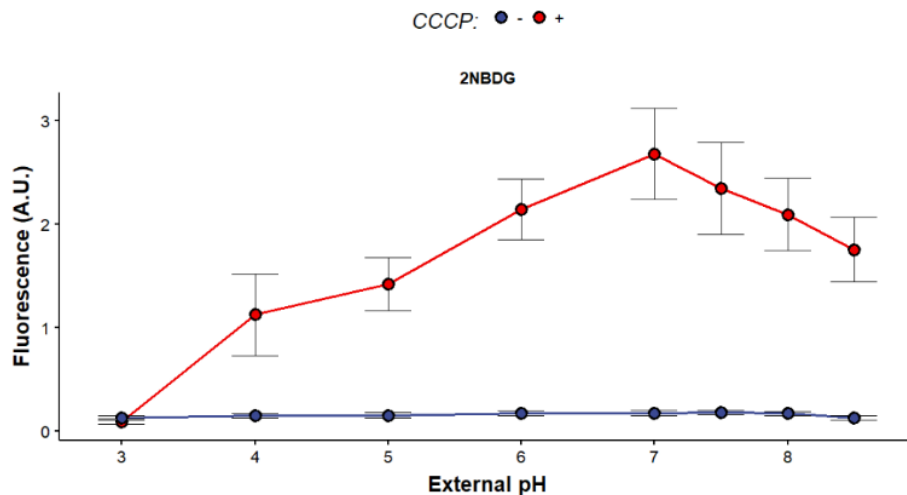


**Figure 3.9: Permeability of CCCP treated cells correlates with pH.**

Diagram showing how the modulation of the cellular pH drives the uptake of 2NBDG in *E. coli*. The dots represent the average across biological replicates, and error bars denote the standard error of the three replicates. CCCP treated cells are represented with red dots (30 min incubation with 250  $\mu$ M CCCP) and in blue, the untreated cells. All experiments were carried out in 96-well plates.

To examine this effect in more detail, I repeated this experiment on the porin KO strains  $\Delta ompF$  and  $\Delta ompC$ . This experiment revealed the individual contribution of each porin (see **Figure 3.10**). Here, I found that the uptake of 2NBDG is reduced in  $\Delta ompF$  and strongly impaired in the  $\Delta ompC$  strain. Still, the pH effect was present for all three strains.

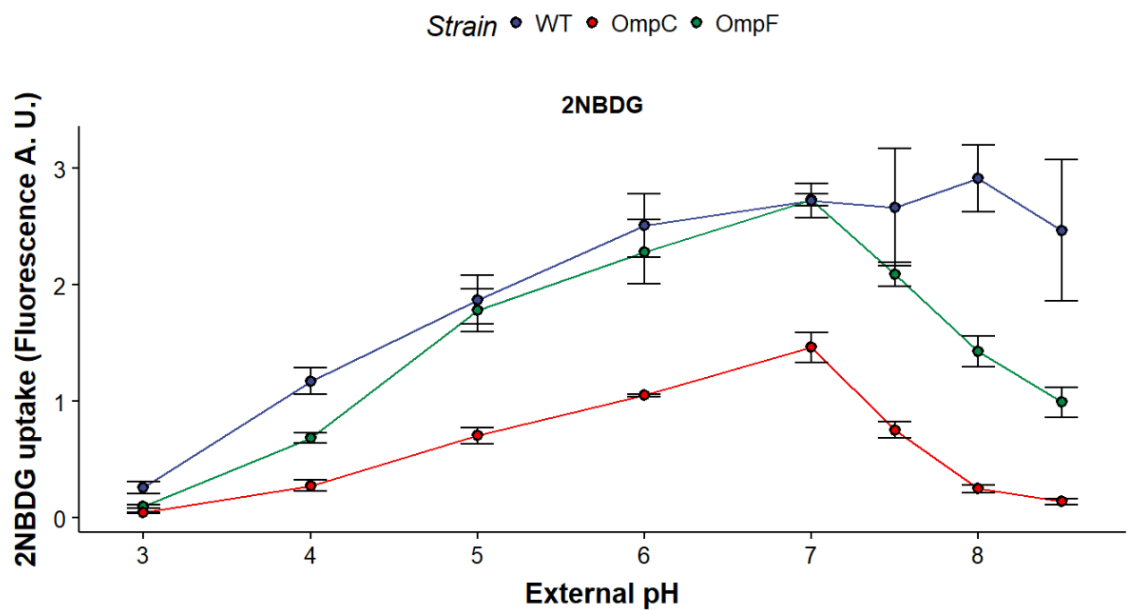


Figure 3.10: The pH permeability effect of CCCP treated cells depends on bacterial porins.

Uptake of 2NBDG by different *E. coli* strains after a treatment to modulate their internal pH. The dots represent the average across biological replicates, and error bars denote the standard error of the three replicates. In blue, I have the WT strain against the  $\Delta$ ompF (green) and  $\Delta$ ompC (red). Cells were treated with 250  $\mu$ M CCCP for 30 min at the indicated pH. I then harvest the cells as described in 3.1. All experiments were carried out in 96-well plates. For all the strains, the data shows that a decrease in pH leads to a decrease in 2NBDG uptake.

### 3.11 ArchT activation increases cytoplasmic pH

In view of the apparent correlation between internal pH and 2NBDG permeability, I extended the study to examine whether modulation of permeability was due to changes in periplasmic pH. I, therefore, assembled a light-activated proton pump (ArchT) in a plasmid for bacterial expression (section 3.3). ArchT is an archaerhodopsin derived from *Halorubrum* strain TP009<sup>387</sup>. This protein responds to yellow light by transporting protons across the membrane. For this function, it requires a retinal co-factor. Although ArchT has been successfully expressed in bacteria, it is mainly expressed in neural cell lines<sup>368,379,387</sup>. Thus to evaluate the ArchT efficiency of Arch depolarisation in *E. coli*, I expressed ArchT in conjunction with the pH sensor pHluorin. This protein is a GFP derived fluorescent protein whose fluorescence intensity is proportional to the pH of the cytoplasm<sup>329,365</sup>. Using a TIRF microscope (see section 3.5), I compared the pHluorin fluorescence

of cells with or without 561 nm laser illumination, which activates the ArchT pump. Therefore, I saw that the cytoplasmic pH of the cells expressing ArchT increased when exposed to the 561 nm light source (Figure 3.11), indicating that ArchT was pumping protons to the periplasm. This result indicated that the expression of the ArchT system could be used to pump protons to the bacterial periplasm *in vivo*.

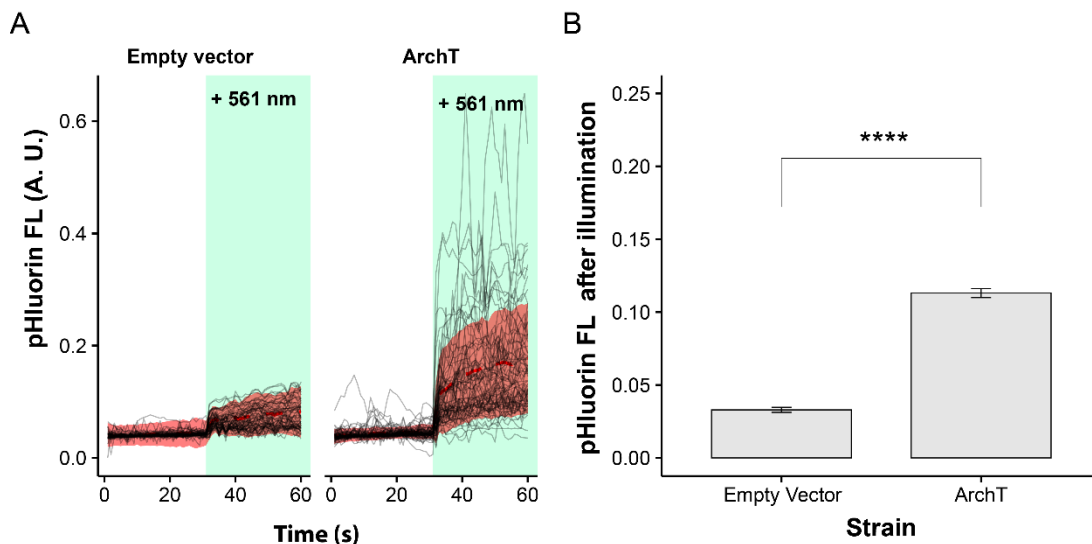


Figure 3.11: Illumination with 561 nm light leads to a decrease in cytoplasmic pH of cell expression ArchT.

A) Trace plot of the pHluorin tracer in *E. coli*. The Y-axis indicates the relative pHluorin fluorescence. The trace of each cell is represented in grey. The red dashed line represents the average of all cells, while the red shaded area represents the standard deviation in red. The green rectangle indicates when the 561 nm excitation light was activated. B) Average fluorescence of pHluorin cells expressing ArchT vs empty vector with or without light exposure. The error bar represents the standard error. The statistical significance was assessed with a t-test, p-value < 0.001.

### 3.12 ArchT activation decreases 2NBDG uptake

Next, I measured the impact of ArchT activation on 2NBDG uptake. For this purpose, I grew *E. coli* cells expressing ArchT and trapped them into the Mother Machine. I then transferred the device to the microscope and washed the cells with M9 for 30 min. At this point, I added the 2NBDG to the medium and compared the uptake. The result demonstrated that ArchT cells uptake 2NBDG at a similar rate to the empty vector strain (Figure 3.12A). However, when I activated the

ArchT pump with the 561 nm light source, I noticed a considerable decrease in 2NBDG uptake, not seen in the empty vector control (Figure 3.12C).

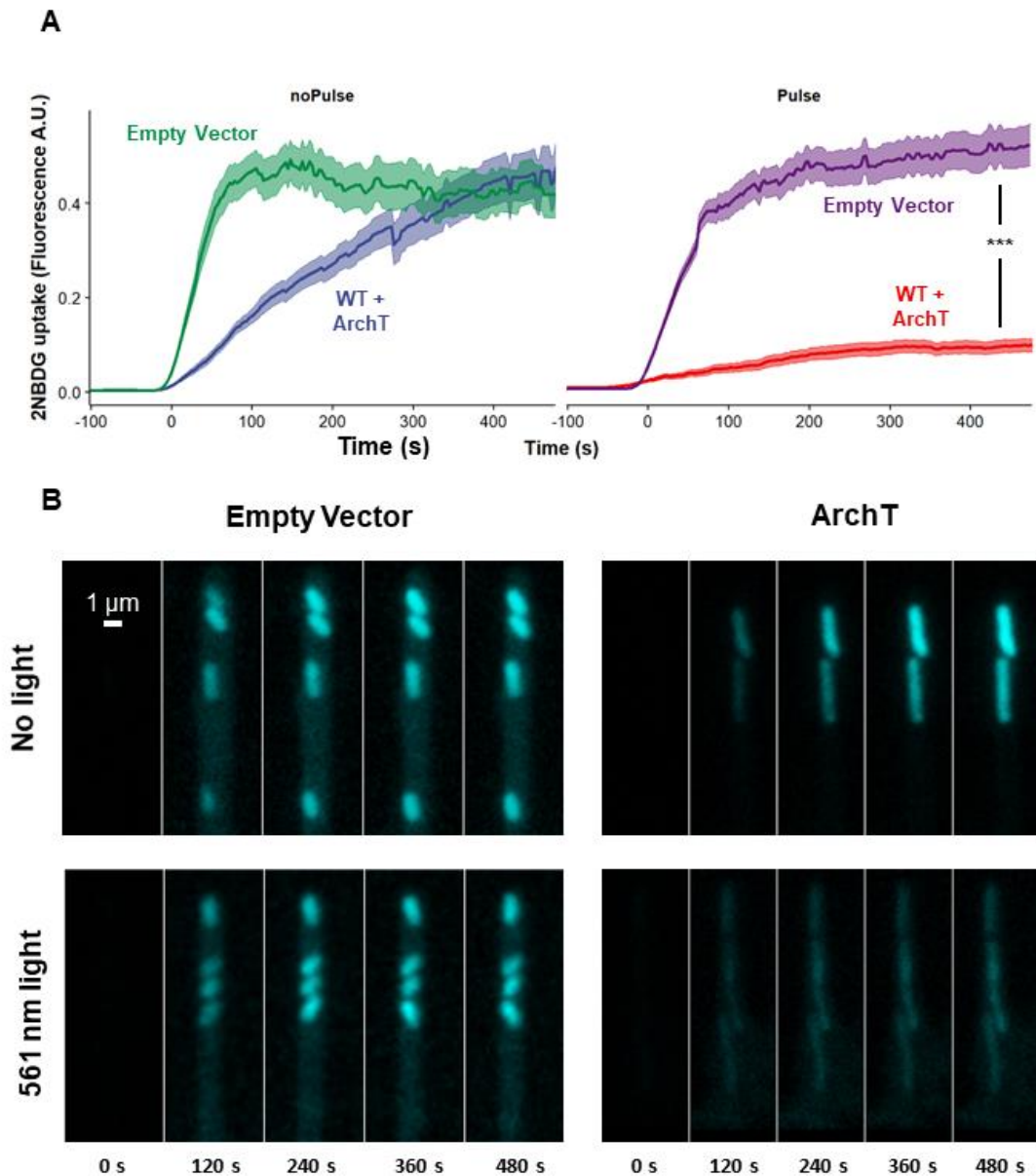
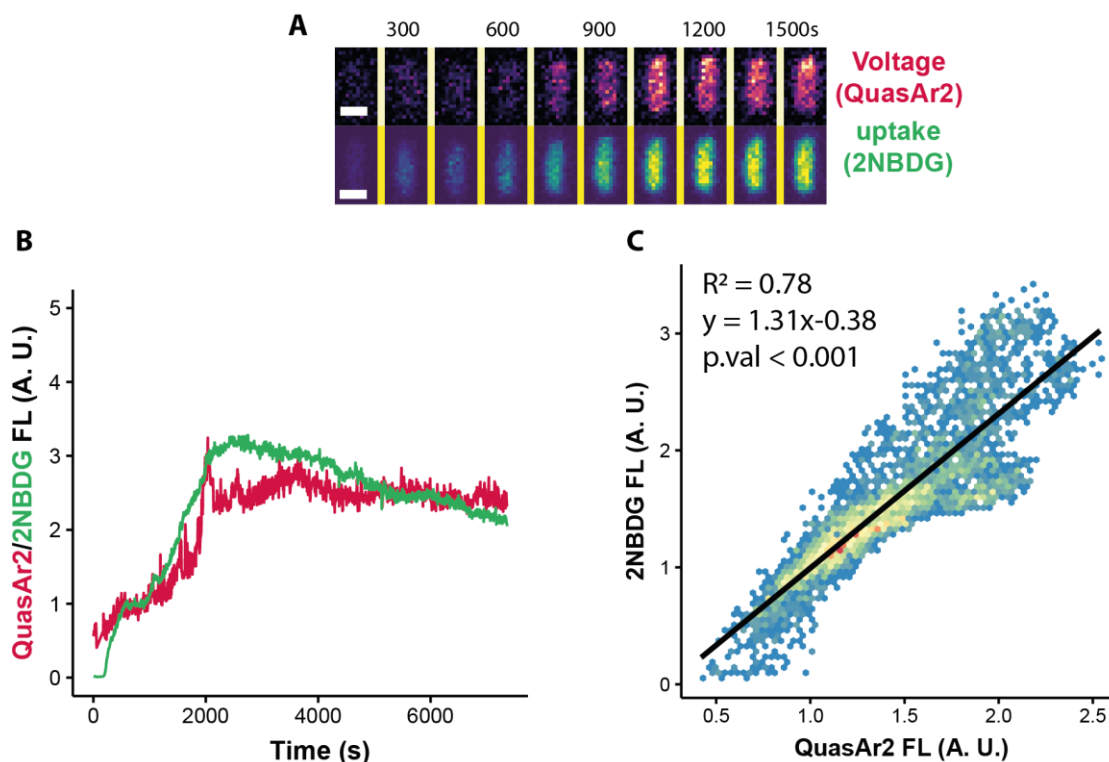


Figure 3.12: Light activation of ArchT leads to a decrease in 2NBDG uptake.

A) 2NBDG signal in single cells. The dark coloured line represents the population average with the shaded area as the standard error. I represented in the left panel in green the WT cells and in blue the ArchT cells both without 561 nm illumination; in the right panel, I have in purple the WT cells and in red the ArchT cells under 561 nm illumination. For the statistical comparison of the uptake rate between empty vector and ArchT expressing cells, I compared each sample with the empty vector as a reference (t-test,  $p$ .val < 0.001). B) Representative images of cells for all conditions.

### 3.13 2NBDG uptake correlates with membrane depolarisation

Given the effect of ArchT activation on bacterial permeability, I investigated whether the bacterial membrane potential changes might correlate with nutrient uptake. For that purpose, I monitored the uptake of 2NBDG on *E. coli* cells in the Mother Machine expressing the voltage sensor QuasAr2. This reporter was a kind donation of Adam Cohen's lab<sup>366</sup>. The fluorescence of this sensor increases with membrane depolarisation. The experimental results are summarized in **Figure 3.13A** and **B**, where it is clear that the arrival of 2NBDG to the cells is accompanied by general depolarization of the bacterial population. In addition, **Figure 3.13C** shows how 2NBDG fluorescence in the cells is correlated with Quasar2 fluorescence.



**Figure 3.13: Uptake of 2NBDG correlates with an increase in Q2 fluorescence.**

Bacteria were grown overnight in SOB + 20  $\mu$ M retinal, 0.002 g/L arabinose and ampicillin. Note that as in ArchT, QuasAr2 is a proteorhodopsin, so it requires retinal to work. The next day, cells were washed with M9 and concentrated 2 mL in 100  $\mu$ L. Then, I injected the cells into a microfluidic chip. I allowed 10-15 min to allow the cells to enter the side channels and flushed the chip with M9 at 1 mL/h flow rate. Finally, before adding 20  $\mu$ g/mL 2NBDG, I washed the chip for 30 min with M9 **A**) Representative images of QuasAr2 fluorescence and 2NBDG fluorescence. The

white scale bar represents a 1  $\mu\text{m}$  distance. **B)** Fluorescence trace of a representative cell, QuasAr2 fluorescence (red), and 2NBDG fluorescence (green). **C)** Linear regression plot of QuasAr2 fluorescence and 2NBDG fluorescence. The coloured heatmap represents a density plot of all the sample points of the whole population. The black line stands for the simple linear regression of the two fluorophores. The  $R^2$  of the model is 0.78, and the value of the  $\beta$  estimate is 1.35 (p-val. < 0.001).

### 3.14 Porin protonated periplasmic residues lead to pore contraction

Further structural analysis was done to determine the molecular mechanism behind the change in porin permeability with the pH. In collaboration with Ali Alsulami (Professor Sir Tom Blundell's Lab, Department of Biochemistry), we ran a molecular dynamic simulation of the two main *E. coli* porins (OmpF and OmpC) and neutral and low periplasmic pH. The low internal pH effect was simulated by protonating several residues from the periplasmic side (see methods section 3.6). The final model suggested a general reduction in the diameter (Figure 3.14). Interestingly, the OmpC pore had a more significant contraction (2.5  $\text{\AA}$  to 1.7  $\text{\AA}$ ) than OmpF (1.8  $\text{\AA}$  to 1.4  $\text{\AA}$ ).

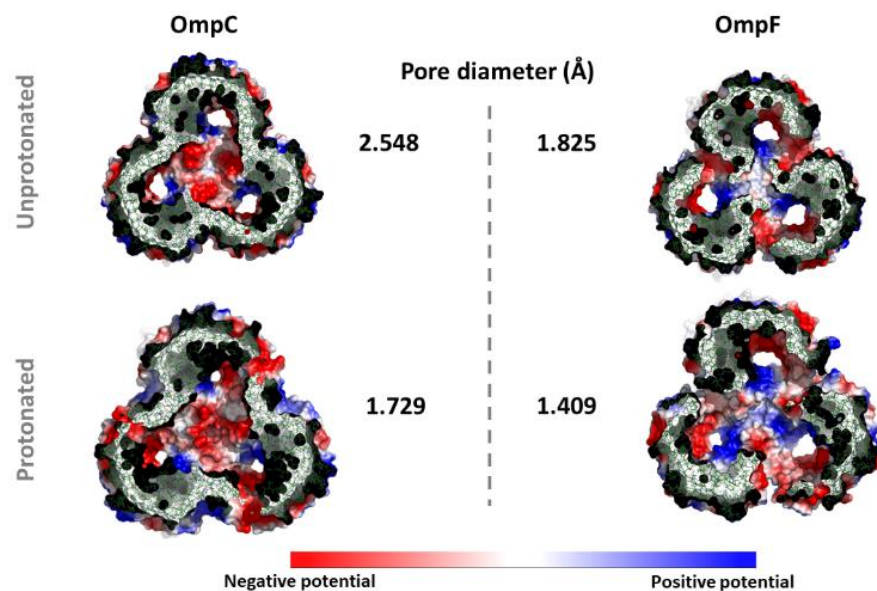


**Figure 3.14** Protonation of the periplasmic residues compresses the pore diameter of OmpC and OmpF.

Analysis was done at constant pressure (1 atm) and temperature (300 K, 26  $^{\circ}\text{C}$ ). All images are the views from the inside (periplasmic side). The cut-through section of the porin was done at the

midpoint of the pore. Electrostatic potential was visualised with blue (positive potential) to red (negative potential).

## **Discussion**

This study has demonstrated that intracellular protons and potassium modulate bacterial membrane permeability.

### **3.15 Membrane permeability estimation**

Firstly, I have shown that fluorescent markers combined with flow cytometry represent an optimal method to estimate bacterial permeability. This technique could discriminate between the WT strain and the main porin KO (OmpF and OmpC), known to affect permeability<sup>26</sup>, which validated our approach. It also allowed us to screen the effect of several ionophores on membrane permeability. In accordance with previous studies<sup>84,85,93,102</sup>, I found that ions, mainly protons and potassium, modulated permeability. One possible explanation for this result could be an interaction between the dye and the ionophore, but the CCCP treatment produced consistent results in three different markers (2NBDG, Hoechst and BFL), while valinomycin produced similar results in two of the markers (2NBDG and BFL).

### **3.16 Potassium increases permeability**

I found that the modulation of external  $K^+$  concentration only affected porin permeability in the presence of valinomycin, implying that the internal levels of  $K^+$  were driving the permeability change. It could be argued that the increase in permeability was due to an increase in cations as reported by Kojima<sup>102</sup>, but I accounted for that effect using an osmotically neutral buffer. In addition, when I applied this method to the porin KO (OmpF and OmpC), I noticed that the 2NBDG permeability of the  $\Delta ompC$  strain was less susceptible to KCl than the WT strain and the  $\Delta ompF$  strain (see Figure 3.8). Together, these findings are strongly suggestive of a potassium interaction with the OmpC residues. Interestingly, Kojima reported significant changes in the electrostatic surface of OmpC with the

addition of monovalent cations<sup>102</sup>. However, as will be shown in section 4.5.3, valinomycin treatment does not have a strong influence on the cytoplasmic K<sup>+</sup>. This observation further supports the idea of periplasmic K<sup>+</sup> as a driver of porin permeability.

### **3.17 Proton decreases of permeability**

Due to its interesting effects, I conducted a comprehensive analysis on the impact of CCCP and protons on 2NBDG uptake. Initially, I showed that CCCP treated cells quickly respond to the changes in the pH, yet control cells were less susceptible. Next, I asked whether the source of this effect was related to porins. Thus, I replicate the same conditions with the major porin KO:  $\Delta ompF$  and  $\Delta ompC$  strains. Whilst both mutants presented a decrease in uptake, the permeability of all strains decreased significantly with the decrease of the medium pH (see Figure 3.10).

Furthermore, the expression of ArchT in *E. coli* provides a valuable tool to manipulate the cellular pH at the single-cell level. The combined expression of pHluorin and ArchT shows that the system is very responsive and tightly controlled. Growing *E. coli* cells expressing ArchT demonstrated that permeability was affected only with the 561 nm light activation. This observation represents strong evidence that the periplasmic pH affects bacterial porin permeability. However, an alternative explanation could be that ArchT influences the inner membrane transport of 2NBDG or stimulates its efflux. The enhanced efflux of 2NBDG could result from the hyperpolarised membrane, which stimulates the function of antiporters as described in the introduction (section 1.4.4.6). Nevertheless, this phenomenon would appear unlikely because no known proteins mediate glucose efflux in *E. coli*.

Moreover, the increased hyperpolarisation of the inner membrane should not affect the uptake of 2NBDG because, like glucose, this molecule is taken up via the PTS system, which works independently of the proton gradient (see section

1.4.2.1). The use of the PTS is evident from the decreased uptake of 2NBDG when both are available due to competition<sup>388</sup>. Nevertheless, experimental corroboration that ArchT disrupts porin permeability could be achieved by measuring uptake of additional tracers, such as BFL or Hoechst.

### **3.18 Membrane depolarisation correlates with 2NBDG uptake**

The results of the ArchT activation experiments implied that a hyperpolarised membrane decreased the cell permeability. Therefore, I set to test this deduction by measuring the uptake of 2NBDG while monitoring the membrane potential. To monitor the membrane potential, I used QuasAr2, whose fluorescence increases when the membrane potential decreases. This reporter pointed to a decrease in membrane potential with the uptake of 2NBDG. Two models could explain this correlation: Either 2NBDG uptake to the cytoplasm consumes the proton gradient, and with it, the membrane potential, or the membrane hyperpolarisation blocks uptake at the level of porins. Similar to the previous suggestion, this issue could be solved by monitoring the uptake of BFL and QuasAr2 simultaneously.

### **3.19 Porin pore diameter narrows with protonation**

The molecular dynamic simulation revealed that the periplasmic residues' protonation triggers a conformational change that closed the pore size. Despite the fact that our simulation suggested a reduction in pore diameter with protonation in OmpF and OmpF porin, the OmpC porin presented a greater diameter reduction. Nevertheless, our results presented two major limitations. First, the periplasmic residues were explicitly protonated in a pre-defined manner. Fixing this parameter means the model could have a protonation state that does not occur *in vivo*. A more realistic approach could be performing a constant-pH

replica-exchange where the simulation samples through the protonation state of each residue at different pHs. Although this method has been implemented for globular proteins<sup>389–391</sup>, our goal was to simulate a different pH across the membrane, which presents further complexity<sup>392</sup>. The second issue was that our simulation had a constant K<sup>+</sup> concentration. That means the simulation model could not explore the potassium-permeability interaction described in the experiments. Given our current findings, a complete model could be considered. A hypothetical complete model should include the effect of potassium as well as the interaction of surrounding lipids with their protonation state.

### **3.20 Conclusion**

In conclusion, this study has presented a strong case for the regulation of porin permeability by ions in living bacteria. In particular, the results indicated that changes in the internal concentration of protons and potassium ions modulate bacterial permeability. Moreover, the OmpC porin seems to respond strongly to changes in potassium. Furthermore, with the help of the optogenetic proton pump ArchT, I demonstrated that increasing the periplasmic pH is enough to collapse cell permeability. This finding provides valuable insights into the mechanism of porins. In addition, we present a computational model to explain the molecular mechanism responsible for this phenomenon. Previous works have studied the impact of site-directed mutations on the L3-loop<sup>393,394</sup>, but the effect of changes in the periplasmic residues remains poorly understood. The role of the periplasmic gate in permeability has mainly been studied through computer simulations<sup>91</sup>. Moreover, our MDS data is consistent with the broader literature, but the ultimate verification should come with empirical evidence. I intend to provide this information using porins reconstituted in lipid vesicles with a defined pH inside and out.

# **Chapter 4: TRANS- MEMBRANE ION OSCILLATIONS**

## Summary

The previous chapter provided a wealth of evidence suggesting that changes in periplasmic pH and potassium modulate porin permeability in *E. coli*. However, it is not clear whether changes in these ions could, therefore, act as dynamic regulators of porins *in vivo*. This section aims to explore the presence of ion oscillations in live bacteria. For this purpose, I deploy a comprehensive set of genetically encoded ion and voltage sensors to understand the cellular regulation of ion homeostasis. When combined with the Mother Machine, these tools allowed me to study cellular electrophysiology at the single-cell level.

My results suggest that growing cells show fluctuations of  $K^+$  and periplasmic pH. In turn, the movement of these ions generates membrane potential spikes. Next, I investigate the underlying mechanism of these ionic fluctuations. First, I found that the addition of glucose increased the ion movement, which did not occur when cells were supplied with no carbon source or lipid base medium. Second, I found an increase in membrane potential spikes with the increase of carbon source concentration.

Finally, I investigated the role of the voltage-activated potassium channel Kch on the membrane potential spikes. The final analysis indicates that this channel determines the resting membrane potential of cells and indirectly affects the periplasmic pH.

*I have performed all the experiments and analyses described in this chapter except the measurement of Hoechst permeability, which was performed by Dr Anja Hagting (Floto lab).*

## Introduction

In liquid culture experiments, extracellular conditions are well mixed, and cell measurements are averaged out. These approaches hide the dynamics of single-cell heterogeneity<sup>362</sup> (see section 1.6). This issue is highly relevant for experiments examining cellular electrophysiology because recent studies have shown that bacterial membrane potential shows transient depolarisation spikes<sup>323</sup>.

The possibility that these transient depolarisations respond to cellular processes is supported by studies showing oscillations in the cytosolic pH<sup>395</sup> and the metabolic cycle of yeast<sup>320</sup>. Both reports showed that cells supplied with different carbon sources present a phase shift in the oscillatory behaviour<sup>320</sup>. In addition, a study done on *Bacillus subtilis* demonstrated that cells growing in biofilms coordinate their behaviour following an alternating metabolic state between different regions<sup>214</sup>. However, a comprehensive analysis covering all the components of bacterial electrophysiology is still lacking.

This project aims to investigate the electrophysiological regulation of *E. coli* at the single-cell level. For that purpose, I leveraged the Mother Machine in combination with a broad set of genetically encoded ion sensors. In total, I deployed sensors to measure cytoplasmic pH (pHluorin), cytoplasmic potassium (GINKO1), cytoplasmic calcium (GCaM), and the membrane potential (QuasAr2)<sup>324,329,366,367</sup>. In addition, I also developed a custom sensor to measure bacterial pH in the periplasmic region (pelBC::pHuji)<sup>369</sup>.

Overall, I observe an independent regulation of periplasmic pH, suggesting periplasmic isolation from the medium. Moreover, in line with the research in other organisms<sup>320,395</sup>, these findings suggest that carbon metabolism controls bacterial electrophysiology. Finally, I combine these observations with our

previous findings to propose a comprehensive model incorporating bacterial electrophysiology and membrane permeability.

## Material and methods

### 4.1.1 Ion sensor calibration

Cell trapping was done following the protocol described in section 2.5.3. After trapping the cells, they were resuscitated with M9 + 1 g/L glucose + 1 g/L casamino acids + 1 mM tryptophan for 90 minutes. Then, for the pH calibration, I switched the medium to M9 + 1 g/L glucose for 30 min and finally to PBS calibrated to a determinate pH with 1 g/L glucose. The pH selected points were 8.5, 7.4, 6.5 and 5.5. The same procedure was done by adding 250  $\mu$ M CCCP to the medium to permeabilise the cells. In the case of the potassium calibration, I used a medium HEPES pH 7.4 with complementary concentrations of KCl and NaCl to keep the osmolarity constant at 150 mM. In order to permeabilise cells to the extracellular potassium, I treated cells with 100  $\mu$ M valinomycin. The flowing conditions were kept at 0.15 mL/h, and during the switch, I increased the speed to 1 mL/h for 15 min. Table 8 summarises the illumination setup of each fluorophore.

**Table 8: Illumination conditions of each fluorescent sensor**

Name	Excitation (nm)	Emission (nm)
pelBCpHuji	561	620/60
pHluorin	488	525/50
GINKO1	488	525/50
GCaM	488	525/50
QuasAr2	561	650/LP

### 4.1.2 Ion oscillations

To observe the ion oscillations, I resuscitated cells with M9 + 1 g/L glucose + 1 g/L casamino acids + 1 mM tryptophan. The flow and temperature were kept constant at 0.150 mL/h and 37C. After 90 minutes, I started the recording process, which lasted until cells started dividing. Finally, I only considered the 45 minutes before starting cell division for the data analysis.

### **4.1.3 Carbon source switching**

After trapping the cells into the chip, cells were washed with a plain M9 medium. Once the main channel was clear, the flow was kept constant at 0.15 mL/h for 30 minutes. At this point, I changed the syringe to the required carbon source and increased the flow to 1 mL/h. After flowing the medium for 2 minutes, I started the recording.

### **4.2 Agar pads**

Agar pads are equivalent to agar plates, but the agar is substituted by agarose due to its improved optical properties, and minimal medium is preferred to LB for the same reason (see section 1.6). These pads were prepared on the same day of the experiment and discarded afterwards. The gel was composed of a 10 mL M9 medium with 1.5 % (wt/vol) low-melting agarose. In addition, I supplemented this with the specified carbon source. I then proceed to dissolve the agarose by heating. Once the mixture was entirely homogeneous, the liquid was split into 3 mL portions onto a 35-mm petri dish. These plates were left to dry for 30 min. Once the agar solidified, I used a 6-mm biopsy puncher (Uni-Core, Harris UK) to cut out a single-use disk. On top of these agar disks, I dropped 1  $\mu$ L of cells. After the drop was absorbed, the pad was moved onto a CELLview™ Dish with Glass Bottom (627870, Greiner) and recording started immediately.

Cells were grown overnight in SOB medium supplemented with 20  $\mu$ M retinal and 0.002 g/L arabinose. The next day, cells were washed with M9 supplemented with the specified carbon source and 2  $\mu$ L were transferred to the agar pad. Before starting the recording, pads were left drying for 5 min.

### **4.3 Permeability analysis**

For the permeability estimation, a colony of *E. coli* was grown overnight at 37 °C in minimal medium M9, supplemented with casamino acids 1 g/L, tryptophan 1

mM and glucose 0.5 g/L. The next day, the source culture was diluted to an  $OD \sim 0.05$  in the same fresh medium. The total volume was 60 mL and placed in a 250 mL conical flask. When the cultures' turbidity reached an OD of 0.1-0.25, the culture was split into 2x15 mL (50 mL tubes). The cultures were spun down 5 min x3900 rpm (Eppendorf 5810R, rotor S-4-104), washed with M9 and resuspended in 15 mL fresh M9 + glucose (4 g/L high, or 0.04 g/L low) or plain M9 for starvation. Then, these cultures were transferred to a 37 °C water bath, and 400  $\mu$ L samples were taken at the indicated timepoints. Each sample was stained with Hoechst (10  $\mu$ g/mL), mixed and incubated for 10 min to allow uptake. Next, the samples were centrifuged for 30-sec max speed at 4 °C (Eppendorf centrifuge 5415 R), washed once and resuspended in 400  $\mu$ L ice-cold PBS. Finally, 2x 200  $\mu$ L was transferred to different wells of a V-bottom 96-well plate (Costar), the fluorescence from the samples was read using iCyt Eclipse (Sony). This device is equipped with 405 nm, 488 nm, 561 nm and 642 nm laser sources.

## Results

### 4.4 Cloning and expression of pelBCpHuji

The periplasmic pH sensor was based on the pBAD-TOPO vector (section 2.3.2). To this backbone, I added the *pelB* leader sequence. The *pelB* export signal sequence has proven to be successful for delivering recombinant proteins to the periplasm of *E. coli* and *Pseudomonas aeruginosa*<sup>370,396</sup>. This signalling sequence consists of 22 amino acids placed at the start codon (see Figure 4.1).

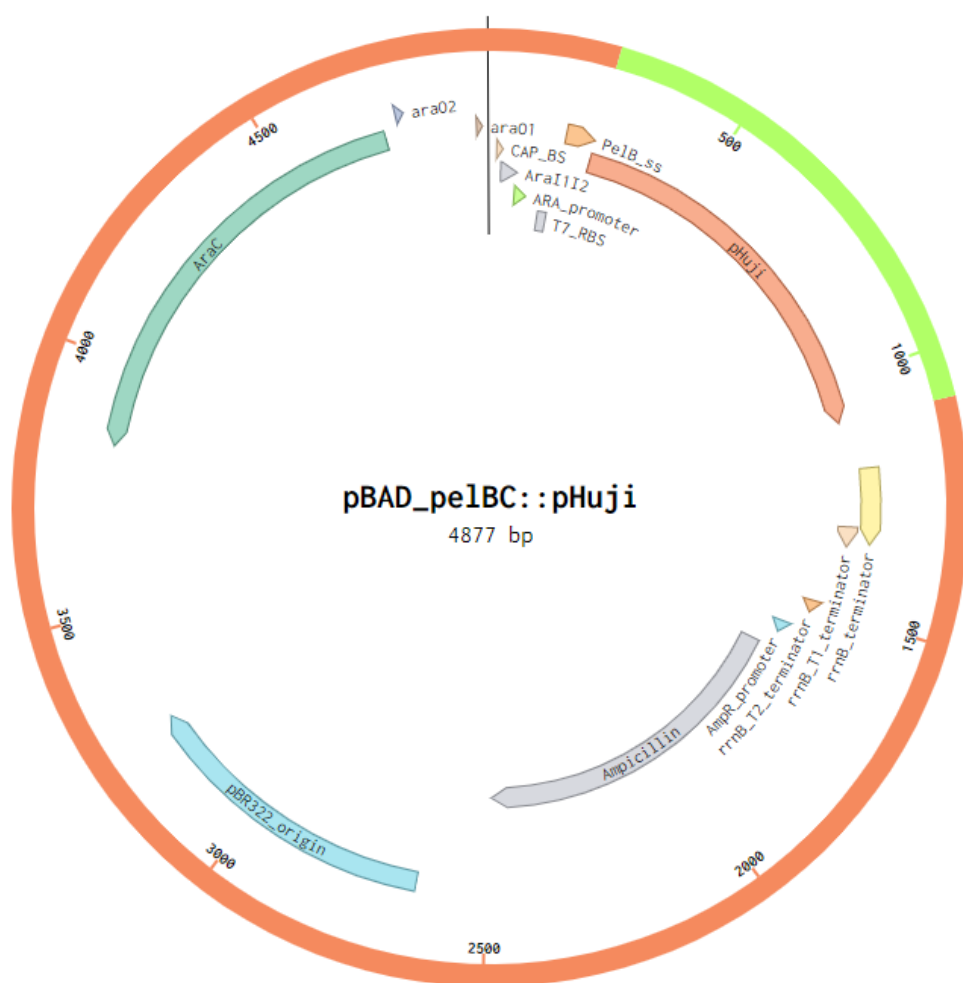


Figure 4.1 Expression vector pBAD-peIBC::pHuji.

The system's backbone is the same as described in section 3.3. Before the start codon of the pHuji sequence, I included the *pelB* leader sequence for export (labelled as *PeIB\_ss*). This system allows the export of the pHuji sensor to the periplasm.

Sequentially, I first designed a pBAD\_peIBC backbone, which I assembled with a Gibson assembly strategy (see section 2.3.1). Then, I inserted the pH sensor. In

order to measure the periplasmic pH accurately, I looked for a sensor with a wide dynamic range because the periplasmic pH could be up to 2 units lower than the cytoplasm, which means a pH 5<sup>397,398</sup>. Since pHluorin fluorescence collapses below pH 6, I opted for pHuji with a working range between 5 and 9<sup>369</sup>. During the assembly process, I used *E. coli* DH5 $\alpha$ , and after validating the sequence, I transferred the construct to an *E. coli* K12 BW25113 WT strain.

## 4.5 Ion sensors calibration

### 4.5.1 Periplasmic pH sensor validation

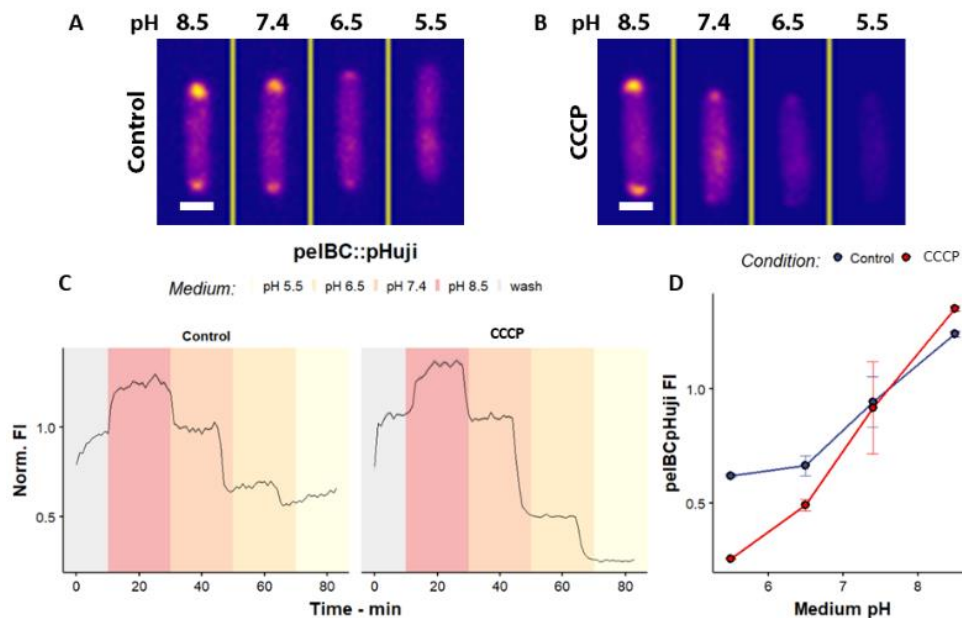


Figure 4.2: pelBC::pHuji sensor calibration

**A, B)** Sample images of *E. coli* expressing the periplasmic pH sensor pelBC pHuji. White scale bar equals 1 micron. The cells were trapped in the mother machine, and the flowing media was changed accordingly. Panel **A** show the pelBC::pHuji in cells exposed to PBS medium at different pH, while in panel **B**, the medium also contained CCCP, which permeabilizes the bacterial membrane to protons. Cells show accumulation of the periplasmic reporter in the poles. **C)** Normalized fluorescence of the pelBCpH signal in a bacterial population when exposed to different pH with and without CCCP. The shaded area corresponds with the standard error. **D)** Average fluorescence of the bacterial population plotted against the medium pH in the presence and absence of CCCP. In red, control cells and in blue CCCP treated cells.

To validate that the periplasmic sensor targeted the periplasm, I grew cells in M9 supplemented with 1 g/L glucose + 1 g/L casamino acids + 1 mM tryptophan. The

following day, I concentrated and transferred them to the Mother Machine. **Figure 4.2** (panels A and B) illustrates that the fluorophore signal was concentrated in the periplasmic region.

Next, I proceeded to assess pHuji pH sensitivity by changing the pH of the external medium in the presence or absence of CCCP. At this point, I switched the medium to M9 + 1 g/L glucose with decreasing pH, from 8.5 to 5.5 (see **Figure 4.2**, panels C and D). I found that treating cells with CCCP generated a linear response of pelBCpHuji fluorescence. Surprisingly, in the absence of CCCP, cells could buffer the periplasmic pH (see **Figure 4.2C**).

#### 4.5.2 pHluorin pH calibration

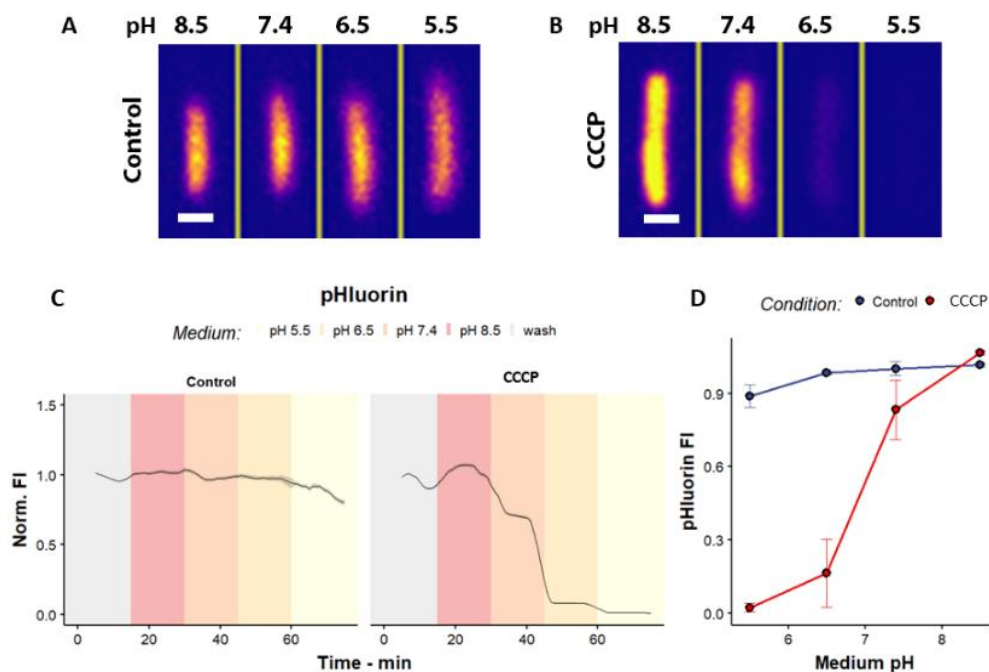


**Figure 4.3: pHluorin calibration**

**A, B)** Sample images of *E. coli* expressing the cytoplasmic pH sensor pHluorin. White scale bar equals 1 micron. The cells were trapped in the mother machine, and the flowing media was changed accordingly. **Panel A** show the pHluorin in cells exposed to PBS medium at different pH, while in **panel B**, the medium also contained CCCP, which permeabilizes the bacterial membrane to protons. Compared with the pelBC::pHuji, the pHuorin sensor accumulates over the cytoplasm. **C)** Normalized fluorescence of the pelBCpH signal in a bacterial population when exposed to different pH with and without CCCP. The shaded area corresponds with the standard error. **D)** Average fluorescence of the bacterial population plotted against the medium pH in the presence and absence of CCCP. In red, control cells and in blue CCCP treated cells.

For the cytoplasmic pH measurements, I used the pBAD\_pHluorin sensor<sup>329</sup>. This sensor was a kind gift from the Summers Lab (Department of Genetics). In order to calibrate this sensor, I followed the same approach as described in the previous section. Image analysis confirmed the proper expression of the sensor in the cytoplasm (Figure 4.3, panels A and B).

In addition, I found that CCCP treated cells exhibited a dynamic range between 6 and 8 pH (Figure 4.3, panels C and D). Finally, it is worth remarking that, in line with the previous literature<sup>399–401</sup>, the untreated cells exhibited a robust capacity to buffer the cytoplasmic pH (Figure 4.3).

#### 4.5.3 GINKO1 K<sup>+</sup> calibration

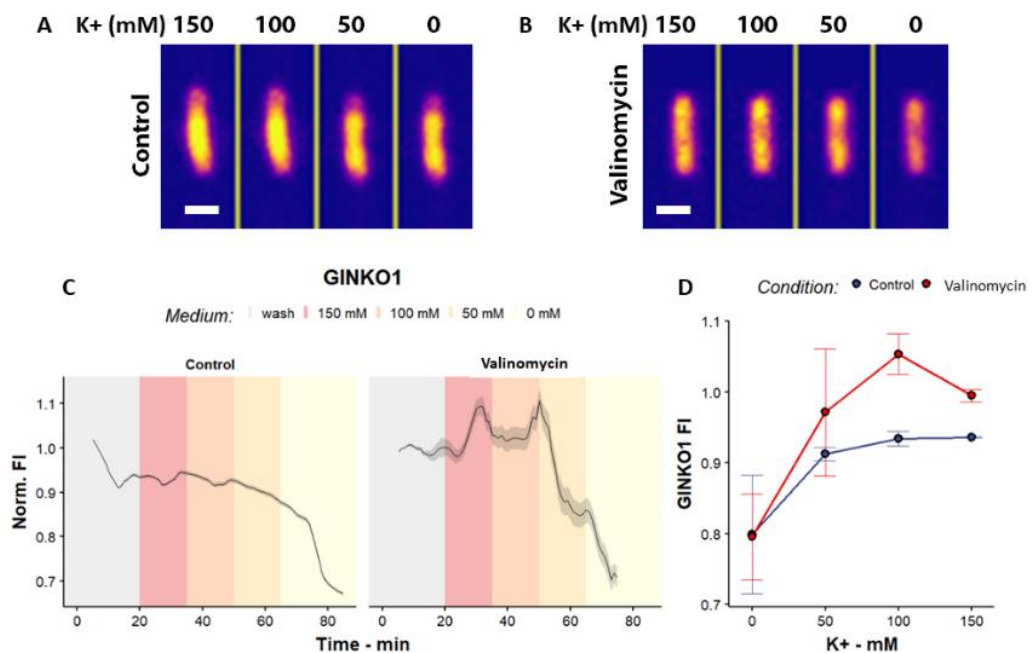


Figure 4.4: cytoplasmic GINKO1 calibration

Cells were supplied with M9 + 1 g/L glucose, and then we switched the medium to HEPES + KCl/NaCl with a constant osmolarity of 150 mM. **A, B)** Representative images of *E. coli* expressing GINKO1. White scale bar equals 1 micron. **C)** Average of the GINKO1 trace of the chip population. The shaded area corresponds with the standard error. **D)** Correlation between GINKO1 and concentration of potassium in the medium. In red, control cells and in blue valinomycin treated cells.

Cytoplasmic potassium was measured with GINKO1<sup>367</sup>. This plasmid was a kind donation of Dr Yi Shen (Campbell lab, University of Alberta). For the calibration, I adapted the method described in section 4.1.1, using Valinomycin instead of CCCP. Also, I changed the buffer from M9 to HEPES + KCl/NaCl, keeping the osmolarity constant at 150 mM (see section 4.1.1). Here, I discovered that the cytoplasmic potassium was tightly controlled (**Figure 4.4A**).

Strikingly, the images showed that the cytoplasmic environment was strongly protected from the valinomycin treatment (**Figure 4.4B**). Looking at the correlation between the signal and potassium concentration in the medium, I found that the total removal of the potassium decreased the GINKO1 signal regardless of the presence of valinomycin (see **Figure 4.4**, panels **C** and **D**).

## **4.6 Spontaneous ion oscillations**

After the calibration of the genetically encoded ion sensors, I looked for the presence of natural oscillations. For this purpose, I monitored the fluorescence of the ionic sensors in cells trapped in the Mother Machine. During this experiment, the cells were supplied with M9 + 1 g/L casamino acids + 1 g/L glucose + 1 mM tryptophan. After 90 minutes of resuscitation, I started recording the cell fluorescence. Image analysis revealed that the cytoplasmic calcium level remained relatively stable during the whole recording (**Figure 4.5A**). However, I observed strong oscillations in periplasmic pH and cytoplasmic K<sup>+</sup> (**Figure 4.5B**). Lastly, I found regular but small oscillations in cytoplasmic pH (**Figure 4.5B**). When comparing the volatility among the different ions, I could confirm that the periplasmic pH and cytoplasmic K<sup>+</sup> were the most dynamic (**Figure 4.5C**, p-value < 0.001, Mann-Witney-U test).

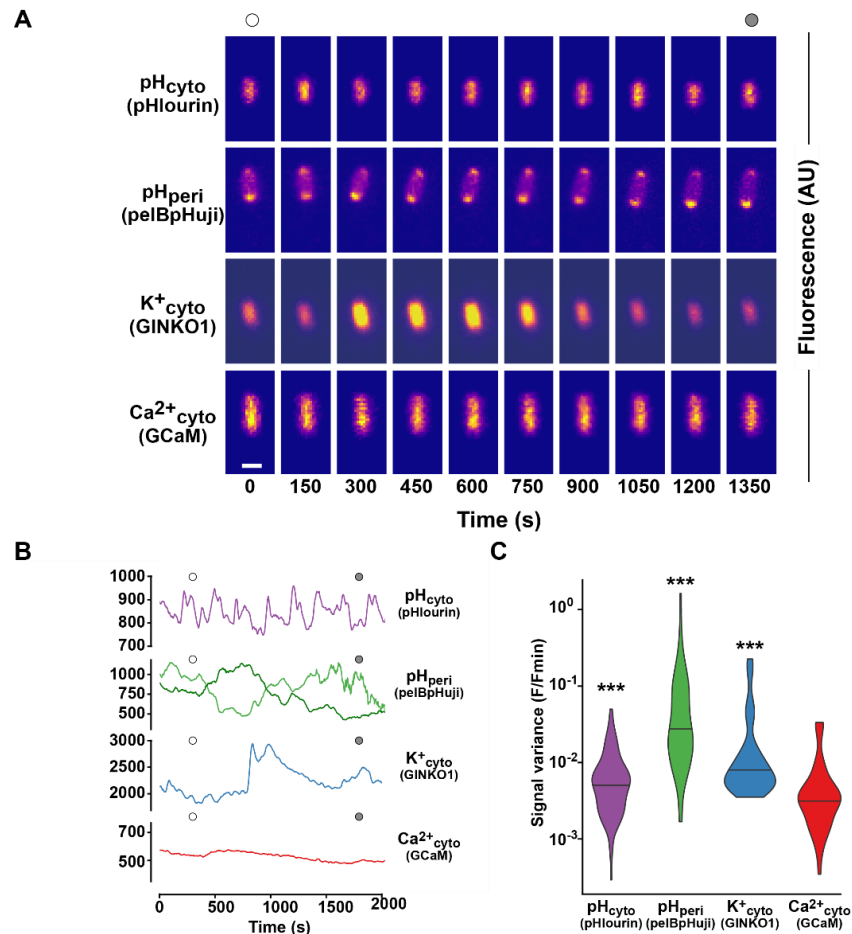


Figure 4.5: *In vivo* dynamics of physiological ions in *E. coli* are dominated by K<sup>+</sup> and periplasmic pH.

A) Representative images of the oscillations in the ion sensors. The absolute fluorescence is plotted in panel B. The white dot marks the beginning of the image montage, and the grey does the end. C) Density plot of the signal variance during a 15-min period of the recording. The statistical test compares the volatility of each sensor with the calcium signal due to its stability. Statistical comparison was made through a Mann-Witney-U test.

## 4.7 Carbon sources drive ion oscillations

Next, I proceed to investigate the factors affecting the oscillations. I hypothesized that the primary driver of the oscillations was carbon metabolism. Since potassium and protons are major components of the bacterial membrane potential, I also monitored the changes in the spiking frequency of the membrane potential reporter QuasAr2<sup>366</sup>. Thus, I monitored the cytoplasmic K<sup>+</sup>, the cytoplasmic and periplasmic pH, and the membrane potential of *E. coli* during the arrival of different carbon sources (see Figure 4.6). For this purpose, I grew the cells overnight

and resuscitated them the next day in the Mother Machine (see section 4.1.3). After 30 min wash with M9, I switched to different carbon sources. I found that (i) exposure to glucose resulted in oscillations in  $K^+$ , periplasmic and cytoplasmic pH, and membrane voltage; (ii) exposure to lipids resulted in very few ion fluctuations and a sustained hyperpolarisation of membrane voltage, while (iii) exposure to M9 media alone resulted in minimal impact on levels of ions or voltage. (Figure 4.6).

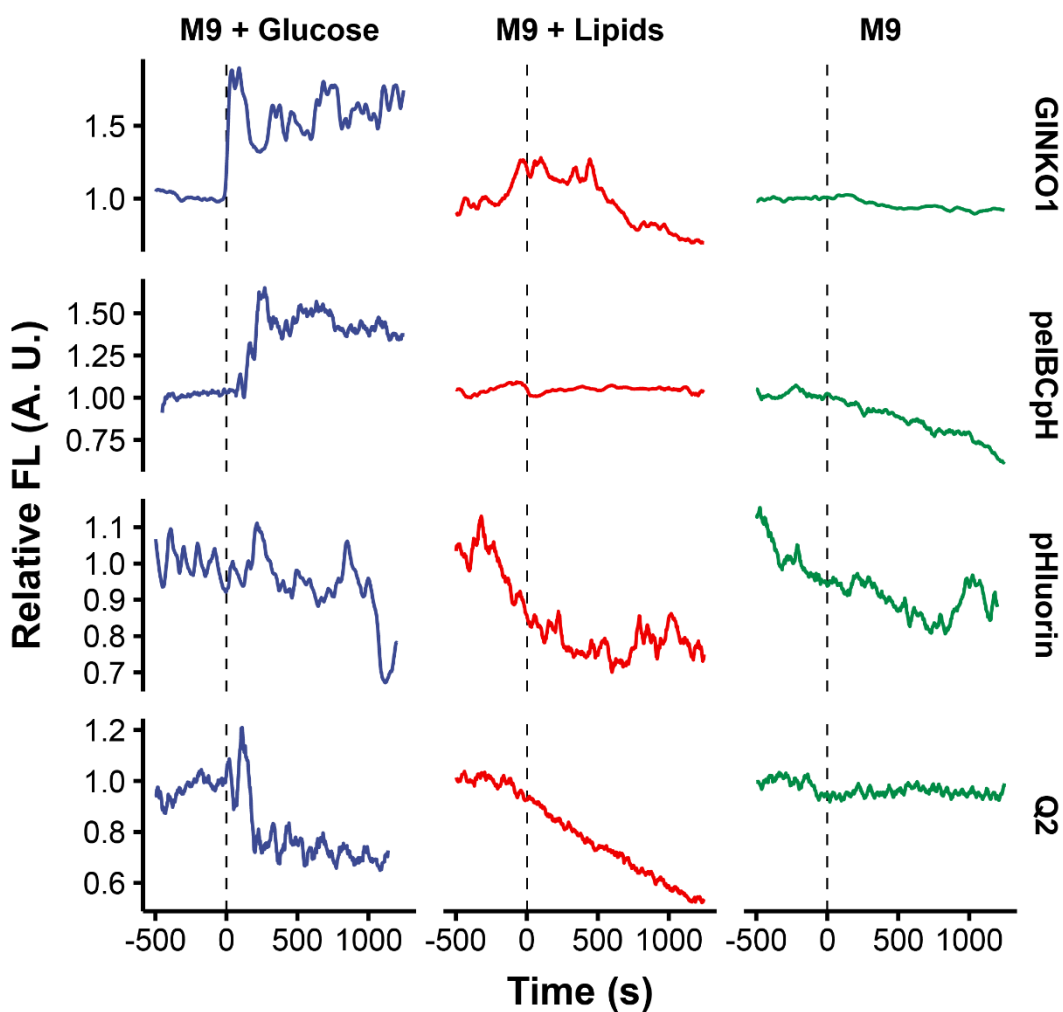


Figure 4.6: Representative traces of the electrophysiological sensors.

Each trace represents the fluorophore signal of one single cell, with one representative trace of each sensor per condition. To compare the signal across conditions, each trace was normalised to the pre-treatment condition. The grey dashed line indicates the arrival of the carbon source (glucose or lipids) or the removal of the carbon source (toM9). Single-cell tracking was done with custom python scripts using the ImageJ and TrackMate suite (see section 2.8).

Furthermore, I looked at the signal volatility after the arrival of the carbon source. First, I found that the arrival of glucose, the preferred sugar of *E. coli*, led to an increased oscillation of cytoplasmic  $K^+$  and periplasmic pH oscillations (see Figure 4.7). Second, the emergence of oscillations was significantly lower when the carbon source was lipid-based (Figure 4.7, p-val 0.0016 for GINKO1, and  $<0.001$  for pelBCpH). This behaviour was translated into membrane potential oscillations when glucose arrived but not when lipid arrived (Figure 4.7, p-value  $<0.001$ ). Finally, I found no statistical significance in cytoplasmic pH after the arrival of glucose (p-value 0.05 compared to lipids).

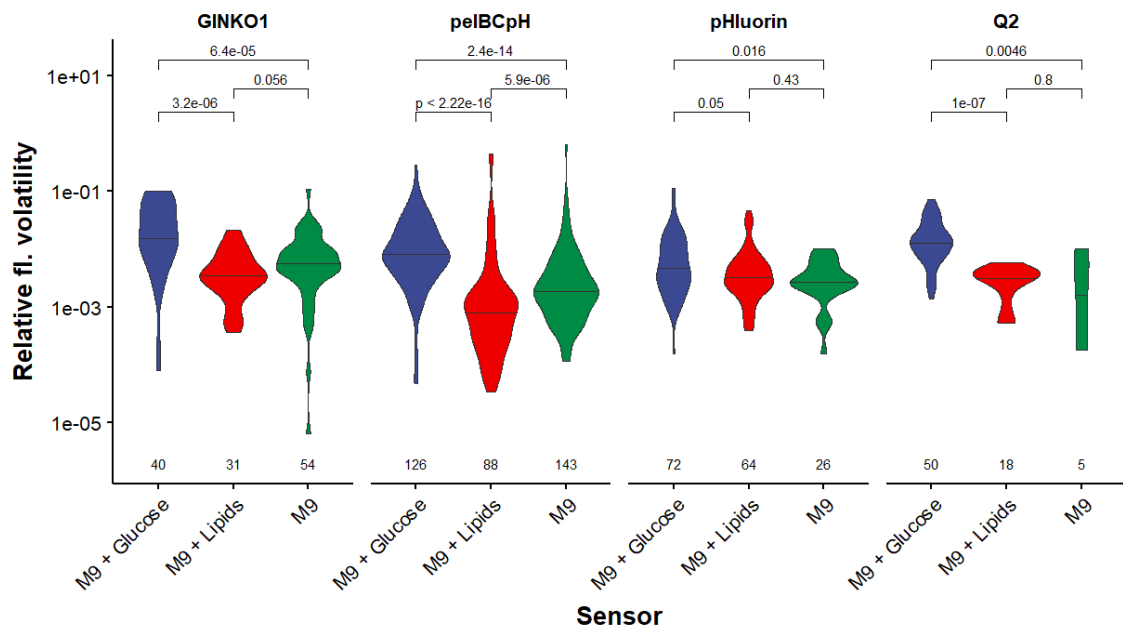


Figure 4.7: Volatility of electrophysiological ions on different carbon sources.

Violin plots of the volatility of the ion sensors on each carbon source. The volatility was calculated by measuring the variance ( $\sigma^2$ ) after the arrival of the carbon source and taking into account the next 700 seconds. The number at the bottom indicates the cell count for each condition. Comparison among each condition was made via the Mann-Whitney test.

## 4.8 Carbon sources induce membrane potential spikes

To further examine the nature of the ion oscillations, I devised a method for efficient screening of multiple conditions. For this purpose, I focused on membrane potential as representative of the general electrophysiology of the cell

using the QuasAr2 reporter<sup>323,366</sup>. Thus, I grew overnight cells, and the following day, I resuspended them in M9 supplemented with the carbon source at the desired concentration. To measure the membrane potential activity, I transferred them to agar pads containing the same carbon source and proceeded to record the QuasAr2 fluorescence under the microscope (for details, see methods 4.2). The selected carbon sources were glucose and fructose (both glycolytic and PTS-dependent), pyruvate and fumarate (gluconeogenic and independent of the PTS transport system). For the data analysis, I looked at the number of peaks under each condition. A peak or spike was defined as the rapid increase of the QuasAr2 signal above the baseline, reaching at least 1.5x (AU). Then, I modelled the data using a generalized linear model that allowed the parametrization of spike count (see Table 9). The resulting model revealed that the spike count mainly depended on the carbon source as well as the concentration (**Figure 4.8A**).

Table 9: Full description of the parametric model for spike count.

Modelling was performed with the glmmTMB package<sup>402</sup>.

<b>Full model</b>				
$y_i = \mathbf{NB}(\eta \theta, p) = \mathbb{E}(y = k \text{spiking}) * \mathbb{P}_k(y = k) + 0 * \mathbb{P}_0(\text{not spiking})$				
<b>Conditional model</b>				
$\eta = \exp(X\beta + Zb = x_1CS + x_1\log(\text{conc}) + z_1\text{replicate})$				
	Estimate	Std. Error	Z-value	p-val (P(x> z ))
CS=Glucose	0.507514	0.122212	4.153	<b>3.29e-05</b> ***
CS=Fructose	0.379303	0.119227	3.181	<b>0.00147</b> **
CS=Fumarate	-0.191135	0.134311	-1.423	0.15472
CS=Pyruvate	0.600709	0.118515	5.069	<b>4.01e-07</b> ***
Log(conc.)	0.048215	0.007671	6.285	<b>3.27e-10</b> ***
<b>Random effects</b>				
Group	Variance		Std. Dev.	
Replicate	0.0571		0.2389	
<b>Zero-Inflation model</b>				
$\text{zero inflation} = \log(p) = \beta_0^{zi} + \beta_1^{\log(\text{conc})}$				
Factor	Estimate	Std. Error	Z-value	p-val (P(x> z ))
Intercept	-1.91071	0.41511	-4.603	<b>4.17e-06</b> ***
log(conc.)	0.16131	0.04521	3.568	<b>0.00036</b> ***
<b>Dispersion model</b>				
$\text{dispersion} = \log(\theta) = \beta_1^{cs} \times CS$				
Factor	Estimate	Std. Error	Z-value	p-val (P(x> z ))
CS=Glucose	1.60467	0.09942	16.14	<b>&lt;2e-16</b> ***
CS=Fructose	1.42822	0.09393	15.21	<b>&lt;2e-16</b> ***
CS=Fumarate	1.64765	0.11293	14.59	<b>&lt;2e-16</b> ***
CS=Pyruvate	1.50995	0.08927	16.91	<b>&lt;2e-16</b> ***

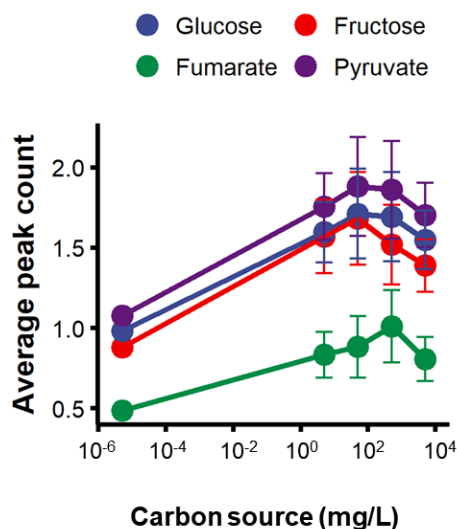


**Figure 4.8: Carbon source drives membrane potential spikes.**

Average of spikes count for every carbon source at different concentrations. The value was calculated using a generalised linear model adjusted to a negative-binomial distribution. I used the Bayes information criterion to select the fittest model. This model took into account the carbon source and concentration effect on the mean value. In addition, the model also accounted for the effect of carbon source in triggering the spiking behaviour (zero-inflation factor) and considered a different dispersion for each carbon source (see Table 9).

## 4.9 Ionophore effect on membrane potential spikes

In view of the correlation between carbon source and membrane potential spikes, I explored the impact of different ionophores. For this purpose, I grew the cells as described in the previous section while keeping the carbon source constant to 0.5 g/L glucose as a reference medium. In addition, before transferring the cells to the agar pad, I added the different ionophores for 10 minutes. The ionophore concentration was the same as described in 3.8. Consistently with other membrane potential reporters, I found that treating cells with CCCP halted all the spikes and kept the cells in a depolarised state<sup>323</sup>. This experiment revealed that most ionophores altered the cell's resting membrane potential. As mentioned, CCCP depolarised cells completely, but indole, nigericin, oligomycin and valinomycin significantly hyperpolarised the cells (Figure 4.9).

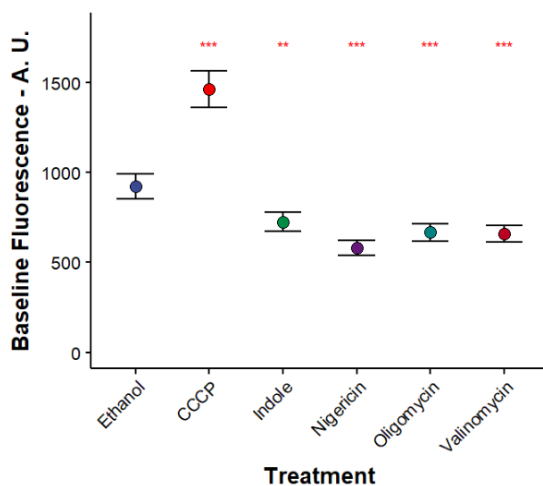


**Figure 4.9: Ionophore modulation of membrane potential baseline.**

The baseline was defined as the trace signal before and after the spike. For each condition, I took the mean of the baseline of all cells in focus. The final value corresponds to the mean of at least three biological replicates. Confidence intervals indicate the standard error. Statistical significance was calculated with a post-hoc Bonferroni test.

#### 4.10 KO strains have different QuasAr2 expression

Finally, I aimed to examine the effect of porin and ion modulator KOs on the membrane potential spikes. To this end, I transformed the KO strains (see Table 1 for the complete genotype) with the pBAD\_QuasAr2 plasmid following the procedures described in 2.3.1. Before modelling the changes in the membrane potential dynamics, I question whether the expression level of the sensor was homogeneous in all strains. For that purpose, I treated all strains with CCCP so that the signal of the membrane was fully depolarised, thus producing the highest QuasAr signal. As **Figure 4.10** shows, Kch and OmpC strains have a higher maximum signal. Thus, for further analysis, I used this value as a reference to normalise the signal of every strain.

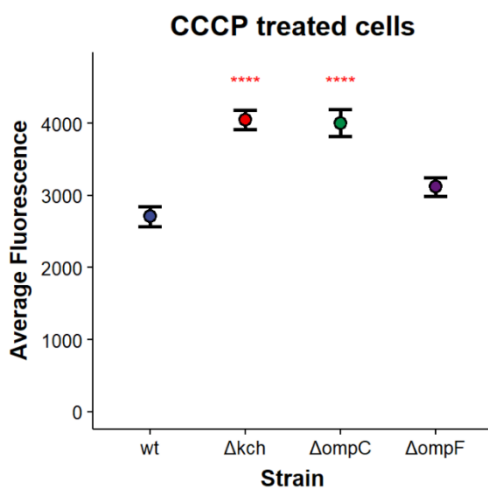


Figure 4.10: Kch and OmpC have higher QuasAr2 maximum signal

As described in the previous section (see section 4.9), cells were treated with CCCP. Next, they were placed onto agar pads and recorded for 2 mins. Each dot represents the average of three biological replicates. Confidence intervals indicate standard error. Statistical significance was calculated with a post-hoc Bonferroni test.

### 4.11 Resting membrane potential in different knockout strains

As can be seen in Figure 4.11, deletion of main porins OmpC and OmpF or the voltage-activated potassium channel Kch caused a fall in QuasAr2 fluorescence. This fall in fluorescence means that, on average, the membrane of the KO strains was more hyperpolarised.

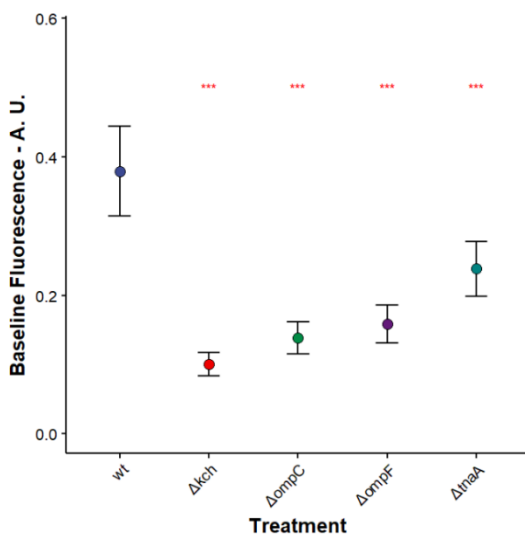


Figure 4.11: Deletion of membrane voltage regulators and porins modulates membrane potential spikes.

Changes in the baseline by each KO strain compared to WT. The baseline was defined as the trace signal before and after the spike. Also, as mentioned before, the baseline of each strain was normalised to the maximum signal calculated by CCCP addition. For each condition, I took the mean of the baseline of all cells in focus. The final value corresponds to the mean of at least three biological replicates. Confidence intervals indicate the standard error. Statistical significance was calculated with a post-hoc Bonferroni test.

### 4.12 Deletion of the Kch channel reduces the spike size

Given my interest in the role of the voltage-activated potassium channel Kch, I carried out an extended analysis of the effect this deletion had on the membrane

potential. **Figure 4.12A** shows how the  $\Delta kch$  strain had not only a lower membrane potential baseline but also an impaired spike size. The trace plots describe smaller and shorter spikes in  $\Delta kch$  compared to the WT strain. Comparing the average area under the curve between both strains revealed that this effect is statistically significant (**Figure 4.12B**, p-value < 0.001).

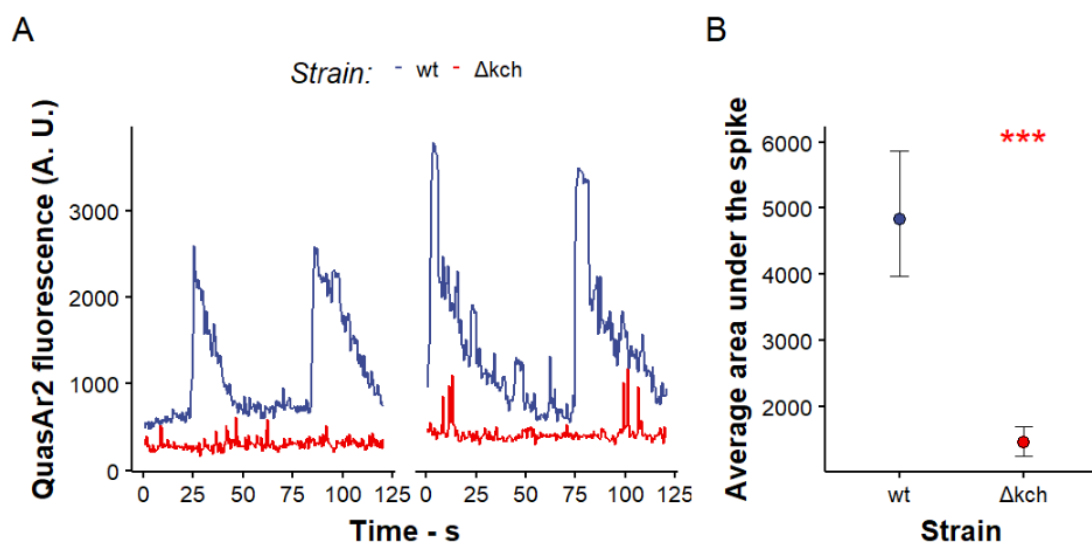


**Figure 4.12: The  $\Delta kch$  strain presents diminished spike size.**

Cells were grown overnight in SOB medium supplemented with 20  $\mu\text{M}$  retinal and 0.002 g/L arabinose. The next day, cells were washed with M9 supplemented with 0.5 g/L glucose. **A)** Trace plot of QuasAr2 fluorescence of four representative cells. The blue line denotes WT cells while the red line stands for the  $\Delta kch$  strain. **B)** Statistical comparison of the average area under the spike. To calculate this value, I integrated all the spike values and subtracted the baseline. Then, I average the mean spike of each cell for the whole population. This value was calculated for three biological replicates. Error bars represent the standard error. Statistical comparison was performed with a t-test.

### 4.13 Kch deletion causes periplasm acidification

To further understand the nature of the membrane potential spikes with the Kch channel, I examined the behaviour of the underlying ions on Kch, which are protons due to the role of pH in Kch gating<sup>403</sup>, and  $\text{K}^+$  as it the primary ion released through the channel. For that purpose, I expressed the ion reporters GINKO1 and pelBCpHuji in the  $kch$  strain and compared it with the wild type strain (see 2.3.1). Then, I grew the cells into the Mother Machine and analysed the signal of each

sensor. Here, I found no significant difference in the GINKO1 baseline signal (see **Figure 4.13A**). Nevertheless, I reported a clear difference in the periplasmic baseline pH (p-value < 0.001). My data suggested that the WT strain had a higher pH than the  $\Delta kch$  strain (**Figure 4.13B**).

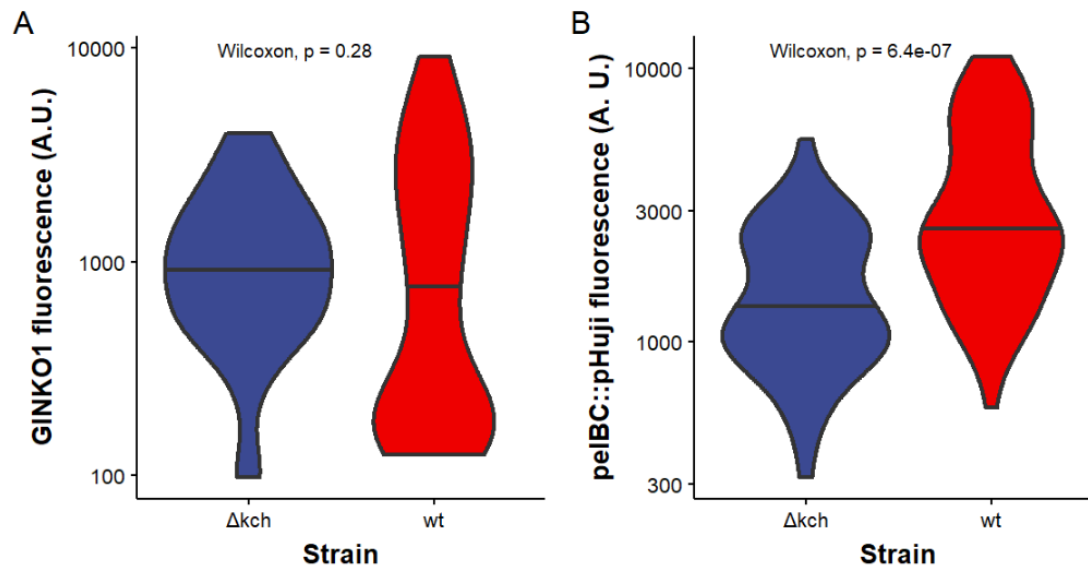


**Figure 4.13: Potassium and periplasmic pH baseline difference between WT and kch strain.**

**A)** Density plot of the GINKO1 signal from WT and kch cells expressing the reporter. **B)** Density plot of the pelBCpHuji signal from WT and kch cells expressing the reporter. For both figures, the black line indicates the 50th quantile. Also, a statistical comparison was performed via the Mann-Witney-U test using the R-base package.

#### **4.14 Changes in the carbon metabolism influence bacterial permeability**

Chapter 3 showed that the cellular pH and  $K^+$  modulate the membrane permeability of *E. coli*, and in this chapter, I demonstrated that these two ions are controlled through carbon metabolism. Therefore, I postulated the hypothesis that changes in carbon sources should also produce changes in permeability. To challenge that hypothesis, I compared the uptake of one of our fluorescent tracers under different glucose concentrations and starvation. I discarded the use of 2NBDG because it enters into competitive binding with glucose<sup>388</sup>, which means changes in 2NBDG uptake will confound this effect with the hypothetical impact of membrane potential. Thus, in order to isolate this phenomenon, I opted for

Hoechst. I observed that removing the carbon source from the cells increased the uptake of Hoechst, and this difference increased with time (Figure 4.14A). Interestingly, when I varied the glucose concentration, I noticed a higher Hoechst permeability with higher glucose (4 g/L) than low glucose (0.04 g/L). Nevertheless, as low glucose cells entered starvation, their Hoechst permeability increased (Figure 4.14B).

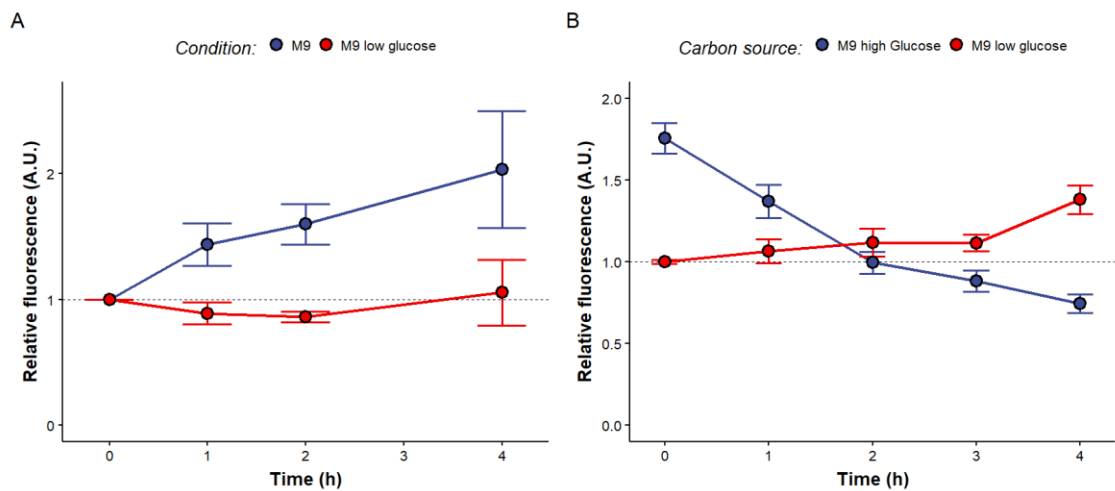


**Figure 4.14: Carbon source drives bacterial permeability.**

Cultures were grown to an OD of 0.1-0.25. the culture was split, washed with M9 and resuspended in fresh M9 + glucose (4 g/L high, or 0.04 g/L low) or plain M9 for starvation. **A)** Hoechst uptake by cells growing in no carbon source or low glucose. **B)** Hoechst uptake in low glucose (0.04 g/L) or high glucose (4 g/L). Each dot represents the average of three independent biological replicates. Error bars describe the standard error.

## **Discussion and conclusion**

In this chapter, I have provided evidence about how *E. coli* has substantial control of the pH in the cytoplasm and periplasm. In addition, the data also suggest that the proton and potassium ions are highly dynamic during growth and depend on the carbon source.

### **4.15 Cytoplasmic and periplasmic pH**

In this work, I have presented a reliable method to determine the bacterial periplasmic pH. Although there have been previous attempts to measure the periplasmic pH in *E. coli* using fluorescent proteins and click chemistry, these methods were highly problematic.

The first measurement of the periplasmic pH, published in 2007, was done with a fluorescent protein derived from GFP called GFPmut3<sup>245</sup>. The main problem of this approach emerges from the fact that the GFP signal is not responsive below pH 6. Moreover, the GFP protein does not fold properly in the reductive environment of the periplasm<sup>404</sup>. In addition, this work was based on cell bulk cultures. This method presents two problems: first, it assumes a perfect efficiency in exporting the GFPmut3 to the periplasm, which is a particular concern because the report mentions the use of the twin-arginine translocation (or Tat) export system<sup>405</sup>. This pathway requires the protein to be folded in the cytoplasm before export. Thus, it can confound cytoplasmic fluorescence with periplasmic fluorescence. Second, fluorometric assays on bulk suspension cultures only give the average signal for the population. Thus, this technique cannot account for the variability of the reporter among cells and is indifferent to the reporter locations within the cell.

The other report that studied periplasmic pH was based on click-chemistry<sup>406</sup>. This novel technique is based on the reaction of small molecules with biological targets. This work presented a method that targeted the periplasm with high precision.

Briefly, they expressed a modified chaperone (HdeA) in the periplasm. When the dye BTTP-Cu is added to the medium, it can react with a target protein located in the periplasm producing a stable fluorescent compound. Nevertheless, given the nature of the compounds used in the chemical reaction, the dynamic range of this method (pH between 5 and 2) was below the main physiologically relevant parameters of *E. coli* (pH between 4 to 8).

The reporter presented in this work, pelBCpHuji, allowed a precise localisation in the periplasmic region, delivering an accurate pH measurement. Interestingly, I found that in the absence of CCCP, the periplasm has some pH buffering capacity. This observation could seem very controversial because the pore diameter of *E. coli* porins is much larger than a proton. Our molecular dynamic simulation in chapter 3 suggested that a change in protonation of the periplasmic residues could generate an electrostatic shield that helps to keep the ions in the periplasmic chamber (see section 3.14). However, further work is required to explain the precise mechanism by which porins might regulate proton flow at the molecular level. Mutational studies of the periplasmic residues should help to verify our hypothesis. Still, this work supposes a significant contribution to our understanding of the periplasmic space and opens the door to studying the proton motive force from a new perspective.

#### **4.16 Buffering of the cytoplasmic K<sup>+</sup>**

In addition, I also tried to calibrate the potassium sensor GINKO1. Although I treated cells with valinomycin, I found very little change in the cytoplasmic K<sup>+</sup> levels despite large changes in extracellular K<sup>+</sup>. A reasonable hypothesis could be that valinomycin only partitions into the outer membrane. Thus (i) changes in cytoplasmic K<sup>+</sup> might be secondary to changes in periplasmic K<sup>+</sup>, and (ii) the observed effects on porin permeability when changing external K<sup>+</sup> in the presence

of valinomycin could reflect an effect of periplasmic  $K^+$  on porins. I attempted to answer this question directly by developing a periplasmic reporter for potassium, but unfortunately, the GINKO1 sensor was not stable in the periplasmic environment. A potential alternative could be using the sensor KIRIN1, which is based on YFP and CFP, which are much more stable at lower pH<sup>367</sup>.

#### **4.17 Ion oscillations and carbon source**

Single-cell measurements using the Mother Machine revealed fluctuations of potassium and hydrogen ions. This evidence is consistent with the fact that gram-negative bacteria use a proton gradient to produce energy, transport solutes across the membrane, and other biological functions (see section 1.4.4.6). Looking at the different ions, I found considerable periplasmic pH oscillations, yet the cytoplasmic pH appeared much more stable. A possible explanation could be the volume difference between the compartments. In addition, changes in the cytoplasmic pH might activate proton exchange to keep the cytosol near-neutral pH.

I then proceeded to show how carbon sources are at the root of the ion oscillations. I showed that glucose triggers robust potassium and hydrogen fluctuations, which in turn causes membrane potential oscillations. Contrarily, when I supply bacteria with lipids or plain M9, I observe slower membrane depolarization but much lower ion volatility. A reason for this could be that glucose uptake could activate the metabolism, and the ETC generates the ion oscillations.

Next, I looked at the membrane potential of *E. coli* using QuasAr2 analysis (see 4.8 and 4.9). Consistent with my previous results, I found that supplying the cells with preferred carbon sources such as glucose, fructose or pyruvate was correlated with a highly spiking phenotype. On the opposite side, I found that feeding cells with fumarate produced much fewer spikes (See section 4.8). I then treated the cells with different ionophores to show that the disruption of the proton gradient

with CCCP completely abolished the spiking phenotype. In addition, treating the cells with oligomycin reduced the resting membrane potential, suggesting the ATPase's involvement. Next, a set of KO strains expressing QuasAr2 revealed that the  $\Delta ompF$ ,  $\Delta ompC$  and  $\Delta kch$  had a much lower resting membrane potential than WT.

Finally, I must address a potential limitation when working with agar pads while measuring membrane potential. The problem emerges from the interference of mechanosensitive channels. The Kralj lab has been working on the relationship between the membrane potential and the mechanosensitive channels of bacteria<sup>324</sup>. His team has shown that transferring cells from liquid to solid medium generates calcium spikes. Thus, measuring the effect of carbon sources on the membrane potential spikes on an agarose pad might be potentially affected by the calcium spikes from the mechanosensitive channels. Whilst I tried to account for this effect by including a lag time step before imaging, a cleaner approach could be undertaken using the Mother Machine. However, this method requires longer times, limiting the number of conditions that could be tested. Another alternative could be the use of ion-specific sensors such as pelBCpHuji or equivalent for other ions.

A deeper study on the  $\Delta kch$  strain revealed that this deletion generated not only a lower resting membrane voltage but also smaller spikes. I also illustrated that the reason for the lower membrane potential in  $\Delta kch$  was the much lower periplasmic pH. This phenomenon suggests that potassium plays a substantial role in setting the proton gradient, and this is likely mediated via Kch.

### 4.18 Carbon source drives permeability

Lastly, I looked for evidence that the ion changes caused by carbon sources also affected permeability. Measuring Hoechst uptake under different glucose concentrations showed that starving cells had the highest permeability while low carbon sources caused low permeability.

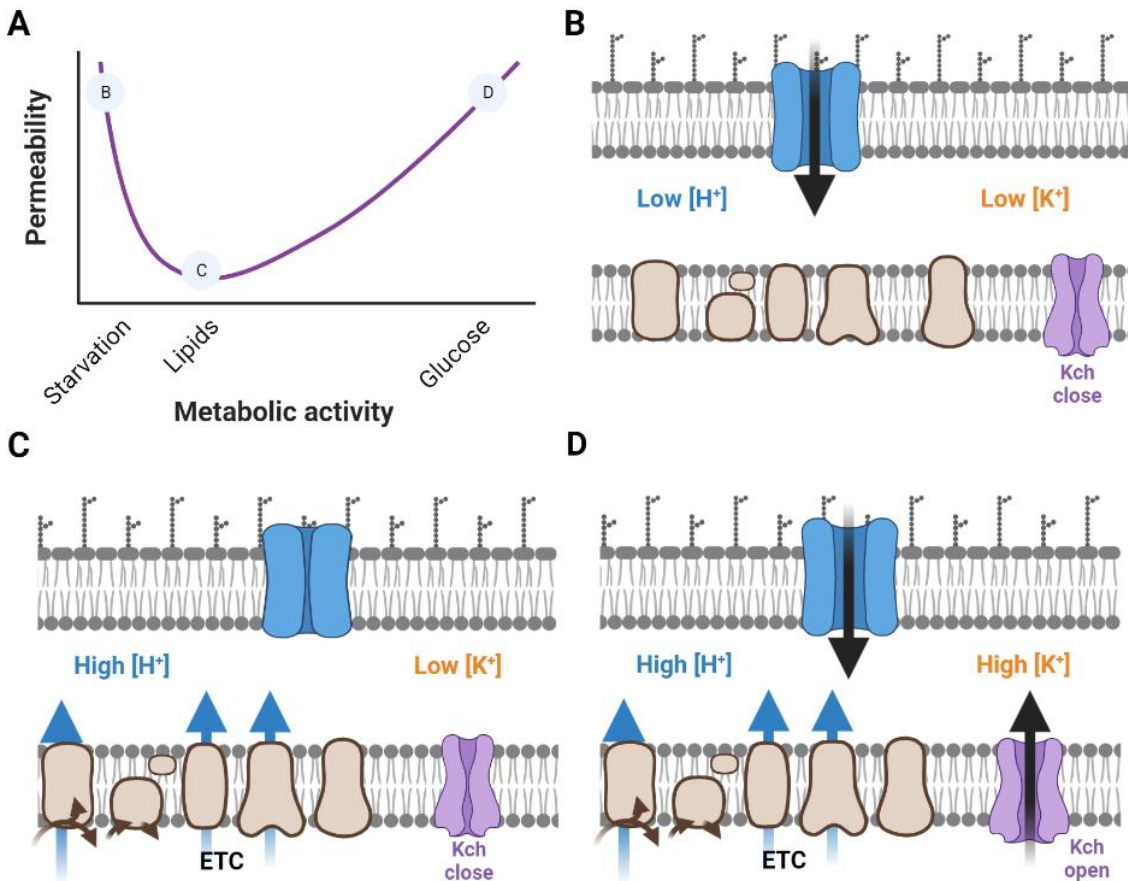


Figure 4.15: Diagram for the regulation of the periplasmic ions and permeability

(A) Correlation diagram between membrane permeability and metabolic activity where the model predicts a U-like behaviour. Thus, under starvation or high glucose conditions, the permeability is expected to be high, but when the metabolic activity is low, such as in the presence of lipids or low glucose, the permeability is low. Next, panels B-D show a representation of the bacterial membrane through the different conditions. Under starvation (B), the ETC cannot sustain a proton gradient; thus, low periplasmic proton concentration allows the porins to open, facilitating the entrance of nutrients. Once the nutrients access the cellular compartment, the ETC starts pumping protons into the periplasm (C). The increase of proton concentration in the periplasm interacts with the porins reducing the pore diameter and with it the membrane permeability. The proton gradient will be used for energy generation or other biological processes. Finally, if excessive hyperpolarisation occurs (D), the Kch channel opens, and this inundates the periplasm of potassium. This increase of potassium in the periplasm re-opens the porin.

All in all, I propose to understand these results under the model described in **Figure 4.15**. I hypothesize an inverse parabolic relation between metabolic activity and permeability (**Figure 4.15A**). Under starvation (**Figure 4.15C** with predicted low periplasmic  $H^+$  and  $K^+$ ), porins are open. Porins shut when bacteria are exposed to low glucose media (**Figure 4.15B** where periplasmic  $H^+$ , but not  $K^+$ , levels rise). However, under conditions of high metabolism, Kch is activated, leading to low  $H^+$  and high  $K^+$  levels in the periplasm, which allows porins to open (**Figure 4.15D**).

#### **4.19 Conclusion**

In conclusion, this is the first study providing a combined measurement of all the relevant ions ( $H^+$ ,  $K^+$  and  $Ca^{2+}$ ) for bacterial physiology. The data exposed in this chapter provide strong evidence that protons and potassium oscillate in exponential growing cells and that these oscillations depend on carbon metabolism. I also describe how  $\Delta kch$  presents a general disruption of the membrane potential homeostasis. Then, I connected these findings with the permeability phenotypes described in the previous chapter. Finally, I present a tentative model to explain the mechanism underpinning the coordination of the periplasmic ion oscillations with the bacterial permeability.

# **Chapter 5: THE CARBON SOURCE INFLUENCES ANTIBIOTIC RESISTANCE THROUGH MEMBRANE PERMEABILITY**

## Summary

Membrane permeability is one of the significant factors that contribute to antimicrobial resistance. Since I have shown the effect carbon sources have on membrane permeability, this chapter aims to evaluate the impact of this phenomenon on antibiotics uptake and susceptibility.

Using the Mother Machine to measure the accumulation of the autofluorescent drug ciprofloxacin, I found a reduced uptake in porin knockout strains (as expected). In addition, the measure of CIP uptake in the efflux pump KO  $\Delta tolC$  confirmed that this difference was not related to a change in efflux activity, supporting the use of this method to monitor porin mediated permeability. Interestingly, I also found that  $\Delta kch$  showed a reduction of ciprofloxacin entry. Supplying cells with either lipid or glucose, I observed that carbon metabolism modulates ciprofloxacin permeability because feeding cells with lipids decreased CIP uptake compared to cells growing in glucose. In line with our previous findings, the carbon source effect was mediated through changes in periplasmic ions. Remarkably, I found that glucose concentration had an inverse effect in the  $\Delta kch$  strain and WT; that is, higher glucose concentration decrease CIP uptake in the  $\Delta kch$  strain.

As expected, changes in carbon source utilisation led to differences in susceptibility to ciprofloxacin. This effect was presumably porin dependent because treating cells with porin independent antibiotics revealed no difference in susceptibility. Lastly, metabolic mutations helped further to define the impact of carbon sources in antibiotic uptake. This data confirms that carbon source availability can strongly influence antibiotic susceptibility. This work suggests a mechanistic model for the impact of different carbon sources and highlights the

need to consider the metabolic control of porin permeability in creating new antibiotics.

*I have performed all the experiments and analyses described in this section except for the ciprofloxacin minimal inhibitory concentration, which was performed by Dr Ieuan Evans.*

## Introduction

Antimicrobial resistance has become a significant threat to global health, with treatment failures in patients with antibiotic-resistant infections are predicted to cause 10 million deaths annually by 2050<sup>407</sup>. Gram-negative bacteria are of particular concern due to the high intrinsic resistance associated with their double-membrane. As described in section 1.3, the outer membrane creates a formidable permeability barrier to the entry of hydrophilic and hydrophobic molecules. Therefore, most antibiotics' transport is dependent on porins for their uptake (Section 1.3.2). The main problem for understanding this process arises from the lack of quantitative methods for studying drug accumulation in single cells.

Recently, Cama et al. developed a very innovative technique to quantify antibiotic uptake in live cells using the Mother Machine<sup>375</sup>. They took advantage of the auto-fluorescent antibiotic ciprofloxacin to study its uptake in hundreds of individual bacteria confined in well-defined microenvironments<sup>375,408</sup>. Thus, I used this platform to study the effect of carbon sources on bacterial permeability. This technique allowed us to confirm my findings from chapter 3 (see section 3.8) and chapter 4 (see section 4.7) with a label-free antibiotic.

My findings in chapter 4 suggest that membrane potential depends on carbon source metabolism (see section 4.7). On top of this, carbon source availability and metabolism have been shown to impact antibiotic susceptibility in a range of different bacterial species (*E coli*, *Acinetobacter baumannii* and *Staphylococcus aureus*)<sup>409,410</sup>. The factors involved in this phenomenon are diverse<sup>26,362,409,410</sup>. In this chapter, I will explore the hypothesis that carbon sources modulate bacterial permeability. Understanding how this part of the metabolism influences antibiotic

resistance in more detail is critical in guiding future drug development and optimising treatment strategies.

I simultaneously imaged ciprofloxacin accumulation in individual *E. coli* in real-time using the auto-fluorescence of the drug. I validated my technique by studying ciprofloxacin accumulation in three *E. coli* strains from the Keio collection, encompassing the wild type (WT), the porin knockout OmpF and OmpC, and the TolC efflux protein knockout ( $\Delta tolC$ ) strain. In addition, I studied the effect of deleting the voltage-activated potassium channel Kch. Finally, I analyse the impact of carbon source supply on ciprofloxacin uptake. Finally, I show how this effect translates into antibiotic efficacy.

## **Material and methods**

### **5.1 Ciprofloxacin uptake in the Mother Machine**

Ciprofloxacin uptake was measured in a Zeiss 780, equipped with a UV light source (DPSS 355 nm 60 mW, Coherent), which allowed ciprofloxacin imaging. This instrument was also equipped with a thermal isolation box to keep the temperature constant at 37 °C. The imaging was done with a 63x/1.4NA Oil lens. Ciprofloxacin fluorescence detection was done with a modified DAPI filter setting (435/65 nm)<sup>375</sup>.

Cell trapping in the Mother Machine followed the protocol described in section 2.5. Then, I resuscitated the cells in the specified medium for 90 minutes at 0.150 mL/h, at which point I switched the syringe to the specified medium plus 12.5 µg/mL ciprofloxacin. I increased the flow to 1 mL/h and waited 3 minutes. At this point, I started recording. Finally, after 15 min, I decreased the flow back to 0.15 mL/h.

### **5.2 MIC and EC50 calculation**

Effective concentration 50 (EC50), defined here as the drug concentration that induces 50% maximal inhibitory effect on cell growth<sup>411</sup>, was determined for *E. coli* according to the Clinical and Laboratory Standards Institute (CLSI) method M07-A9<sup>412</sup>. Briefly, *E. coli* were grown to an optical density (A600 nm) of 0.2–0.3 in liquid culture, and  $1 \times 10^5$  bacteria were added to each well of 96-well plates containing serial dilutions of the antibiotic, in triplicate wells per condition, and incubated at 37°C until growth was seen in the control wells. Then, the turbidity absorbance at 600 nm was measured with a ClarioStart (BGM LABTECH). Finally, the data were

fitted to a dose-response model using a 4-parameter logistic regression equation<sup>413</sup>.

## Results

### 5.3 Porin mediates ciprofloxacin uptake

In chapter 3, I showed that bacterial permeability depends on the ionic environment in the periplasm, and this factor is conditioned by carbon metabolism (Chapter 4:). Therefore, I adapted my microfluidic setup to test the effect of carbon source and membrane potential on ciprofloxacin uptake. Ciprofloxacin is a quinolone that exhibits natural autofluorescence upon 360 nm light excitation<sup>375</sup>. Consequently, I exploited this feature to study ciprofloxacin uptake *in situ*. For this aim, I grew *E. coli* strains overnight in supplemented M9 and trapped them in the Mother Machine (see section 2.5). Then, I provided them with the same medium for 90 min. After that time, I added 1.2  $\mu\text{g}/\text{mL}$  of ciprofloxacin to the flowing media. Although this concentration is 10 times the MIC<sup>414</sup>, it allowed optimal fluorescence within our microscopy setup. **Figure 5.1** shows that my system was capable of detecting ciprofloxacin uptake. In line with other research, this analysis confirms that the transport of ciprofloxacin is mediated by porins  $\Delta ompF$  and  $\Delta ompC$ <sup>375,415</sup>. Also, the uptake profile of  $\Delta tolC$  confirms that the difference in uptake is not due to changes in efflux pump activity under the timeframe. Finally, I noticed that glucose uptake by  $\Delta kch$  is also impaired.

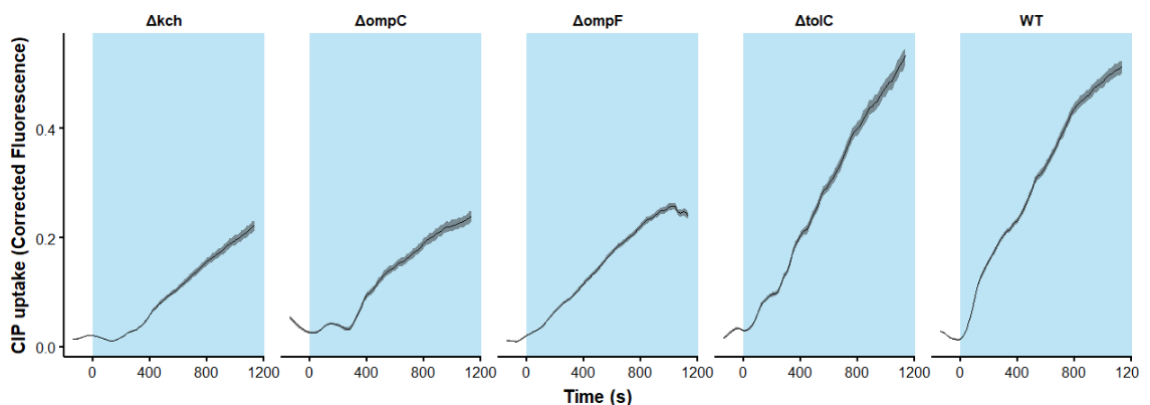
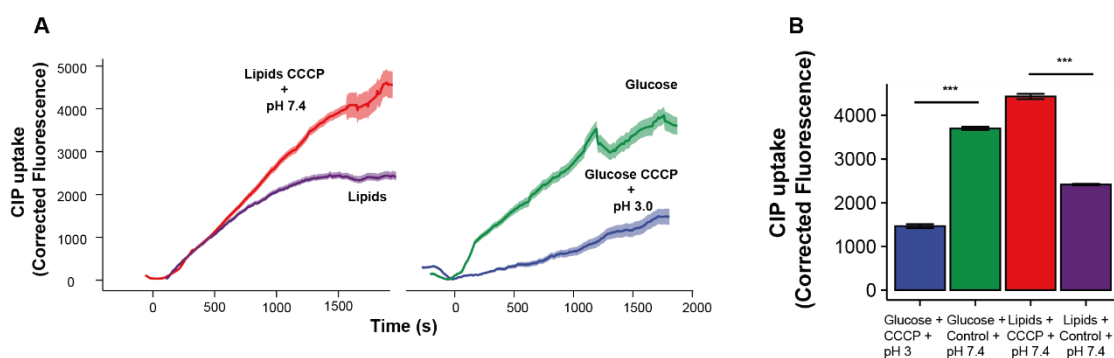


Figure 5.1 Individual ciprofloxacin accumulation experiments for the bacterial KO investigated.

The blue background indicates the arrival of ciprofloxacin into the Mother Machine. The black line denotes the average ciprofloxacin fluorescence within the cells. The cell fluorescence values are reported after correcting for the background, subtracting the initial cellular auto-fluorescence at  $t = 0$ . Then, fluorescence intensity was normalised to the maximum fluorescence of WT cells to normalise data across experiments. The shaded area indicates the standard error of three biological replicates.

## 5.4 Periplasmic pH drives the carbon source effect

Chapter 3: showed that the permeability of the periplasmic environment depends on the proton and potassium concentration and that the carbon metabolism drives these factors. Thus, I proceeded to analyse the effect of carbon sources on ciprofloxacin uptake. For this purpose, I grew *E. coli* cells in M9 supplemented with 4 g/L glucose or lipid source for 90 minutes (see section 2.2.2). Then, I switched the medium supply to the one with the same composition plus ciprofloxacin, and I started monitoring the uptake of the compound for ~25 minutes. **Figure 5.2A** reveals that the uptake process of bacteria growing in lipids is slower than bacteria growing in glucose. I then simulated a hyperpolarised phenotype with CCCP and low pH, implying a high proton concentration in the periplasm. This experiment revealed that cells treated with CCCP at low pH lost their permeability (**Figure 5.2B**,  $p$ -value  $< 0.001$ ). In contrast, cells growing on lipids showed an increase in CIP uptake when treated with CCCP at pH 7.4 (**Figure 5.2B**,  $p$ -value  $< 0.001$ ).



**Figure 5.2: Carbon source drives ciprofloxacin permeability.**

**A)** Fluorescent profile of *E. coli* under different carbon sources. Solid coloured lines represent average across experiments. The shaded area indicates the standard error. The cell fluorescence values are reported after correcting for the background, subtracting the initial cellular auto-fluorescence at  $t = 0$ . **B)** Comparison of ciprofloxacin fluorescence within cells at  $t > 1500$ . The statistical comparison was made via the Mann-Witney-U test (Wilcox test).

## 5.5 Kch effect on permeability depends on carbon source

In order to examine the carbon source effect interaction with the Kch channel, I examined the ciprofloxacin uptake of the WT and  $\Delta kch$  strains under different carbon concentrations. The hypothesis was that higher glucose concentration would lead to an activation of the Kch channel, which increased periplasmic potassium and increased permeability. The result showed that higher glucose concentration increased the CIP permeability of WT (Figure 5.3). Interestingly, this phenotype is the opposite in the  $\Delta kch$  strain (see Figure 5.3); that is, less CIP was uptaken at high glucose compared to low glucose.

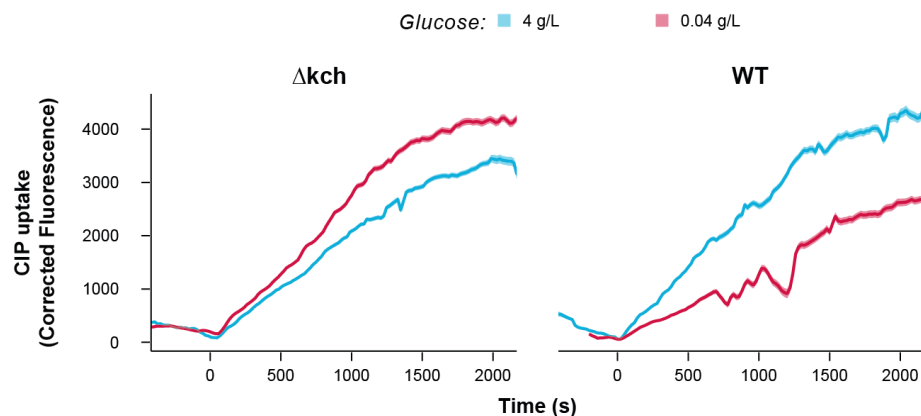


Figure 5.3: Ciprofloxacin uptake on  $\Delta kch$  and WT strain at different glucose concentrations.

For this experiment, cells were prepared as described in section 5.1. The carbon source was M9 supplemented with 0.04 g/L glucose (low glucose) or 4 g/L glucose (high glucose). The cell fluorescence values are reported after correcting for the background, subtracting the initial cellular auto-fluorescence at  $t = 0$ . The solid coloured line indicates the population average. The shaded area indicates the standard error.

## 5.6 The $\Delta kch$ strain and porin knock-outs are more resistant to ciprofloxacin but not to colistin

The previous section described how ciprofloxacin uptake depended on porins and the carbon source. Next, I assessed the effect of the porin knock-out and Kch KO

on ciprofloxacin bactericidal efficacy. For this purpose, I treated liquid bulk cultures with increasing ciprofloxacin concentrations and measured the optical density at 24 hours. This data was fitted to a dose-response model, and then I compared the EC<sub>50</sub> (Figure 5.4A). As reported before (see Figure 5.1), ciprofloxacin efficacy is severely affected by porin deletion (p-value < 0.001). In addition, I found that Kch deletion also decreases antibiotic efficacy. When I compared the effectiveness of a permeability independent antibiotic such as colistin on these strains, I found no significant difference (Figure 5.4B).

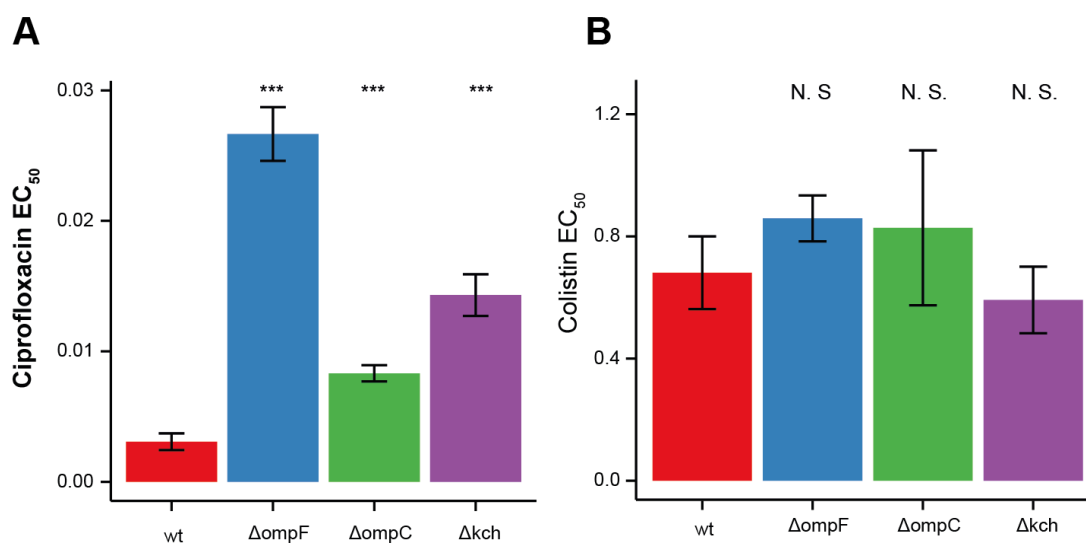


**Figure 5.4: Effective concentration of ciprofloxacin and colistin**

Bacterial cultures were grown on M9 + 1 g/L glucose + 1 g/L casamino acids + 1 mM tryptophan. When they reached the exponential phase, I treated them with serial dilution concentrations of the antibiotic and read the optical density (600 nm) at 24h. This data was fitted to a dose-response curve. **A)** Ciprofloxacin effective concentration 50% for each strain (see section 5.2). **B)** Colistin effective concentration 50% for each strain. In both cases, the parameter was extracted from the model and averaged across replicates. The confidence interval indicates the standard error. Statistical significance was measured via a t-test with the WT as reference.

## 5.7 Carbon source modulates ciprofloxacin MIC

With the help of Dr Ieuan Evans (Floto Lab), I tested whether changes in susceptibility of *E. coli* to ciprofloxacin observed above were due to utilisation of different carbon sources (rather than changes in the levels of exposure of the drugs due to the media). To achieve this, we compared the growth rates in different carbon sources of wild type *E. coli* and knockouts for AceA ( $\Delta aceA$ ), which

cannot utilise lipids, and PtsH ( $\Delta ptsH$ ), which cannot utilise glucose. We found, as expected, that (i) wild type and  $\Delta aceA$  cells were susceptible to ciprofloxacin in glucose media (and that  $\Delta ptsH$  strains failed to grow), while (ii) in lipid media (0.3 g/L casitone, 0.05% Tyloxapol, and the lipid 1,2-dipalmitoylphosphatidylcholine at 14 mg/L), wild type and  $\Delta ptsH$  cells were resistant to ciprofloxacin (and that  $\Delta aceA$  strains failed to grow). Importantly, when exposed to mixed media (50% glucose and 50% lipid media), wild type cells remained susceptible to ciprofloxacin (presumably because they are predominantly utilising glucose) and also  $\Delta aceA$  remain susceptible (because they have to utilise glucose). In contrast, the  $\Delta ptsH$  strain became resistant (likely because they are forced to utilise lipids) (**Figure 5.5**).

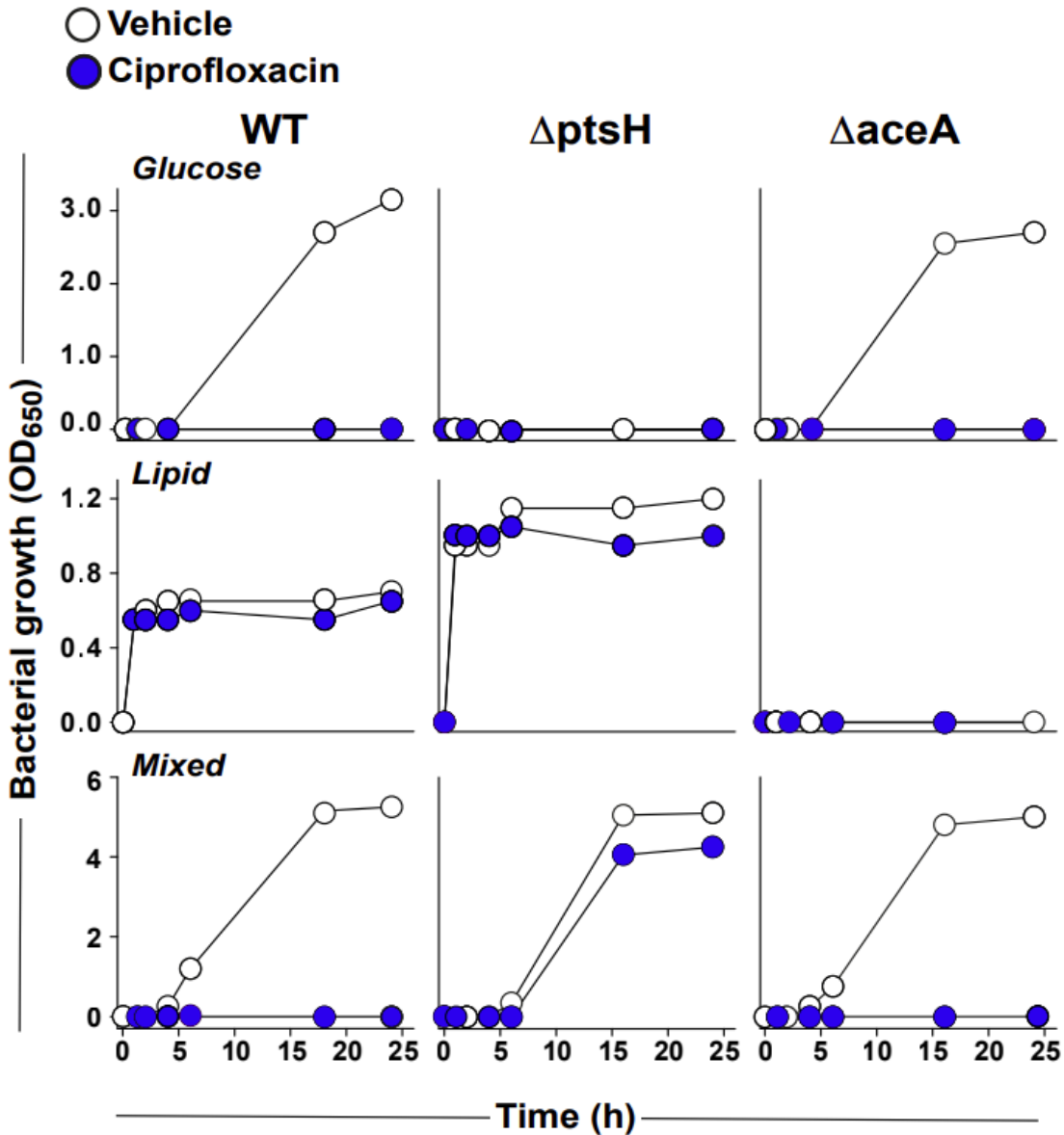


Figure 5.5: Susceptibility of the *E. coli* strains (WT,  $\Delta ptsH$  and  $\Delta aceA$ ) to ciprofloxacin in glucose, lipid and mixed media.

A low concentration of ciprofloxacin (0.0125 mg/L) was used in each experimental condition. The WT strain exhibits clear differences between the untreated control and the test conditions in both the glucose and mixed media. However, in the lipid medium, the control and the treatment conditions all grow at the same rate.  $\Delta ptsH$  exhibits the same growth as the untreated control in lipid and mixed media but fails to grow in glucose medium (higher starting concentration of organisms was required to achieve growth in the *ptsH* strain in lipid medium).  $\Delta aceA$  behaves in the same way as the WT, showing no growth in any of the treatment conditions in the glucose medium, reduced susceptibility compared to the WT in mixed medium and fails to grow in lipid medium.

## **Discussion and conclusion**

In this chapter, I have demonstrated that the type of carbon source available to *E. coli* modulates the antibiotic permeability to ciprofloxacin. In addition, I show that this effect is reflected in the MIC data.

### **5.8 Carbon source drives membrane permeability**

In accordance with previous reports, this work shows that ciprofloxacin uptake requires porin permeability<sup>375</sup>. I also found that the  $\Delta kch$  strains presented a decreased ciprofloxacin permeability compared with WT. When looking at the carbon source effect, I observed that the bacteria growing on lipids had a slower ciprofloxacin uptake than glucose. One explanation for this difference could be that the carbon source alters the porin's expression. Nevertheless, I show that treating cells with ionophores could restore cell permeability, suggesting regulation by periplasmic ions.

However, modulating the intracellular ions with ionophores and medium pH could also be problematic because it alters the protonation state of ciprofloxacin. Indeed, it has been reported that the changes in quinolone protonation affect its permeability through porins<sup>416</sup>. A potential method to modulate periplasmic pH without altering the medium pH (and with it CIP protonation) could be the use of the ArchT proton pump described in Chapter 3:. This tool could allow the modification of the periplasmic pH environment without affecting the ciprofloxacin protonation.

Furthermore, I provide evidence that the voltage-activated channel Kch mediates the carbon source effect on permeability. The evidence suggests that at high

glucose concentration, Kch activation increases the permeability because the knock-out strain had lower permeability than WT. Interestingly, the use of low glucose concentration reduces the WT strain's permeability while increasing the permeability of the  $\Delta kch$  strain.

A drawback of our approach is that ciprofloxacin has a cytoplasmic target. That means our measurements could confound changes in inner membrane permeability with outer membrane permeability. Therefore, I would suggest extending the analysis of the carbon source impact on the MIC and uptake of other antibiotics. Particularly, studying the uptake of penicillin derivatives could greatly help to elucidate this question because the penicillin target is located in the periplasm. In other words, these molecules only need to cross one membrane before reaching their target. Thus, if carbon source also affects the permeability of these compounds, that would further strengthen the idea that carbon metabolism regulates outer membrane permeability.

## **5.9 Carbon source affects antibiotic susceptibility**

The evidence presented in this chapter indicates that porins and the Kch channel condition ciprofloxacin susceptibility. The porin effect can be clearly explained as a reduction in uptake because, as I have shown, ciprofloxacin uptake is mediated by OmpC and OmpF (see Figure 5.1 and Figure 5.4). Still, some researchers have proposed that the main parameter affecting antibiotic efficacy is growth rate so that the faster grow the cells, the more vulnerable they become<sup>417,418</sup>. The reason behind this phenomenon could be that the uptake of the antibiotic through the inner membrane requires active transport. This idea is also supported by the fact that treating *E. coli* with colistin generates similar EC50 in all strains (see Figure 5.4).

Finally, the effect of  $\Delta kch$  on antibiotic efficacy could respond to a lower potassium concentration in the periplasm and thus lower permeability (as described by the

## Chapter 5: The carbon source influences antibiotic resistance through membrane permeability

model shown in Chapter 3:). However, further work is needed to validate this hypothesis. For example, generating Kch variants with target-directed mutation should help to evaluate if the cell permeability could be altered with an always-open or always close channel. If true, measuring the antibiotic susceptibility of  $\Delta kch$  in different carbon sources should mirror the permeability profile data. These experiments are already ongoing.

The results of *E. coli* WT,  $\Delta ptsH$ , and  $\Delta aceA$  strains in different carbon sources are, again, strongly suggest that the carbon source mediates porin permeability, which in turn results in changes in antibiotic susceptibility. In line with our model, the data show how glucose availability increases antibiotic permeability and susceptibility compared to lipid media (see Figure 5.2 and Figure 5.5). Moreover, the data from mixed media provide an unequivocal indication of how the mere presence of glucose increases the susceptibility of the WT strain.

Within the context of the diauxic shift<sup>342</sup>, one would imagine that the whole *E. coli* population begins metabolising glucose and thus becomes susceptible to ciprofloxacin before switching to the use of lipids. Others, however, have proposed that the “diauxic shift” is indeed composed of two subpopulations growing simultaneously: one population uses the preferred carbon source while the other consumes the alternative carbon source<sup>419,420</sup>. If this would be the case, then the subpopulation using glucose must be much greater than the one using the lipids because the data do not show a slower growth curve even after 24h of sampling (see Figure 5.5). In addition, the growth curve of the  $\Delta ptsH$  strain suggests that the glucose growing population relies upon this transporter because this KO do has a delayed and slower growth curve, while  $\Delta aceA$  follows a similar susceptibility pattern to ciprofloxacin than WT. It could then also be that a more extended

sampling could make this theoretically delayed growth apparent even in the WT strain.

## **5.10 Conclusion**

Whilst this evidence demonstrates that carbon source impacts antibiotic susceptibility in *E. coli*, it does not provide an indication of a mechanism of action for changes in porin permeability. Other questions exist around a number of possible mechanisms by which carbon sources could affect antibiotic susceptibility. These include how certain carbon sources impact growth, porin expression and bacterial energetics<sup>418</sup>.

# **Chapter 6: INDOLE PRODUCTION REGULATES MEMBRANE POTENTIAL**

## Summary

The bacterium *E. coli* produces a substantial quantity of the signalling molecule indole, which has been shown to act as a protonophore and proposed to act as a physiological method to cause membrane depolarization. Recent work has suggested that most indole is produced as a pulsed release before the stationary phase. This study aimed to understand the principles regulating indole production, which is the only known ionophore naturally produced by *E. coli*.

I measured indole production by *E. coli* utilising glycolytic and gluconeogenic carbon sources. Our data suggest that gluconeogenic carbon sources synthesize indole continuously rather than in a pulse. I confirmed this finding by measuring the tryptophanase (TnaA) expression responsible for indole production. This analysis also supports the continuous indole production on gluconeogenic carbon sources. In addition, increased glycolytic concentration delays the indole pulse.

Next, I evaluated the impact of indole production on the bacteria membrane potential. Using the fluorescent probe Oxonol-VI as a proxy for membrane potential, I found a consistent difference between glucose and fumarate. Although the cells growing in fumarate did not show a change with the presence of tryptophan, bacteria growing on glucose presented a change at the entrance to the stationary phase, when indole is being produced.

Finally, I also found an effect on the cytoplasmic pH because treating cells with indole permeabilised cells to protons. In addition, WT and the  $\Delta tnaA$  strain showed a considerable difference in pH during growth. Altogether, this suggests indole might act as a natural proton regulator in *E. coli*.

*I have performed all the experiments and analyses described in this chapter.*

## Introduction

Indole production is mediated by increased synthesis of the enzyme tryptophanase (TnaA), encoded by the *tnaA* gene. Tryptophanase converts tryptophan into indole, pyruvate and ammonia<sup>329,331,338</sup>. Tryptophanase expression is controlled by the catabolite repression protein and the TorR two-component signal (see section 1.5.5). In addition, the concentration of indole depends very closely upon the amount of tryptophan in the growth medium<sup>337,338,341</sup>.

Gaimster and colleagues have recently shown that indole production is rapidly upregulated in the early exponential phase<sup>331</sup>. This sudden pulse in indole production allows the internal concentration of indole to spike, reaching concentrations close to 20 mM<sup>331</sup>. This very high concentration has been shown to depolarise cells. It has been proposed that this happens via proton leak because indole allows the flow of protons across lipid vesicles<sup>329</sup>.

Therefore, this work aims to understand the roots of indole pulse regulation. This phenotype will be studied directly through the measurement of indole concentration with the Kovac's reagent, a classic colourimetric assay, and indirectly using a *tnaA*::GFP strain<sup>361</sup>. Also, the use of different carbon sources in a minimal medium will allow us to unveil the role of carbon metabolism in indole synthesis and tryptophanase regulation. Furthermore, I propose to study the natural effect of the indole pulse on the membrane potential of bacteria. I will take advantage of membrane potential fluorescent probes to estimate the membrane potential in the *tnaA*::GFP strain, which allows us to correlate indole production with the membrane voltage.

## **Material and methods**

### **6.1 Indole measurements**

Cultures were grown as described in section 2.2.3. The carbon source was added to fresh M9 for each experiment. For indole measurement, 5  $\mu$ L samples were diluted at 1:10 ratio in PBS, and 100  $\mu$ L Kovacs reagent was added. Briefly, indole reacts with Kovacs's reagent, so the solution turns from yellow to cherry red. The absorbance at 540 nm was measured (Gene Quant 1300, GE Spectrophotometer). The concentration of indole in the supernatant was calculated using a calibration curve. Kovacs reagent was prepared according to Gaimster (75 mL of HCl and 225 mL of amyl alcohol)<sup>331</sup>.

### **6.2 Tna-GFP fluorescent measurement**

Expression of TnaA was measured using the *E. coli* strain *tnaA::GFP:Km<sup>R</sup>*. (see section 2.1.1). This strain has the GFP protein tethered to the tryptophanase, acting as a proxy for indole synthesis<sup>361</sup>. A single colony of *E. coli tnaA::GFP* was inoculated in M9 + 1 g/L glycerol. The following day the bacteria were resuspended in the same fresh medium until turbidity reached an  $OD_{600nm} \sim 0.3 - 0.5$ . Then, they were diluted to  $OD_{600nm} \sim 0.05$  in fresh M9 supplemented with or without tryptophan and the carbon source at the specified concentration in a 96-well plate. The plates were sealed with transparent film permeable to gas "Air-O-Seal" (4titude). Finally, incubation and fluorescence tracking was carried out in a Synergy HTX BioTek. The light source for GFP excitation was a Xenon flash lamp using a  $488 \pm 2$  nm monochromator filter, and emission was recorded at 530/20 nm. Absorbance 600 nm was also recorded.

### **6.3 Membrane potential estimation with Oxonol-VI**

A single colony was inoculated into M9 + 1 g/L glycerol. The next morning the cultures were resuspended in a fresh medium and incubated for 6 h. Then, I added

20  $\mu\text{M}$  Oxonol-VI and grew overnight so that the cultures were fully loaded the next day. The following day, cells were diluted to an  $\text{OD}_{600\text{nm}} \sim 0.05$  units in M9 + 20  $\mu\text{M}$  Oxonol-VI with or without tryptophan and the carbon source at the specified concentration. The fluorophore oxonol-VI emits a fluorescent signal when associated with the bacterial membrane, and its signal is inversely proportional to the cell's membrane potential<sup>421</sup>. Thus, high oxonol-VI fluorescence indicates cell depolarization, and low fluorescence implies hyperpolarisation<sup>421</sup>.

Cells were incubated at 37 °C shaking, and samples were analysed by flow cytometry in a Cytex DxP8 FACScan (Cytex) equipped with a 100 mW 561 nm and 30 mW at 488 nm lasers. For each sample, 50,000 events were recorded at a rate of 5,000-10,000 events per second.

#### **6.4 Measurements of cytoplasmic pH**

For the measurement of the pH, cells were expressing the pSCM001 plasmid<sup>422</sup>, which contains the pHluorin sensor linked to mCherry. The pHluorin sensor is a derived protein from the super-ecliptic GFP<sup>423</sup>, whose fluorescence is proportional to the environmental pH. At the same time, the mCherry is relatively insensitive to changes in pH, so its signal can be used to correct protein expression artefacts. These cells were grown overnight in M9 + 1 g/L glucose. The next day, they were resuspended in a fresh medium until the exponential phase ( $\text{OD}_{600\text{nm}} \sim 0.2$ ). Then, a sample was transferred to a 96-well plate and treated with different indole concentrations for 30 min and immersed in PBS buffered at pH 6. Then, to convert the fluorescence signal into pH, the pHluorin values were calibrated with a standard curve treating the cells with CCCP at different pH (between pH6 to 8.5). Fluorescence was measured in a Synergy HTX BioTek.

For the time-course experiments, cells were grown overnight in M9 + 1 g/L glucose or fumarate. The next day, the cultures were resuspended in a fresh medium and then transferred to a 96-well plate. Then, cells were incubated at 37 °C shaking while fluorescence was measured in a Synergy HTX BioTek.

## Results

### 6.5 Regulation of indole production

#### 6.5.1 Glycolytic flux controls indole production

As described in section 1.5.5.1, glucose represses *tnaA* expression and indole production<sup>361</sup>. Thus, I set to test to what extent other carbon sources affect indole synthesis. For that purpose, I grew *E. coli* in a wide range of gluconeogenic (glycerol, fumarate and acetate) and glycolytic (glucose, gluconate and fructose) carbon sources to investigate this relationship. The results of this experiment confirmed that all glycolytic carbon sources repressed indole synthesis because indole was detected when cells reached the stationary phase (Figure 6.1; left A-C). In contrast, when *E. coli* was fed with gluconeogenic substrates, indole was produced throughout the whole growth process (Figure 6.1; right D-F).

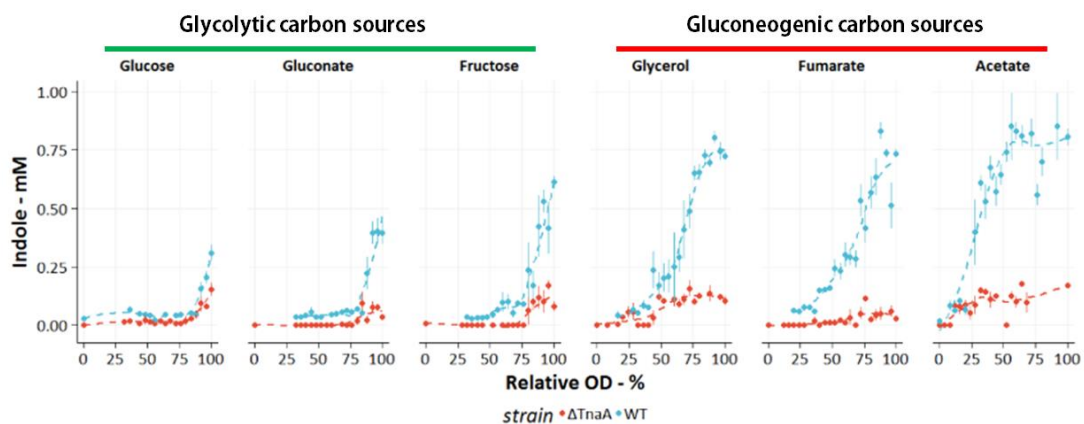
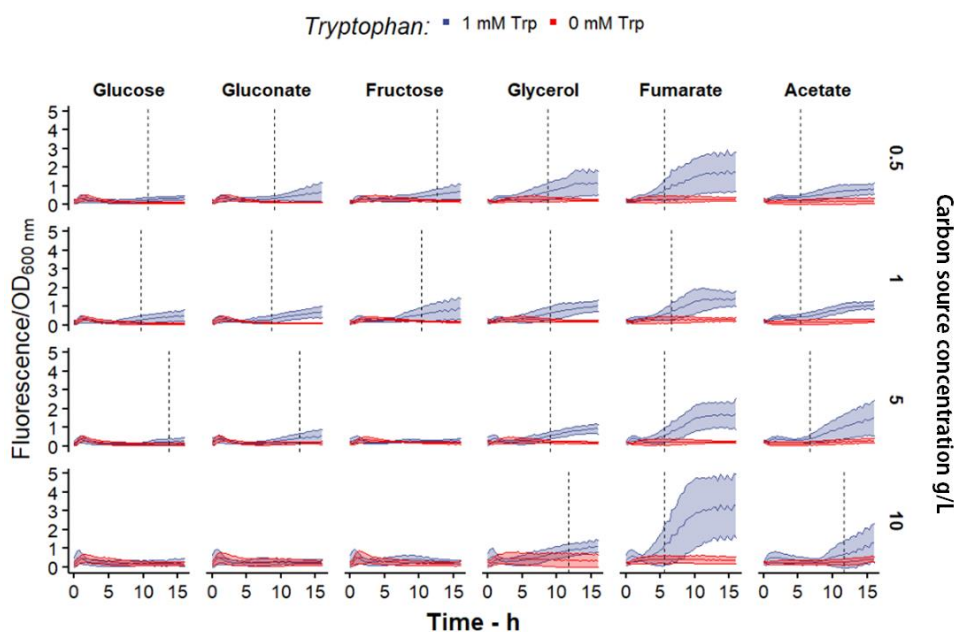


Figure 6.1: Carbon source determines the kinetics of indole synthesis in *E. coli*.

The figure shows the change of indole concentration in relation to the culture biomass. Biomass was estimated using the OD 600 nm, and this value was divided by the maximum OD of each culture condition (100 % OD). Each dot stands for the mean value. The red dots represent the *tnaA* strain, and in blue, the WT. The dashed line shows the smooth regression to aid visualisation. Error bars indicate the standard error. Data represent at least three independent replicates.

### 6.5.2 Indole pulse is regulated via TnaA synthesis

The result of this experiment suggested that the regulation of indole production might occur at the level of TnaA. Consequently, I assessed the kinetics of TnaA expression in *E. coli*, using the chromosomally tag TnaA-GFP reporter strain (described in Gaimster *et al.* 2015<sup>329</sup>) growing on the same carbon sources. Also, I used the presence/absence of tryptophan as negative control<sup>329</sup>. The analysis of this experiment made evident the effect of the carbon source and its concentration on TnaA synthesis (Figure 6.2). Taking as a reference for general TnaA expression the point where the TnaA::GFP signal of the +Trp positive cultures doubles the -Trp baseline (Figure 6.2, dashed line), the data showed a delay in the activation time with an increase in glucose, fructose or gluconate concentration. Interestingly, this expression delay is not present when the cultures are supplied with gluconeogenic carbon sources (Figure 6.2).



**Figure 6.2: The type and concentration of carbon source regulate TnaA synthesis.**

Each panel represents the change in Fluorescence of TnaA-GFP in each carbon source at a determined concentration (right axis). This signal was normalised to OD to compensate for the changes in biomass. The solid line represents the average, and the coloured area stands for the standard error. Data represent at least three independent replicates. The dashed line indicates the earliest time-point when the GFP signal of cultures supplemented with 1 mM differed 2.5-fold of cultures without indole.

## 6.6 Indole regulation on membrane potential

### 6.6.1 TnaA synthesis happens during the entrance of the stationary phase

In line with the previous work<sup>361</sup>, the results presented in section 6.4 show that, while gluconeogenic substrates produce a continuous tryptophanase and indole synthesis, glycolytic carbon sources delay indole synthesis until the entrance to the stationary phase.

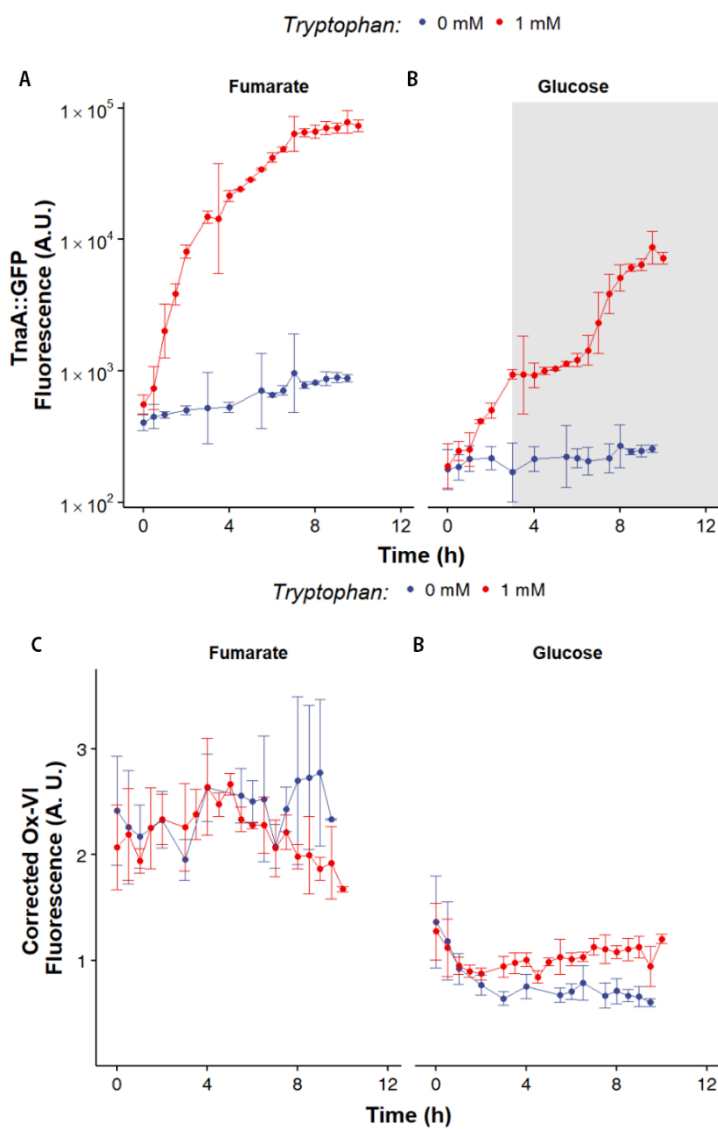


Figure 6.3: TnaA production is correlated with membrane depolarization.

**A, B**) TnaAGFP fluorescence on cultures growing in fumarate (**A**) or glucose (**B**). **C, D**) Oxonol-VI signal corrected by FCS of cultures growing in fumarate (**C**) or glucose (**D**). Each dot represents the geometric average of three biological replicates. Error bars indicate the standard deviation of the six independent replicates. The red colour indicates cultures supplemented with tryptophan, and the blue colour stands for cultures without tryptophan. The grey rectangle marks the entrance in the exponential phase and the stationary phase. The beginning of the stationary phase was estimated based on previous experiments.

Since indole is a known protonophore<sup>330</sup>, I examined whether it could modulate bacterial membrane potential. Thus, I employed the fluorescent voltage probe Oxonol-VI (OxVI) to simultaneously monitor membrane potential and indole production using the *E. coli* TnaA::GFP reporter strain (**Figure 6.3**). OxVI uptake and fluorescence increase with membrane depolarisation<sup>421</sup>, but the proportion of the signal originating in the outer versus the inner membrane remains unclear.

I cultured the bacteria in fumarate or glucose in the presence or absence of tryptophan as a control for indole production. Flow cytometry analysis confirmed that using fumarate as the sole carbon source induces a constant TnaA synthesis, while in glucose, TnaA production was delayed until the stationary phase entrance (**Figure 6.3**, panels **A** and **B**). When I looked at the signal from the membrane potential reporter, I could see that fumarate cells have a stronger Oxonol-VI (**Figure 6.3**, panels **C** and **D**) than glucose, but I did not see a difference in OxVI signal between the presence or absence of tryptophan for the fumarate condition. In contrast, the cells growing on glucose showed a shift when tryptophan was available (**Figure 6.3D**; linear mixed model p-value < 0.001).

### **6.6.2 Indole causes a proton leak**

Previous research has shown that the ability to produce indole was a determinant factor for the cytoplasmic pH of bacteria<sup>329</sup>. Thus, I set to investigate the effect of indole addition on the cytoplasmic pH. For that purpose, I grew cells expressing pHluorin (plasmid pSCM001, see section 2.3.2) in order to measure cytoplasmic pH. When the cultures reached the exponential phase, I treated the cells with different indole concentrations and measured the pHluorin signal. Here I found

that immersing the cells in an acid buffer (pH 6) in the presence of indole leads to a decrease of cytoplasmic pH (1.5 pH units, from pH 8 to pH 7.5, **Figure 6.4B**). Consistently with my previous findings (see section 4.5.2), in the absence of indole, cells had a robust buffering capacity for the cytoplasmic pH. Comparing the presence and absence of indole showed a statistically significant effect on pH (**Figure 6.4C**).

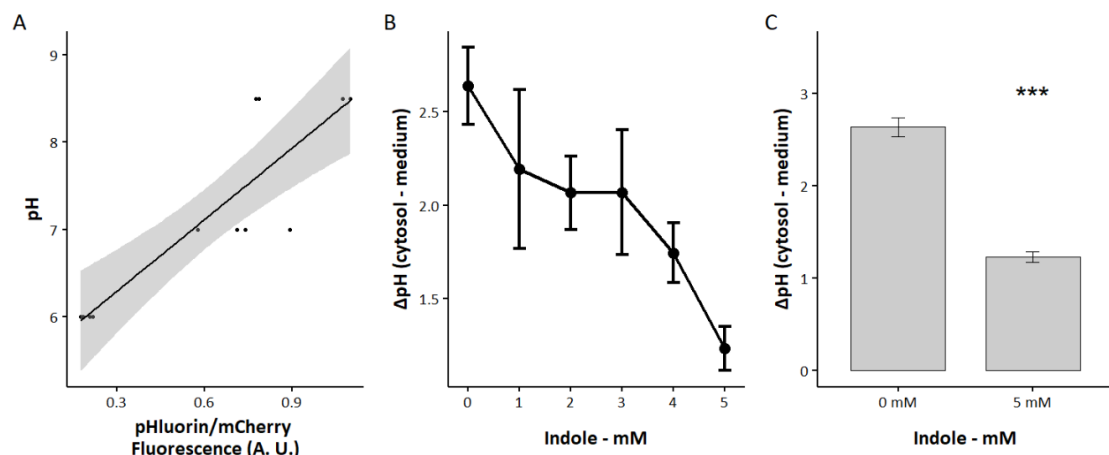


**Figure 6.4: The addition of indole allows protons to cross the bacterial membrane.**

Cells were grown in M9 + 1 g/L glucose to exponential phase. Then, a sample was treated with different indole concentrations for 30 min and immersed in PBS buffered at pH 6. Then, to convert the fluorescence signal into pH, the pHluorin values were calibrated with a standard curve treating the cells with CCCP at different pH. **A)** Calibration curve. **B)** Decrease in cytoplasmic pH with the addition of indole. Since the medium was buffered at a lower pH (pH 6), the addition of indole permeabilises the membrane to protons, thus acidifying the cytoplasm. The shaded area indicates the standard error. **C)** Statistical comparison between no indole or 5 mM indole. Error bar denotes the standard error. The statistical confirmation was done with a T-test, and three stars denote p-value <0.001.

### 6.6.3 The strain $\Delta tnaA$ has a higher pH than WT

After showing the effect of indole treatment on cytoplasmic pH, I aimed to investigate the role of indole in the physiology of growing cells. For that purpose, I grew cells expressing the pHluorin sensor in different carbon sources and then compared their cytoplasmic pH. Here, I found that independently of the carbon source, the  $\Delta tnaA$  strain always presented a higher cytoplasmic pH compared to WT, that is, pH 8.25 for  $\Delta tnaA$  vs pH 7.5 WT when growing in fumarate (see **Figure**

6.5A) and pH 7.8 for  $\Delta tnaA$  vs pH 7.3 WT when growing in glucose (see Figure 6.5B), suggesting a role of indole in setting the basal cytoplasmic pH level *in vivo*.

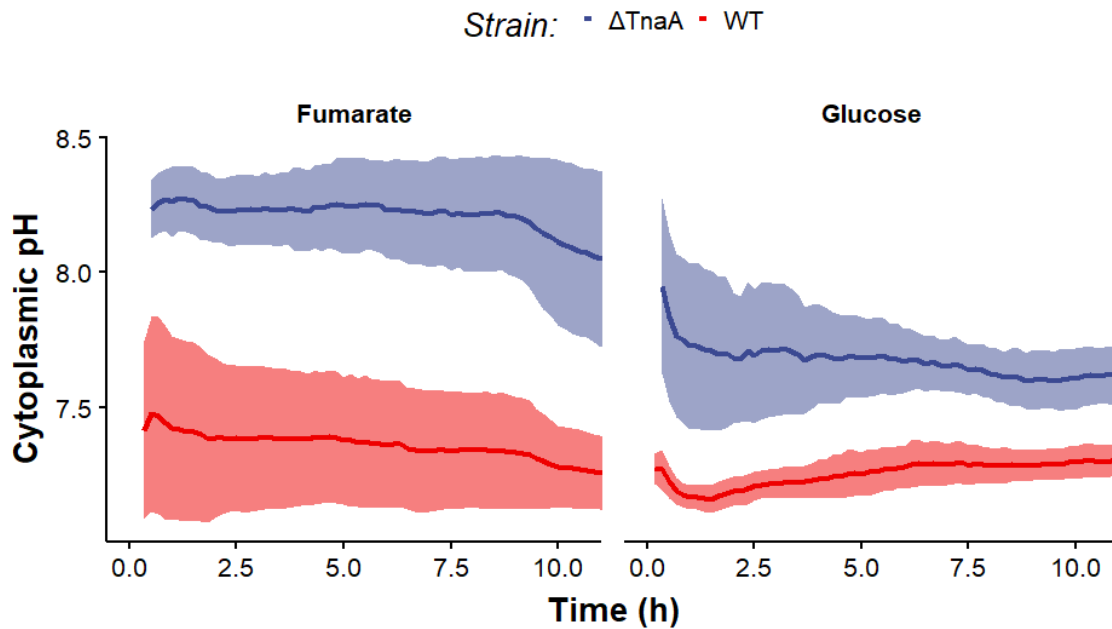


Figure 6.5: The  $\Delta tnaA$  has a higher pH than WT

Cells were grown in M9 + 1 g/L glucose/ + 1 mM tryptophan in a 96-well plate setup where fluorescence was monitored over time. Then, to convert the fluorescence signal into pH, the pHluorin values were calibrated with a standard curve treating the cells with CCCP at different pH. The WT (red) has lower pH than  $\Delta tnaA$  (blue).

## **Discussion and conclusion**

In this chapter, I have presented an overview of indole signalling regulation and its effects on bacterial electrophysiology. These experiments were done at the beginning of my thesis. Having developed a suite of fluorescent reporters to examine internal ion concentrations and inner membrane voltage changes, I would have been very keen (given more research time) to revisit the effects on Indole using more robust methods. Particularly, I think taking advantage of the mother machine could have vastly helped us in this research project. This platform, in combination with the TnaA-GFP strain and the QuasAr2 sensor, corroborates at the single-cell level the impact of TnaA synthesis on the membrane potential.

### **6.7 Regulation of indole synthesis**

I have provided evidence that specific carbon sources control indole synthesis. These results are consistent with the broader literature as it is well established that indole production is repressed in the presence of glucose<sup>338,341</sup>. Here I extend the current understanding of indole production, showing how gluconeogenic carbon sources produce a constant indole production as long as tryptophan is present in the medium. A further investigation of this question would require an understanding of the two main promoters of the *tna* operon: CRP and TorR. If gluconeogenic carbon sources induce *tna* due to a low glycolytic flux, then a knockout of CRP should remove indole production even when bacteria grow on fumarate. If, however, gluconeogenic carbon sources increase alkaline stress, then a  $\Delta$ *torR* strain should show a significant decrease in indole production. Finally, a combination of both effects could be tested with a double KO.

## 6.8 Indole effect on membrane potential

Previous works have demonstrated that treatment with high indole concentration produces membrane depolarisation<sup>330</sup>. In addition, it also has been reported that such high concentrations are indeed achievable physiologically through intense indole synthesis during the so-called 'indole pulse'. However, the effect of this indole pulse has not been studied during planktonic growth.

My results indicate that cells growing in fumarate produce constant indole and produce a stronger Oxonol-VI signal, which is inversely correlated to membrane potential and is thought to represent membrane depolarization. This phenotype is also present in cells growing without tryptophan and is therefore indole-independent. Nevertheless, when I look at cells growing on glucose, I can see that the Oxonol-VI signal decreases as cells during the initial stages of the exponential phase but start to increase along with the TnaA::GFP signal. Consistently, this change does not occur in the absence of tryptophan, which suggests that TnaA synthesis and indole production drives the change in membrane potential. An important drawback of this approach emerges from the fact that oxonol-VI fluorescence depends on two factors: fluorophore uptake and membrane voltage. Indeed, this artefact is common to all chemical probes to measure membrane potential. For example, already in 1999, the studies of the membrane potential with the Rhodamine 123, DiOC<sub>2</sub>(3), oxonol dye DiBAC<sub>1</sub>(3) showed that the fluorescent signal was affected by the cell size and permeability of *Staphylococcus aureus*<sup>424,425</sup>. Indeed, this artefact was the motivation for the development of ratiometric sensors such as DiOC<sub>2</sub>(3) that provide a signal proportional to the membrane potential along with an independent signal proportional to the fluorophore abundance<sup>425</sup>. The lack of this reference signal for the reporters tested here could explain why membrane potential measurements with ThT and OxVI are so diverse.

## Chapter 6: Indole production regulates membrane potential

On top of that, both membranes could potentially influence the signal from this voltage reporter. Therefore, I think that using a genetically encoded membrane potential reporter could help resolve these problems. In addition, with the methods I have developed, I could (given more research time) now directly measure periplasmic pH (using my periplasmic reporter pelBC::pHuji).

It is clear that the work presented in this chapter is preliminary. Therefore, a more rigorous analysis of the potential role of indole should include (i) physiological regulation of membrane voltage (and how it influences porin permeability in light of the other regulatory mechanisms described in Chapters 3, 4, and 5); and (ii) whether indole could influence macrophage phagosomal or cellular membrane voltage and thereby disrupt host immunity.

# **Chapter 7: GENERAL DISCUSSION AND CONCLUSION**

## **Discussion**

In this project, I have explored how the periplasmic ionic environment of *E. coli* might regulate porin permeability. I have linked dynamics changes in periplasmic ions to the carbon metabolism integrating all my findings into a model to explain the control of porin permeability. I validated my model by looking at permeability to the antibiotic ciprofloxacin confirming the potential clinical relevance of my findings. Finally, I studied the dynamics of the physiological regulator of membrane potential indole, showing how carbon metabolism might regulate it and lead to changes in membrane potential.

### **7.1 Regulation of porin permeability by periplasmic ions**

Despite long-standing research on the effects of ions in porin conductivity and permeability<sup>66,335</sup>, the relevance for this phenomenon in living organisms remains insufficient. The results reported in this thesis provide the first convincing evidence that intracellular periplasmic ions drive bacterial permeability *in vivo*, which could explain how bacteria can build a proton motive force despite having a large number of porins on the outer membrane.

I deployed a combined approach measuring the accumulation of fluorescent compounds with flow cytometry and monitoring single-cell uptake in real-time with the Mother Machine microfluidics system. The impact of internal potassium and hydrogen in the uptake of fluorescent tracers suggest potential regulation of porins through internal ions. In addition, my data suggest that the OmpC porin is largely responsible for the effects of internal potassium. This evidence is also supported in the findings of Kojima *et al.*, who used a totally independent method<sup>102</sup>.

I then developed an independent method to modulate periplasmic pH at the single-cell level, adapting a genetically encoded light-activated proton pump, ArchT. Measurements of fluorescent markers with the cells expressing ArchT within a microfluidic device indicated that periplasmic acidification blocks porin permeability.

I also provide computational support through molecular dynamic simulation that the porin aperture might be regulated by the protonation of residues located at the periplasmic side. In line with the experimental results, these simulations suggest that increased protonation decreases porin diameter. Although advanced methods could increase the precision of the simulation, exploring that option was beyond the scope of my research. Reconstituting porins in lipid vesicles with different pH inside and out could produce definitive evidence for intrinsic regulation of porin permeability by ion interaction.

Whilst the data presented in this work indicate that internal ions modulate porin permeability, there are some potential issues with the methodology that could introduce artefacts in our measurements. First, the greater part of this work was done with 2NBDG, which accumulates in the cytoplasm. Thus it is perfectly possible that the experiment confounded changes in the permeability of the inner membrane with the outer membrane. This issue should be easily solved by repeating some of the measurements with the fluorescent penicillin analogue BFL. In addition, it could be the case that the ionic modulation of porins is intrinsic to the particular porins of *E. coli* studied in this work. This idea is supported by the fact that different porins have indeed different ion selectivity<sup>66</sup>. Also, several studies have shown that changing certain amino acids in the porin sequence causes significant changes in the permeability and selectivity of the porin<sup>66</sup>. Further studies of porins in other Gram-negatives such as *Pseudomonas* or in other non-Gram-negatives like *Mycobacterial* species would provide even more robust evidence for a generalisation of porin control through ionic changes. It is also

interesting to ask whether this ion regulation of porins could occur in the mitochondrion's porin-like proteins.

One reason why similar effects in all double-membrane organisms should be expected is that this mechanism explains how double-membrane bacteria can build an ion gradient when they have open pores on the outer membrane. If these pores are always open, when the electron transport chain pumps protons to the inter-membrane space, they should theoretically leak out. My work provides evidence of ion regulation of bacterial porins that would preserve the proton motive force as much as possible and potentially limit ROS production through the back reaction of Complex I. Whilst a possible explanation could be that porins and the electron transport chain cluster around different areas of the membrane (e. g. accumulating on different poles), studies covering the localisation of *E. coli*'s proteome suggest the opposite<sup>426</sup>. That is, most of the electron transport chain and Krebs' cycle-related proteins are located in the membrane poles, which is the same area around which transporters are located<sup>426</sup>. Nevertheless, the open question is, how can gram-positives generate a proton gradient with only one membrane?

## **7.2 Periplasmic ion isolation**

The results presented in this thesis represent the first step in understanding periplasmic ion dynamics in *E. coli*. I adapted a genetically encoded pH sensor to accurately monitor periplasmic pH for the first time. This experiment revealed that the ionic periplasmic environment is partially isolated from the external medium and this isolation allowed the emergence of proton spikes. Although the buffering capacity was not absolute, these results are very important in the light of the general thesis because it clearly shows that the proton concentration of the periplasm can fluctuate independently of the external medium and the cytoplasm.

Although I tried to develop a reporter for periplasmic potassium based on the GINKO1 reporter, I noticed that the fluorescent sensors for this ion were not stable in the cytoplasm. This problem was likely due to the instability of GFP in the periplasmic environment<sup>404</sup>. Future designs should take this into account. For example, new genetically encoded potassium sensors have been already explored<sup>427</sup> using GINKO1 as a template but changing the K-binding region. It would then make sense to integrate the K-binding region in other fluorescent proteins that could be resistant to periplasmic conditions. This combination would allow having a fluorescent potassium sensor for the periplasm compartment. This tool would be precious because I observed that the cytoplasmic K<sup>+</sup> was not fully permeabilised with the valinomycin treatment.

### **7.3 Carbon source drives ion oscillations**

Looking at the dynamics of individual ions in the cytoplasm and the periplasmic pH, I noticed that the potassium and hydrogen ions were highly dynamic. My results suggest that one of the underlying forces behind these spikes is carbon metabolism, partly mediated by the voltage-activated potassium channel Kch. This observation was also supported by the increase in membrane potential spikes with the increase in glucose. Also, the use of ionophores and the chemical disruption of the ATPase with oligomycin caused a clear impact on the membrane potential baseline, strongly suggesting the participation of the electron transport chain.

Moreover, I found that the Kch channel contributes to setting the basal membrane potential through changes in the periplasmic pH. Nevertheless, I was unable to assess its impact on potassium levels. As mentioned above, this could be solved with the periplasmic potassium sensor.

The correlation between the carbon source and the changes in periplasmic ions led us to theorize that carbon sources could mediate membrane permeability.

Interestingly, I found that extreme conditions such as starvation and the high availability of carbon sources increased membrane permeability.

It would be compelling to study the relationship between metabolism and cell division because of its potential relevance to pathology. It has been proposed that one of the survival mechanisms of bacteria during the infection process or trapped within the macrophage phagosome is to enter a state of dormancy<sup>428,429</sup>. Therefore, I would expect different oscillatory frequencies for dormant bacteria versus growing bacteria.

#### **7.4 Carbon metabolism drives ciprofloxacin uptake**

In order to test this permeability model, I studied the uptake of ciprofloxacin. Single-cell fluorescent analysis of ciprofloxacin uptake revealed how carbon sources might mediate the permeability of ciprofloxacin. One possible explanation for this phenomenon is that the grown on different carbon sources causes a differential expression in porins, which modulates cell permeability. However, I showed that combining the use of proton ionophores and different pH I could revert the permeability phenotype, suggesting that the periplasmic ionic environment indeed mediates the carbon source effect. Still, this method presents the same kind of bias discussed in section 7.1, particularly because it is known that pH changes alter quinolones permeability<sup>416</sup>. Thus, experiments with ArchT and the uptake of quinolones might help to resolve this confounder.

In addition, I found that the deletion of the Kch channel also impaired ciprofloxacin uptake. A detailed study of this strain showed that this phenotype is modulated by the carbon source concentration, in accordance with the model proposed in this work. Nevertheless, measuring ciprofloxacin as a proxy for permeability presents the same bias that glucose analogues. This compound tends to accumulate in the

cytoplasm. This cytoplasmic accumulation means that easy to mistake changes in permeability in the outer membrane with the inner membrane. Here, I think fluorescent penicillin markers as a proxy for outer membrane permeability could help further clarify this question.

I then tried to translate the effect of carbon source in permeability to antibiotic efficacy. As expected, the data showed that the deletion of major porins or the Kch was associated with increased ciprofloxacin resistance. The use of different carbon sources causes leads to large differences in the antibiotic susceptibility of *E. coli*. In line with this evidence, growing metabolic knock out strains with impaired glucose or lipid pathways in mixed media showed that the strains utilising glucose always had higher susceptibility to ciprofloxacin.

Overall, this work has shown that carbon source affects not only permeability but also antibiotic susceptibility. A potential area of research could be looking for combined therapies targeting periplasmic ions, improving the uptake of antibiotics. The clear drawback of this method is that most ion modulators also affect eukaryotic cells. Therefore, a more reasonable approach could be targeting the Kch channel or the electron transport chain itself.

## **7.5 Regulation of indole and membrane potential**

The results presented in this chapter potentially helped to generalise our understanding of the regulation of indole production. Using several carbon sources, I showed that indole production at the stationary phase entrance is likely regulated by the glycolytic flux. In addition, I show that cells growing on gluconeogenic carbon sources present a very different profile for indole production.

Moreover, I also attempt to show how indole production affects the membrane potential in live cells. Although my findings were not conclusive, they pointed to

an important disadvantage in using chemical probes as membrane potential reporters.

However, my data clearly indicate that indole acts as an ionophore. This result was confirmed by measuring the change in cytosolic pH with the addition of indole. In addition, I also showed how growing cells have a different cytoplasmic pH depending on their ability to produce indole.

Future work is necessary to define the precise role of indole production and its impact on bacterial membrane permeability and host immunity.



# **Chapter 8: APPENDIX AND REFERENCES**

## References

1. Cavalier-Smith, T. A revised six-kingdom system of life. *Biol. Rev.* **73**, 203–266 (1998).
2. Curtis, T. P., Sloan, W. T. & Scannell, J. W. Estimating prokaryotic diversity and its limits. *Proc. Natl. Acad. Sci.* **99**, 10494–10499 (2002).
3. Schloss, P. D. & Handelsman, J. Status of the Microbial Census. *Microbiol. Mol. Biol. Rev.* **68**, 686–691 (2004).
4. Giovannoni, S. J., Cameron Thrash, J. & Temperton, B. Implications of streamlining theory for microbial ecology. *ISME J.* **8**, 1553–1565 (2014).
5. Egan, A. J. F., Errington, J. & Vollmer, W. Regulation of peptidoglycan synthesis and remodelling. *Nat. Rev. Microbiol.* **18**, 446–460 (2020).
6. Muñoz-Gómez, S. A. & Roger, A. J. Leaving negative ancestors behind. *eLife* **5**, e20061 (2016).
7. Gram, H. C. J. & Friedlaender, C. *Ueber die isolirte Färbung der Schizomyceten: in Schnitt-und Trockenpräparaten.* (Theodor Fischer's medicinischer Buchhandlung, 1884).
8. Tocheva, E. I., Ortega, D. R. & Jensen, G. J. Sporulation, bacterial cell envelopes and the origin of life. *Nat. Rev. Microbiol.* **14**, 535–542 (2016).
9. *Brock biology of microorganisms.* (Benjamin Cummings, 2012).
10. Stackebrandt, E., Murray, R. G. E. & Trüper, H. G. Y. 1988. Proteobacteria classis nov., a Name for the Phylogenetic Taxon That Includes the “Purple Bacteria and Their Relatives”. *Int. J. Syst. Evol. Microbiol.* **38**, 321–325.
11. Blount, Z. D. The unexhausted potential of *E. coli*. *eLife* **4**, e05826 (2015).
12. Crick, F. H. C., Barnett, L., Brenner, S. & Watts-Tobin, R. J. General Nature of the Genetic Code for Proteins. *Nature* **192**, 1227–1232 (1961).
13. Nirenberg, M. *et al.* RNA codewords and protein synthesis, VII. On the general nature of the RNA code. *Proc. Natl. Acad. Sci.* **53**, 1161–1168 (1965).
14. Judson, H. F. *The Eighth Day of Creation: Makers of the Revolution in Biology.* (1979).
15. Hartl, D. L. & Dykhuizen, D. E. The Population Genetics of *Escherichia Coli*. *Annu. Rev. Genet.* **18**, 31–68 (1984).
16. Leimbach, A., Hacker, J. & Dobrindt, U. *E. coli* as an All-Rounder: The Thin Line Between Commensalism and Pathogenicity. in *Between Pathogenicity and Commensalism* (eds. Dobrindt, U., Hacker, J. H. & Svanborg, C.) 3–32 (Springer, 2013). doi:10.1007/82\_2012\_303.
17. Megrian, D., Taib, N., Witwinowski, J., Beloin, C. & Gribaldo, S. One or two membranes? Diderm Firmicutes challenge the Gram-positive/Gram-negative divide. *Mol. Microbiol.* **113**, 659–671 (2020).
18. Konovalova, A., Kahne, D. E. & Silhavy, T. J. Outer Membrane Biogenesis. *Annu. Rev. Microbiol.* **71**, 539–556 (2017).
19. Clifton, L. A. *et al.* Effect of Divalent Cation Removal on the Structure of Gram-Negative Bacterial Outer Membrane Models. *Langmuir* **31**, 404–412 (2015).
20. Whitfield, C. & Trent, M. S. Biosynthesis and Export of Bacterial Lipopolysaccharides. *Annu. Rev. Biochem.* **83**, 99–128 (2014).
21. Simpson, B. W. & Trent, M. S. Pushing the envelope: LPS modifications and their consequences. *Nat. Rev. Microbiol.* **17**, 403–416 (2019).

22. Bertani, B. & Ruiz, N. Function and biogenesis of lipopolysaccharides. *EcoSal Plus* **8**, (2018).
23. May, K. L. & Grabowicz, M. The bacterial outer membrane is an evolving antibiotic barrier. *Proc. Natl. Acad. Sci.* **115**, 8852–8854 (2018).
24. Ma, H., Irudayanathan, F. J., Jiang, W. & Nangia, S. Simulating Gram-Negative Bacterial Outer Membrane: A Coarse Grain Model. *J. Phys. Chem. B* **119**, 14668–14682 (2015).
25. Nikaido, H. Porins and specific channels of bacterial outer membranes. *Mol. Microbiol.* **6**, 435–442 (1992).
26. Nikaido, H. Molecular Basis of Bacterial Outer Membrane Permeability Revisited. *Microbiol. Mol. Biol. Rev.* **67**, 593–656 (2003).
27. Taib, N. *et al.* Genome-wide analysis of the Firmicutes illuminates the diderm/monoderm transition. *Nat. Ecol. Evol.* **4**, 1661–1672 (2020).
28. Lake, J. A., Servin, J. A., Herbold, C. W. & Skophammer, R. G. Evidence for a New Root of the Tree of Life. *Syst. Biol.* **57**, 835–843 (2008).
29. Lake, J. A. Evidence for an early prokaryotic endosymbiosis. *Nature* **460**, 967–971 (2009).
30. Gupta, R. S. Origin of diderm (Gram-negative) bacteria: antibiotic selection pressure rather than endosymbiosis likely led to the evolution of bacterial cells with two membranes. *Antonie Van Leeuwenhoek* **100**, 171–182 (2011).
31. von Dohlen, C. D., Kohler, S., Alsop, S. T. & McManus, W. R. Mealybug  $\beta$ -proteobacterial endosymbionts contain  $\gamma$ -proteobacterial symbionts. *Nature* **412**, 433–436 (2001).
32. Thao, M. L., Gullan, P. J. & Baumann, P. Secondary ( $\gamma$ -Proteobacteria) Endosymbionts Infect the Primary ( $\beta$ -Proteobacteria) Endosymbionts of Mealybugs Multiple Times and Coevolve with Their Hosts. *Appl. Environ. Microbiol.* **68**, 3190–3197 (2002).
33. Gupta, R. S. Protein Phylogenies and Signature Sequences: A Reappraisal of Evolutionary Relationships among Archaeobacteria, Eubacteria, and Eukaryotes. *Microbiol. Mol. Biol. Rev.* **62**, 1435–1491 (1998).
34. Vollmer, W. Bacterial outer membrane evolution via sporulation? *Nat. Chem. Biol.* **8**, 14–18 (2012).
35. Errington, J. L-form bacteria, cell walls and the origins of life. *Open Biol.* **3**, 120143 (2013).
36. Sutcliffe, I. C. A phylum level perspective on bacterial cell envelope architecture. *Trends Microbiol.* **18**, 464–470 (2010).
37. Gupta, R. S. & Golding, G. B. Evolution of HSP70 gene and its implications regarding relationships between archaeobacteria, eubacteria, and eukaryotes. *J. Mol. Evol.* **37**, 573–582 (1993).
38. Remmert, M., Biegert, A., Linke, D., Lupas, A. N. & Söding, J. Evolution of Outer Membrane  $\beta$ -Barrels from an Ancestral  $\beta\beta$  Hairpin. *Mol. Biol. Evol.* **27**, 1348–1358 (2010).
39. Tocheva, E. I. *et al.* Peptidoglycan Remodeling and Conversion of an Inner Membrane into an Outer Membrane during Sporulation. *Cell* **146**, 799–812 (2011).
40. Vincent, A. T. *et al.* The Mycobacterial Cell Envelope: A Relict From the Past or the Result of Recent Evolution? *Front. Microbiol.* **9**, 2341 (2018).

41. Ferreira, R. J. & Kasson, P. M. Antibiotic Uptake Across Gram-Negative Outer Membranes: Better Predictions Towards Better Antibiotics. *ACS Infect. Dis.* **5**, 2096–2104 (2019).
42. Martinez, M. B., Flickinger, M., Higgins, L., Krick, T. & Nelsestuen, G. L. Reduced Outer Membrane Permeability of *Escherichia coli* O157:H7: Suggested Role of Modified Outer Membrane Porins and Theoretical Function in Resistance to Antimicrobial Agents. *Biochemistry* **40**, 11965–11974 (2001).
43. Pagès, J.-M., James, C. E. & Winterhalter, M. The porin and the permeating antibiotic: a selective diffusion barrier in Gram-negative bacteria. *Nat. Rev. Microbiol.* **6**, 893–903 (2008).
44. Lou, H. *et al.* Altered Antibiotic Transport in *OmpC* Mutants Isolated from a Series of Clinical Strains of Multi-Drug Resistant *E. coli*. *PLOS ONE* **6**, e25825 (2011).
45. Fernández, L. & Hancock, R. E. W. Adaptive and Mutational Resistance: Role of Porins and Efflux Pumps in Drug Resistance. *Clin. Microbiol. Rev.* **25**, 661–681 (2012).
46. Fajardo-Lubián, A., Zakour, N. L. B., Agyekum, A., Qi, Q. & Iredell, J. R. Host adaptation and convergent evolution increases antibiotic resistance without loss of virulence in a major human pathogen. *PLOS Pathog.* **15**, e1007218 (2019).
47. Braun, V. FhuA (TonA), the Career of a Protein. *J. Bacteriol.* **191**, 3431–3436 (2009).
48. Ekiert, D. C. *et al.* Architectures of Lipid Transport Systems for the Bacterial Outer Membrane. *Cell* **169**, 273–285.e17 (2017).
49. Jacques, M. Role of lipo-oligosaccharides and lipopolysaccharides in bacterial adherence. *Trends Microbiol.* **4**, 408–410 (1996).
50. Genevaux, P., Bauda, P., DuBow, M. S. & Oudega, B. Identification of Tn10 insertions in the *rfaG*, *rfaP*, and *galU* genes involved in lipopolysaccharide core biosynthesis that affect *Escherichia coli* adhesion. *Arch. Microbiol.* **172**, 1–8 (1999).
51. Nesper, J. *et al.* Role of *Vibrio cholerae* O139 Surface Polysaccharides in Intestinal Colonization. *Infect. Immun.* **70**, 5990–5996 (2002).
52. Petersson, J. *et al.* Importance and regulation of the colonic mucus barrier in a mouse model of colitis. *Am. J. Physiol. - Gastrointest. Liver Physiol.* **300**, G327–G333 (2011).
53. Kim, J. K. *et al.* The lipopolysaccharide core oligosaccharide of *Burkholderia* plays a critical role in maintaining a proper gut symbiosis with the bean bug *Riptortus pedestris*. *J. Biol. Chem.* **292**, 19226–19237 (2017).
54. Mathis, R. *et al.* Lipopolysaccharides as a communication signal for progression of legume endosymbiosis. *Proc. Natl. Acad. Sci.* **102**, 2655–2660 (2005).
55. Lee, K.-J., Lee, M.-A., Hwang, W., Park, H. & Lee, K.-H. Deacylated lipopolysaccharides inhibit biofilm formation by Gram-negative bacteria. *Biofouling* **32**, 711–723 (2016).
56. Chalabaev, S. *et al.* Biofilms Formed by Gram-Negative Bacteria Undergo Increased Lipid A Palmitoylation, Enhancing In Vivo Survival. *mBio* **5**, (2014).
57. Murphy, K. *et al.* Influence of O Polysaccharides on Biofilm Development and Outer Membrane Vesicle Biogenesis in *Pseudomonas aeruginosa* PAO1. *J. Bacteriol.* **196**, 1306–1317 (2014).
58. Lu, Q., Wang, J., Faghihnejad, A., Zeng, H. & Liu, Y. Understanding the molecular interactions of lipopolysaccharides during *E. coli* initial adhesion with a surface forces apparatus. *Soft Matter* **7**, 9366–9379 (2011).

59. Alshalchi, S. A. & Anderson, G. G. Expression of the lipopolysaccharide biosynthesis gene *lpxD* affects biofilm formation of *Pseudomonas aeruginosa*. *Arch. Microbiol.* **197**, 135–145 (2015).
60. Graham, L. L., Beveridge, T. J. & Nanninga, N. Periplasmic space and the concept of the periplasm. *Trends Biochem. Sci.* **16**, 328–329 (1991).
61. Willey, J. M., Sherwood, L., Woolverton, C. J. & Prescott, L. M. *Prescott, Harley, and Klein's microbiology*. (McGraw-Hill Higher Education, 2008).
62. Vollmer, W., Blanot, D. & De Pedro, M. A. Peptidoglycan structure and architecture. *FEMS Microbiol. Rev.* **32**, 149–167 (2008).
63. Miller, S. I. & Salama, N. R. The gram-negative bacterial periplasm: Size matters. *PLOS Biol.* **16**, e2004935 (2018).
64. Niederweis, M., Danilchanka, O., Huff, J., Hoffmann, C. & Engelhardt, H. Mycobacterial outer membranes: in search of proteins. *Trends Microbiol.* **18**, 109–116 (2010).
65. Rosenbusch, J. P. Characterization of the Major Envelope Protein from *Escherichia coli*: REGULAR ARRANGEMENT ON THE PEPTIDOGLYCAN AND UNUSUAL DODECYL SULFATE BINDING. *J. Biol. Chem.* **249**, 8019–8029 (1974).
66. Electrophysiology of unconventional channels and pores. (Springer, 2015).
67. Schirmer, T., Keller, T., Wang, Y. & Rosenbusch, J. Structural basis for sugar translocation through maltoporin channels at 3.1 Å resolution. *Science* **267**, 512–514 (1995).
68. Liang, B. & Tamm, L. K. Structure of outer membrane protein G by solution NMR spectroscopy. *Proc. Natl. Acad. Sci. U. S. A.* **104**, 16140–16145 (2007).
69. Zeth, K. & Thein, M. Porins in prokaryotes and eukaryotes: common themes and variations. *Biochem. J.* **431**, 13–22 (2010).
70. Arunmanee, W. *et al.* Gram-negative trimeric porins have specific LPS binding sites that are essential for porin biogenesis. *Proc. Natl. Acad. Sci. U. S. A.* **113**, E5034–5043 (2016).
71. Prajapati, J. D., Kleinekathöfer, U. & Winterhalter, M. How to Enter a Bacterium: Bacterial Porins and the Permeation of Antibiotics. *Chem. Rev.* **121**, 5158–5192 (2021).
72. Vergalli, J. *et al.* Porins and small-molecule translocation across the outer membrane of Gram-negative bacteria. *Nat. Rev. Microbiol.* **18**, 164–176 (2020).
73. Schulz, G. E. beta-Barrel membrane proteins. *Curr. Opin. Struct. Biol.* **10**, 443–447 (2000).
74. Koebnik, R., Locher, K. P. & Gelder, P. V. Structure and function of bacterial outer membrane proteins: barrels in a nutshell. *Mol. Microbiol.* **37**, 239–253 (2000).
75. Wang, Y.-F., Dutzler, R., Rizkallah, P. J., Rosenbusch, J. P. & Schirmer, T. Channel specificity: structural basis for sugar discrimination and differential flux rates in maltoporin<sup>11</sup> Edited by R. Huber. *J. Mol. Biol.* **272**, 56–63 (1997).
76. Cowan, S. W. *et al.* Crystal structures explain functional properties of two *E. coli* porins. *Nature* **358**, 727–733 (1992).
77. Baslé, A., Rummel, G., Storici, P., Rosenbusch, J. P. & Schirmer, T. Crystal Structure of Osmoporin OmpC from *E. coli* at 2.0 Å. *J. Mol. Biol.* **362**, 933–942 (2006).
78. Dhakshnamoorthy, B., Raychaudhury, S., Blachowicz, L. & Roux, B. Cation selective pathway of OmpF porin revealed by anomalous X-ray diffraction. *J. Mol. Biol.* **396**, 293–300 (2010).

79. Biró, I., Pezeshki, S., Weingart, H., Winterhalter, M. & Kleinekathöfer, U. Comparing the Temperature-Dependent Conductance of the Two Structurally Similar *E. coli* Porins OmpC and OmpF. *Biophys. J.* **98**, 1830–1839 (2010).
80. Korteland, J., Tommassen, J. & Lugtenberg, B. PhoE protein pore of the outer membrane of *Escherichia coli* K12 is a particularly efficient channel for organic and inorganic phosphate. *Biochim. Biophys. Acta BBA - Biomembr.* **690**, 282–289 (1982).
81. Schulz, G. E. The structure of bacterial outer membrane proteins. *Biochim. Biophys. Acta BBA - Biomembr.* **1565**, 308–317 (2002).
82. Yamashita, E., Zhalnina, M. V., Zakharov, S. D., Sharma, O. & Cramer, W. A. Crystal structures of the OmpF porin: function in a colicin translocon. *EMBO J.* **27**, 2171–2180 (2008).
83. Alcaraz, A., Nestorovich, E. M., Aguilera-Arzo, M., Aguilera, V. M. & Bezrukov, S. M. Salting Out the Ionic Selectivity of a Wide Channel: The Asymmetry of OmpF. *Biophys. J.* **87**, 943–957 (2004).
84. Nestorovich, E. M., Rostovtseva, T. K. & Bezrukov, S. M. Residue Ionization and Ion Transport through OmpF Channels. *Biophys. J.* **85**, 3718–3729 (2003).
85. Pezeshki, S., Chimere, C., Bessonov, A. N., Winterhalter, M. & Kleinekathöfer, U. Understanding Ion Conductance on a Molecular Level: An All-Atom Modeling of the Bacterial Porin OmpF. *Biophys. J.* **97**, 1898–1906 (2009).
86. Dargent, B., Hofmann, W., Pattus, F. & Rosenbusch, J. P. The selectivity filter of voltage-dependent channels formed by phosphoporin (PhoE protein) from *E. coli*. *EMBO J.* **5**, 773–778 (1986).
87. Benz, R., Darveau, R. P. & Hancock, R. E. W. Outer-membrane protein PhoE from *Escherichia coli* forms anion-selective pores in lipid-bilayer membranes. *Eur. J. Biochem.* **140**, 319–324 (1984).
88. Watanabe, M., Rosenbusch, J., Schirmer, T. & Karplus, M. Computer simulations of the OmpF porin from the outer membrane of *Escherichia coli*. *Biophys. J.* **72**, 2094–2102 (1997).
89. Eppens, E. F., Saint, N., Gelder, P. V., Bostel, R. van & Tommassen, J. Role of the constriction loop in the gating of outer membrane porin PhoE of *Escherichia coli*. *FEBS Lett.* **415**, 317–320 (1997).
90. Bainbridge, G., Mobasher, H., Armstrong, G. A., Lea, E. J. A. & Lakey, J. H. Voltage-gating of *Escherichia coli* porin: a cysteine-scanning mutagenesis study of loop 311 Edited by I. B. Holland. *J. Mol. Biol.* **275**, 171–176 (1998).
91. Perini, D. A., Alcaraz, A. & Queralt-Martín, M. Lipid Headgroup Charge and Acyl Chain Composition Modulate Closure of Bacterial  $\beta$ -Barrel Channels. *Int. J. Mol. Sci.* **20**, 674 (2019).
92. Aguilera, V. M., Queralt-Martín, M., Aguilera-Arzo, M. & Alcaraz, A. Insights on the permeability of wide protein channels: measurement and interpretation of ion selectivity. *Integr. Biol.* **3**, 159–172 (2011).
93. Queralt-Martín, M., Verdiá-Báguena, C., Aguilera, V. M. & Alcaraz, A. Electrostatic Interactions Drive the Nonsteric Directional Block of OmpF Channel by La<sup>3+</sup>. *Langmuir* **29**, 15320–15327 (2013).
94. Shah, P. & Swiatlo, E. A multifaceted role for polyamines in bacterial pathogens. *Mol. Microbiol.* **68**, 4–16 (2008).
95. Tabor, H. & Tabor, C. W. Polyamine requirement for efficient translation of amber codons in vivo. *Proc. Natl. Acad. Sci.* **79**, 7087–7091 (1982).

96. Ito, K. & Igarashi, K. The increase by spermidine of fidelity of protamine synthesis in a wheat-germ cell-free system. *Eur. J. Biochem.* **156**, 505–510 (1986).
97. Igarashi, K., Sugawara, K., Izumi, I., Nagayama, C. & Hirose, S. Effect of Polyamines on Polyphenylalanine Synthesis by Escherichia coli and Rat-Liver Ribosomes. *Eur. J. Biochem.* **48**, 495–502 (1974).
98. Higashi, K. *et al.* Enhancement of +1 Frameshift by Polyamines during Translation of Polypeptide Release Factor 2 in Escherichia coli\*. *J. Biol. Chem.* **281**, 9527–9537 (2006).
99. Iyer, R. & Delcour, A. H. Complex Inhibition of OmpF and OmpC Bacterial Porins by Polyamines \*. *J. Biol. Chem.* **272**, 18595–18601 (1997).
100. Samartzidou, H. & Delcour, A. H. Excretion of Endogenous Cadaverine Leads to a Decrease in Porin-Mediated Outer Membrane Permeability. *J. Bacteriol.* **181**, 791–798 (1999).
101. Alcaraz, A., Queralt-Martín, M., García-Giménez, E. & Aguilera, V. M. Increased salt concentration promotes competitive block of OmpF channel by protons. *Biochim. Biophys. Acta BBA - Biomembr.* **1818**, 2777–2782 (2012).
102. Kojima, S. & Nikaido, H. High Salt Concentrations Increase Permeability through OmpC Channels of Escherichia coli. *J. Biol. Chem.* **289**, 26464–26473 (2014).
103. Brelidze, T. I. & Magleby, K. L. Protons Block BK Channels by Competitive Inhibition with K<sup>+</sup> and Contribute to the Limits of Unitary Currents at High Voltages. *J. Gen. Physiol.* **123**, 305–319 (2004).
104. Labesse, G. *et al.* MOMP, a Divergent Porin from Campylobacter: Cloning and Primary Structural Characterization. *Biochem. Biophys. Res. Commun.* **280**, 380–387 (2001).
105. Ferguson, A. D. Structural Basis of Gating by the Outer Membrane Transporter FecA. *Science* **295**, 1715–1719 (2002).
106. Moeck, G. S. & Coulton, J. W. TonB-dependent iron acquisition: mechanisms of siderophore-mediated active transport<sup>†</sup>. *Mol. Microbiol.* **28**, 675–681 (1998).
107. Chimento, D. P., Kadner, R. J. & Wiener, M. C. The Escherichia coli Outer Membrane Cobalamin Transporter BtuB: Structural Analysis of Calcium and Substrate Binding, and Identification of Orthologous Transporters by Sequence/Structure Conservation. *J. Mol. Biol.* **332**, 999–1014 (2003).
108. J, T. & B, L. PHO-regulon of Escherichia coli K12: a minireview. *Ann. Microbiol. (Paris)* **133**, 243–249 (1982).
109. Makino, K. *et al.* Signal transduction in the phosphate regulon of Escherichia coli involves phosphotransfer between PhoR and PhoB proteins. *J. Mol. Biol.* **210**, 551–559 (1989).
110. Gerken, H., Vuong, P., Soparkar, K. & Misra, R. Roles of the EnvZ/OmpR Two-Component System and Porins in Iron Acquisition in Escherichia coli. *mBio* **11**, (2020).
111. Delihias, N. Regulation of gene expression by trans-encoded antisense RNAs. *Mol. Microbiol.* **15**, 411–414 (1995).
112. Gutierrez-Ríos, R. M. *et al.* Identification of regulatory network topological units coordinating the genome-wide transcriptional response to glucose in Escherichia coli. *BMC Microbiol.* **7**, 53 (2007).

113. Thomas, A. D. & Booth, I. R. The regulation of expression of the porin gene *ompC* by acid pH. *J. Gen. Microbiol.* **138**, 1829–1835 (1992).
114. Batchelor, E., Walthers, D., Kenney, L. J. & Goulian, M. The Escherichia coli CpxA-CpxR Envelope Stress Response System Regulates Expression of the Porins OmpF and OmpC. *J. Bacteriol.* **187**, 5723–5731 (2005).
115. Alekshun, M. N. & Levy, S. B. Regulation of chromosomally mediated multiple antibiotic resistance: the *mar* regulon. *Antimicrob. Agents Chemother.* **41**, 2067–2075 (1997).
116. Dimple, B. Redox signaling and gene control in the Escherichia coli *soxRS* oxidative stress regulon — a review. *Gene* **179**, 53–57 (1996).
117. Rosenberg, E. Y., Bertenthal, D., Nilles, M. L., Bertrand, K. P. & Nikaido, H. Bile salts and fatty acids induce the expression of Escherichia coli AcrAB multidrug efflux pump through their interaction with Rob regulatory protein. *Mol. Microbiol.* **48**, 1609–1619 (2003).
118. Strahl, H. & Errington, J. Bacterial Membranes: Structure, Domains, and Function. *Annu. Rev. Microbiol.* **71**, 519–538 (2017).
119. Singer, S. J. & Nicolson, G. L. The Fluid Mosaic Model of the Structure of Cell Membranes. *Science* **175**, 720–731 (1972).
120. Vereb, G. *et al.* Dynamic, yet structured: The cell membrane three decades after the Singer–Nicolson model. *Proc. Natl. Acad. Sci.* **100**, 8053–8058 (2003).
121. Sohlenkamp, C. & Geiger, O. Bacterial membrane lipids: diversity in structures and pathways. *FEMS Microbiol. Rev.* **40**, 133–159 (2016).
122. Parsons, J. B. & Rock, C. O. Bacterial lipids: Metabolism and membrane homeostasis. *Prog. Lipid Res.* **52**, 249–276 (2013).
123. Facey, S. J. & Kuhn, A. Membrane integration of E. coli model membrane proteins. *Biochim. Biophys. Acta BBA - Mol. Cell Res.* **1694**, 55–66 (2004).
124. DeFelice, L. J. & Goswami, T. Transporters as Channels. *Annu. Rev. Physiol.* **69**, 87–112 (2007).
125. Booth, I. R., Edwards, M. D. & Miller, S. Bacterial Ion Channels. *Biochemistry* **42**, 10045–10053 (2003).
126. Martinac, B., Saimi, Y. & Kung, C. Ion Channels in Microbes. *Physiol. Rev.* **88**, 1449–1490 (2008).
127. Accardi, A. & Picollo, A. CLC channels and transporters: Proteins with borderline personalities. *Biochim. Biophys. Acta BBA - Biomembr.* **1798**, 1457–1464 (2010).
128. Saier Jr., M. H. The Bacterial Phosphotransferase System: New Frontiers 50 Years after Its Discovery. *J. Mol. Microbiol. Biotechnol.* **25**, 73–78 (2015).
129. Kundig, W., Ghosh, S. & Roseman, S. PHOSPHATE BOUND TO HISTIDINE IN A PROTEIN AS AN INTERMEDIATE IN A NOVEL PHOSPHO-TRANSFERASE SYSTEM. *Proc. Natl. Acad. Sci.* **52**, 1067–1074 (1964).
130. Koebmann, B. J., Westerhoff, H. V., Snoep, J. L., Nilsson, D. & Jensen, P. R. The Glycolytic Flux in Escherichia coli Is Controlled by the Demand for ATP. *J. Bacteriol.* **184**, 3909–3916 (2002).
131. Siebold, C., Flükiger, K., Beutler, R. & Erni, B. Carbohydrate transporters of the bacterial phosphoenolpyruvate: sugar phosphotransferase system (PTS). *FEBS Lett.* **504**, 104–111 (2001).

132. Jeckelmann, J.-M. *et al.* Structure and function of the glucose PTS transporter from *Escherichia coli*. *J. Struct. Biol.* **176**, 395–403 (2011).
133. Moussatova, A., Kandt, C., O'Mara, M. L. & Tieleman, D. P. ATP-binding cassette transporters in *Escherichia coli*. *Biochim. Biophys. Acta BBA - Biomembr.* **1778**, 1757–1771 (2008).
134. Rees, D. C., Johnson, E. & Lewinson, O. ABC transporters: the power to change. *Nat. Rev. Mol. Cell Biol.* **10**, 218–227 (2009).
135. Linton, K. J. & Higgins, C. F. The *Escherichia coli* ATP-binding cassette (ABC) proteins. *Mol. Microbiol.* **28**, 5–13 (1998).
136. Busch, W. & Saier, M. H. The Transporter Classification (TC) System, 2002. *Crit. Rev. Biochem. Mol. Biol.* **37**, 287–337 (2002).
137. Du, D. *et al.* Multidrug efflux pumps: structure, function and regulation. *Nat. Rev. Microbiol.* **16**, 523–539 (2018).
138. Li, X.-Z. & Nikaido, H. Antimicrobial Drug Efflux Pumps in *Escherichia coli*. in *Efflux-Mediated Antimicrobial Resistance in Bacteria: Mechanisms, Regulation and Clinical Implications* (eds. Li, X.-Z., Elkins, C. A. & Zgurskaya, H. I.) 219–259 (Springer International Publishing, 2016). doi:10.1007/978-3-319-39658-3\_9.
139. Sun, J., Deng, Z. & Yan, A. Bacterial multidrug efflux pumps: Mechanisms, physiology and pharmacological exploitations. *Biochem. Biophys. Res. Commun.* **453**, 254–267 (2014).
140. Fitzpatrick, A. W. P. *et al.* Structure of the MacAB–TolC ABC-type tripartite multidrug efflux pump. *Nat. Microbiol.* **2**, 1–8 (2017).
141. Greene, N. P., Kaplan, E., Crow, A. & Koronakis, V. Antibiotic Resistance Mediated by the MacB ABC Transporter Family: A Structural and Functional Perspective. *Front. Microbiol.* **9**, (2018).
142. Jin, M. S., Oldham, M. L., Zhang, Q. & Chen, J. Crystal structure of the multidrug transporter P-glycoprotein from *Caenorhabditis elegans*. *Nature* **490**, 566–569 (2012).
143. Dawson, R. J. P. & Locher, K. P. Structure of a bacterial multidrug ABC transporter. *Nature* **443**, 180–185 (2006).
144. Choudhury, H. G. *et al.* Structure of an antibacterial peptide ATP-binding cassette transporter in a novel outward occluded state. *Proc. Natl. Acad. Sci.* **111**, 9145–9150 (2014).
145. Crow, A., Greene, N. P., Kaplan, E. & Koronakis, V. Structure and mechanotransmission mechanism of the MacB ABC transporter superfamily. *Proc. Natl. Acad. Sci.* **114**, 12572–12577 (2017).
146. Nishino, K. & Yamaguchi, A. Virulence and Drug Resistance Roles of Multidrug Efflux Pumps in *Escherichia coli* and *Salmonella*. *Biosci. Microflora* **27**, 75–85 (2008).
147. Kobayashi, N., Nishino, K. & Yamaguchi, A. Novel Macrolide-Specific ABC-Type Efflux Transporter in *Escherichia coli*. *J. Bacteriol.* **183**, 5639–5644 (2001).
148. Zgurskaya, H. I. & Nikaido, H. Cross-Linked Complex between Oligomeric Periplasmic Lipoprotein AcrA and the Inner-Membrane-Associated Multidrug Efflux Pump AcrB from *Escherichia coli*. *J. Bacteriol.* **182**, 4264–4267 (2000).

149. Tikhonova, E. B., Wang, Q. & Zgurskaya, H. I. Chimeric Analysis of the Multicomponent Multidrug Efflux Transporters from Gram-Negative Bacteria. *J. Bacteriol.* **184**, 6499–6507 (2002).
150. Touzé, T. *et al.* Interactions underlying assembly of the Escherichia coli AcrAB–TolC multidrug efflux system. *Mol. Microbiol.* **53**, 697–706 (2004).
151. Murakami, S., Nakashima, R., Yamashita, E. & Yamaguchi, A. Crystal structure of bacterial multidrug efflux transporter AcrB. *Nature* **419**, 587–593 (2002).
152. Murakami, S., Nakashima, R., Yamashita, E., Matsumoto, T. & Yamaguchi, A. Crystal structures of a multidrug transporter reveal a functionally rotating mechanism. *Nature* **443**, 173–179 (2006).
153. Seeger, M. A., von Ballmoos, C., Verrey, F. & Pos, K. M. Crucial Role of Asp408 in the Proton Translocation Pathway of Multidrug Transporter AcrB: Evidence from Site-Directed Mutagenesis and Carbodiimide Labeling. *Biochemistry* **48**, 5801–5812 (2009).
154. Li, X.-Z., Plésiat, P. & Nikaido, H. The Challenge of Efflux-Mediated Antibiotic Resistance in Gram-Negative Bacteria. *Clin. Microbiol. Rev.* **28**, 337–418 (2015).
155. Du, D. *et al.* Structure of the AcrAB–TolC multidrug efflux pump. *Nature* **509**, 512–515 (2014).
156. Wang, Z. *et al.* An allosteric transport mechanism for the AcrAB-TolC multidrug efflux pump. *eLife* **6**, e24905 (2017).
157. Radestock, S. & Forrest, L. R. The Alternating-Access Mechanism of MFS Transporters Arises from Inverted-Topology Repeats. *J. Mol. Biol.* **407**, 698–715 (2011).
158. Fluman, N., Adler, J., Rotenberg, S. A., Brown, M. H. & Bibi, E. Export of a single drug molecule in two transport cycles by a multidrug efflux pump. *Nat. Commun.* **5**, 4615 (2014).
159. Jiang, D. *et al.* Structure of the YajR transporter suggests a transport mechanism based on the conserved motif A. *Proc. Natl. Acad. Sci.* **110**, 14664–14669 (2013).
160. Heng, J. *et al.* Substrate-bound structure of the E. coli multidrug resistance transporter MdfA. *Cell Res.* **25**, 1060–1073 (2015).
161. Yin, Y., He, X., Szweczyk, P., Nguyen, T. & Chang, G. Structure of the Multidrug Transporter EmrD from Escherichia coli. *Science* **312**, 741–744 (2006).
162. Benarroch, J. M. & Asally, M. The Microbiologist’s Guide to Membrane Potential Dynamics. *Trends Microbiol.* **28**, 304–314 (2020).
163. Schofield, Z. *et al.* Bioelectrical understanding and engineering of cell biology. *J. R. Soc. Interface* **17**, 20200013 (2020).
164. Strahl, H. & Hamoen, L. W. Membrane potential is important for bacterial cell division. *Proc. Natl. Acad. Sci.* **107**, 12281–12286 (2010).
165. Kaim, G. & Dimroth, P. ATP synthesis by F-type ATP synthase is obligatorily dependent on the transmembrane voltage. *EMBO J.* **18**, 4118–4127 (1999).
166. Mulkidjanian, A. Y., Dibrov, P. & Galperin, M. Y. The past and present of sodium energetics: may the sodium-motive force be with you. *Biochim. Biophys. Acta* **1777**, 985–992 (2008).
167. Wilson, T. H. & Ding, P. Z. Sodium-substrate cotransport in bacteria. *Biochim. Biophys. Acta BBA - Bioenerg.* **1505**, 121–130 (2001).

168. Poolman, B. *et al.* Cation and sugar selectivity determinants in a novel family of transport proteins. *Mol. Microbiol.* **19**, 911–922 (1996).
169. Pourcher, T., Bibi, E., Kaback, H. R. & Leblanc, G. Membrane Topology of the Melibiose Permease of *Escherichia coli* Studied by melB–phoA Fusion Analysis. *Biochemistry* **35**, 4161–4168 (1996).
170. Hacksell, I. *et al.* Projection structure at 8 Å resolution of the melibiose permease, an Na<sup>+</sup>-sugar co-transporter from *Escherichia coli*. *EMBO J.* **21**, 3569–3574 (2002).
171. Purhonen, P., Lundbäck, A.-K., Lemonnier, R., Leblanc, G. & Hebert, H. Three-dimensional structure of the sugar symporter melibiose permease from cryo-electron microscopy. *J. Struct. Biol.* **152**, 76–83 (2005).
172. Wilson, D. M. & Wilson, T. H. Cation specificity for sugar substrates of the melibiose carrier in *Escherichia coli*. *Biochim. Biophys. Acta BBA - Biomembr.* **904**, 191–200 (1987).
173. Pourcher, T. *et al.* The melibiose/Na<sup>+</sup> symporter of *Escherichia coli*: kinetic and molecular properties. *Philos. Trans. R. Soc. Lond. B Biol. Sci.* **326**, 411–423 (1990).
174. Rotman, B., Ganesan, A. K. & Guzman, R. Transport systems for galactose and galactosides in *Escherichia coli*. *J. Mol. Biol.* **36**, 247–260 (1968).
175. Pardee, A. B. An Inducible Mechanism for Accumulation of Melibiose in *Escherichia coli*. *J. Bacteriol.* **73**, 376–385 (1957).
176. Jung, H. The sodium/substrate symporter family: structural and functional features. *FEBS Lett.* **529**, 73–77 (2002).
177. Jung, H. Towards the molecular mechanism of Na<sup>+</sup>/solute symport in prokaryotes. *Biochim. Biophys. Acta BBA - Bioenerg.* **1505**, 131–143 (2001).
178. Hilger, D., Polyhach, Y., Jung, H. & Jeschke, G. Backbone Structure of Transmembrane Domain IX of the Na<sup>+</sup>/Proline Transporter PutP of *Escherichia coli*. *Biophys. J.* **96**, 217–225 (2009).
179. Chen, C. C. & Wilson, T. H. Solubilization and functional reconstitution of the proline transport system of *Escherichia coli*. *J. Biol. Chem.* **261**, 2599–2604 (1986).
180. Kayama, Y. & Kawasaki, T. Stimulatory effect of lithium ion on proline transport by whole cells of *Escherichia coli*. *J. Bacteriol.* **128**, 157–164 (1976).
181. Karpel, R., Alon, T., Glaser, G., Schuldiner, S. & Padan, E. Expression of a sodium proton antiporter (NhaA) in *Escherichia coli* is induced by Na<sup>+</sup> and Li<sup>+</sup> ions. *J. Biol. Chem.* **266**, 21753–21759 (1991).
182. Pinner, E., Padan, E. & Schuldiner, S. Cloning, sequencing, and expression of the nhaB gene, encoding a Na<sup>+</sup>/H<sup>+</sup> antiporter in *Escherichia coli*. *J. Biol. Chem.* **267**, 11064–11068 (1992).
183. Padan, E., Bibi, E., Ito, M. & Krulwich, T. A. Alkaline pH homeostasis in bacteria: New insights. *Biochim. Biophys. Acta BBA - Biomembr.* **1717**, 67–88 (2005).
184. Hilger, D., Polyhach, Y., Padan, E., Jung, H. & Jeschke, G. High-Resolution Structure of a Na<sup>+</sup>/H<sup>+</sup> Antiporter Dimer Obtained by Pulsed Electron Paramagnetic Resonance Distance Measurements. *Biophys. J.* **93**, 3675–3683 (2007).

185. Hilger, D. *et al.* Assessing Oligomerization of Membrane Proteins by Four-Pulse DEER: pH-Dependent Dimerization of NhaA Na<sup>+</sup>/H<sup>+</sup> Antiporter of *E. coli*. *Biophys. J.* **89**, 1328–1338 (2005).
186. Gerchman, Y., Rimon, A., Venturi, M. & Padan, E. Oligomerization of NhaA, the Na<sup>+</sup>/H<sup>+</sup> Antiporter of *Escherichia coli* in the Membrane and Its Functional and Structural Consequences. *Biochemistry* **40**, 3403–3412 (2001).
187. Rimon, A., Tzubery, T. & Padan, E. Monomers of the NhaA Na<sup>+</sup>/H<sup>+</sup> Antiporter of *Escherichia coli* Are Fully Functional yet Dimers Are Beneficial under Extreme Stress Conditions at Alkaline pH in the Presence of Na<sup>+</sup> or Li<sup>+</sup>\*. *J. Biol. Chem.* **282**, 26810–26821 (2007).
188. Herz, K., Rimon, A., Jeschke, G. & Padan, E.  $\beta$ -Sheet-dependent Dimerization Is Essential for the Stability of NhaA Na<sup>+</sup>/H<sup>+</sup> Antiporter\*. *J. Biol. Chem.* **284**, 6337–6347 (2009).
189. Hunte, C. *et al.* Structure of a Na<sup>+</sup> /H<sup>+</sup> antiporter and insights into mechanism of action and regulation by pH. *Nature* **435**, 1197–1202 (2005).
190. Lee, C. *et al.* Crystal structure of the sodium-proton antiporter NhaA dimer and new mechanistic insights. *J. Gen. Physiol.* **144**, 529–544 (2014).
191. Rothman, A., Padan, E. & Schuldiner, S. Topological Analysis of NhaA, a Na<sup>+</sup>/H<sup>+</sup> Antiporter from *Escherichia coli*\*. *J. Biol. Chem.* **271**, 32288–32292 (1996).
192. Williams, K. A. Three-dimensional structure of the ion-coupled transport protein NhaA. *Nature* **403**, 112–115 (2000).
193. Pinner, E., Padan, E. & Schuldiner, S. Kinetic properties of NhaB, a Na<sup>+</sup>/H<sup>+</sup> antiporter from *Escherichia coli*. *J. Biol. Chem.* **269**, 26274–26279 (1994).
194. Schultz, S. G., Epstein, W. & Solomon, A. K. Cation Transport in *Escherichia coli* : IV. Kinetics of net K uptake. *J. Gen. Physiol.* **47**, 329–346 (1963).
195. Rhoads, D. B., Waters, F. B. & Epstein, W. Cation transport in *Escherichia coli*. VIII. Potassium transport mutants. *J. Gen. Physiol.* **67**, 325–341 (1976).
196. Laimins, L. A., Rhoads, D. B., Altendorf, K. & Epstein, W. Identification of the structural proteins of an ATP-driven potassium transport system in *Escherichia coli*. *Proc. Natl. Acad. Sci. U. S. A.* **75**, 3216–3219 (1978).
197. Sigworth, F. J. Voltage gating of ion channels. *Q. Rev. Biophys.* **27**, 1–40 (1994).
198. Durell, S. R., Bakker, E. P. & Guy, H. R. Does the KdpA Subunit from the High Affinity K<sup>+</sup>-Translocating P-Type KDP-ATPase have a Structure Similar to That of K<sup>+</sup> Channels? *Biophys. J.* **78**, 188–199 (2000).
199. Pedersen, B. P., Stokes, D. L. & Apell, H.-J. The KdpFABC complex – K<sup>+</sup> transport against all odds. *Mol. Membr. Biol.* **35**, 21–38 (2019).
200. Gaßel, M., Siebers, A., Epstein, W. & Altendorf, K. Assembly of the Kdp complex, the multi-subunit K<sup>+</sup>-transport ATPase of *Escherichia coli*. *Biochim. Biophys. Acta BBA - Biomembr.* **1415**, 77–84 (1998).
201. Epstein, W. & Davies, M. Potassium-Dependant Mutants of *Escherichia coli* K-12. *J. Bacteriol.* **101**, 836–843 (1970).
202. Polarek, J. W., Walderhaug, M. O. & Epstein, W. [51] Genetics of Kdp, the K<sup>+</sup>-transport ATPase of *Escherichia coli*. in *Methods in Enzymology* vol. 157 655–667 (Academic Press, 1988).

203. Ballal, A., Basu, B. & Apte, S. K. The Kdp-ATPase system and its regulation. *J. Biosci.* **32**, 559–568 (2007).
204. *Ion Transport in Prokaryotes*. (Elsevier, 1987). doi:10.1016/C2013-0-11399-2.
205. Schlösser, A., Meldorf, M., Stumpe, S., Bakker, E. P. & Epstein, W. TrkH and its homolog, TrkG, determine the specificity and kinetics of cation transport by the Trk system of *Escherichia coli*. *J. Bacteriol.* **177**, 1908–1910 (1995).
206. Dosch, D. C., Helmer, G. L., Sutton, S. H., Salvacion, F. F. & Epstein, W. Genetic analysis of potassium transport loci in *Escherichia coli*: evidence for three constitutive systems mediating uptake potassium. *J. Bacteriol.* **173**, 687–696 (1991).
207. Bossemeyer, D. *et al.* K<sup>+</sup>-transport Protein TrkA of *Escherichia coli* Is a Peripheral Membrane Protein That Requires other trk Gene Products for Attachment to the Cytoplasmic Membrane\*. *J. Biol. Chem.* **264**, 16403–16410 (1989).
208. Schlosser, A., Hamann, A., Bossemeyer, D., Schneider, E. & Bakker, E. P. NAD<sup>+</sup> binding to the *Escherichia coli* K<sup>+</sup>-uptake protein TrkA and sequence similarity between TrkA and domains of a family of dehydrogenases suggest a role for NAD<sup>+</sup> in bacterial transport. *Mol. Microbiol.* **9**, 533–543 (1993).
209. Bossemeyer, D., Schlösser, A. & Bakker, E. P. Specific cesium transport via the *Escherichia coli* Kup (TrkD) K<sup>+</sup> uptake system. *J. Bacteriol.* **171**, 2219–2221 (1989).
210. Schleyer, M. & Bakker, E. P. Nucleotide sequence and 3'-end deletion studies indicate that the K<sup>(+)</sup>-uptake protein kup from *Escherichia coli* is composed of a hydrophobic core linked to a large and partially essential hydrophilic C terminus. *J. Bacteriol.* **175**, 6925–6931 (1993).
211. Sato, Y. *et al.* Defining membrane spanning domains and crucial membrane-localized acidic amino acid residues for K<sup>+</sup> transport of a Kup/HAK/KT-type *Escherichia coli* potassium transporter. *J. Biochem. (Tokyo)* **155**, 315–323 (2014).
212. Doyle, D. A. *et al.* The Structure of the Potassium Channel: Molecular Basis of K<sup>+</sup> Conduction and Selectivity. *Science* **280**, 69–77 (1998).
213. Prindle, A. *et al.* Ion channels enable electrical communication within bacterial communities. *Nature* **527**, 59–63 (2015).
214. Liu, J. *et al.* Metabolic co-dependence gives rise to collective oscillations within biofilms. *Nature* **523**, 550–554 (2015).
215. Li, Y. Ionic regulation of MscK, a mechanosensitive channel from *Escherichia coli*. *EMBO J.* **21**, 5323–5330 (2002).
216. Levina, N. *et al.* Protection of *Escherichia coli* cells against extreme turgor by activation of MscS and MscL mechanosensitive channels: identification of genes required for MscS activity. *EMBO J.* **18**, 1730–1737 (1999).
217. Li, C., Edwards, M. D., Jeong, H., Roth, J. & Booth, I. R. Identification of mutations that alter the gating of the *Escherichia coli* mechanosensitive channel protein, MscK. *Mol. Microbiol.* **64**, 560–574 (2007).
218. Arif, M., Howard, J. & Tisa, L. S. Calcium Homeostasis in *Escherichia coli*: Characterization of Mutants and Genome Expression of MG1655. *Bangladesh J. Microbiol.* 1–8 (2016) doi:10.3329/bjm.v31i1.28457.

219. Gangola, P. & Rosen, B. P. Maintenance of intracellular calcium in Escherichia coli. *J. Biol. Chem.* **262**, 12570–12574 (1987).
220. Ivey, D. M. *et al.* Cloning and characterization of a putative Ca<sup>2+</sup>/H<sup>+</sup> antiporter gene from Escherichia coli upon functional complementation of Na<sup>+</sup>/H<sup>+</sup> antiporter-deficient strains by the overexpressed gene. *J. Biol. Chem.* **268**, 11296–11303 (1993).
221. Brey, R. N. & Rosen, B. P. Properties of Escherichia coli mutants altered in calcium/proton antiport activity. *J. Bacteriol.* **139**, 824–834 (1979).
222. Roeßler, M., Sewald, X. & Müller, V. Chloride dependence of growth in bacteria. *FEMS Microbiol. Lett.* **225**, 161–165 (2003).
223. Maduke, M., Pheasant, D. J. & Miller, C. High-Level Expression, Functional Reconstitution, and Quaternary Structure of a Prokaryotic Clc-Type Chloride Channel. *J. Gen. Physiol.* **114**, 713–722 (1999).
224. Accardi, A. & Miller, C. Secondary active transport mediated by a prokaryotic homologue of ClC Cl<sup>-</sup> channels. *Nature* **427**, 803–807 (2004).
225. Iyer, R., Iverson, T. M., Accardi, A. & Miller, C. A biological role for prokaryotic ClC chloride channels. *Nature* **419**, 715–718 (2002).
226. Kloda, A. *et al.* Mechanosensitive channel of large conductance. *Int. J. Biochem. Cell Biol.* **40**, 164–169 (2008).
227. Edwards, M. D. *et al.* Characterization of three novel mechanosensitive channel activities in Escherichia coli. *Channels* **6**, 272–281 (2012).
228. Schumann, U. *et al.* YbdG in Escherichia coli is a threshold-setting mechanosensitive channel with MscM activity. *Proc. Natl. Acad. Sci.* **107**, 12664–12669 (2010).
229. Sukharev, S. I., Blount, P., Martinac, B., Blattner, F. R. & Kung, C. A large-conductance mechanosensitive channel in E. coli encoded by mscL alone. *Nature* **368**, 265–268 (1994).
230. Saint, N. *et al.* A Hexameric Transmembrane Pore Revealed by Two-dimensional Crystallization of the Large Mechanosensitive Ion Channel (MscL) of Escherichia coli \*. *J. Biol. Chem.* **273**, 14667–14670 (1998).
231. Blount, P. *et al.* Membrane topology and multimeric structure of a mechanosensitive channel protein of Escherichia coli. *EMBO J.* **15**, 4798–4805 (1996).
232. Koprowski, P. & Kubalski, A. Voltage-independent Adaptation of Mechanosensitive Channels in Escherichia coli Protoplasts. *J. Membr. Biol.* **164**, 253–262 (1998).
233. Akitake, B., Anishkin, A. & Sukharev, S. The “Dashpot” Mechanism of Stretch-dependent Gating in MscS. *J. Gen. Physiol.* **125**, 143–154 (2005).
234. Stenberg, F. *et al.* Protein Complexes of the Escherichia coli Cell Envelope\*,. *J. Biol. Chem.* **280**, 34409–34419 (2005).
235. Bass, R. B., Strop, P., Barclay, M. & Rees, D. C. Crystal Structure of Escherichia coli MscS, a Voltage-Modulated and Mechanosensitive Channel. *Science* **298**, 1582–1587 (2002).
236. Machiyama, H., Tatsumi, H. & Sokabe, M. Structural Changes in the Cytoplasmic Domain of the Mechanosensitive Channel MscS During Opening. *Biophys. J.* **97**, 1048–1057 (2009).
237. Booth, I. R. & Blount, P. The MscS and MscL Families of Mechanosensitive Channels Act as Microbial Emergency Release Valves. *J. Bacteriol.* **194**, 4802–4809 (2012).
238. Berry, R. The Bacterial Flagellar Motor. in *Molecular Motors* 111–140 (John Wiley & Sons, Ltd, 2002). doi:10.1002/3527601503.ch4.

239. Berry, R. M. & Armitage, J. P. The Bacterial Flagella Motor. in *Advances in Microbial Physiology* (ed. Poole, R. K.) vol. 41 291–337 (Academic Press, 1999).
240. Reid, S. W. *et al.* The maximum number of torque-generating units in the flagellar motor of *Escherichia coli* is at least 11. *Proc. Natl. Acad. Sci.* **103**, 8066–8071 (2006).
241. Kopp, D. R. & Postle, K. The Intrinsically Disordered Region of ExbD Is Required for Signal Transduction. *J. Bacteriol.* **202**, (2020).
242. Padan, E., Zilberstein, D. & Rottenberg, H. The Proton Electrochemical Gradient in *Escherichia coli* Cells. *Eur. J. Biochem.* **63**, 533–541 (1976).
243. Taylor, B. L. Role of Proton Motive Force in Sensory Transduction in Bacteria. *Annu. Rev. Microbiol.* **37**, 551–573 (1983).
244. Ingledew, W. J. & Poole, R. K. The respiratory chains of *Escherichia coli*. *Microbiol. Rev.* **48**, 222–271 (1984).
245. Wilks, J. C. & Slonczewski, J. L. pH of the Cytoplasm and Periplasm of *Escherichia coli*: Rapid Measurement by Green Fluorescent Protein Fluorimetry. *J. Bacteriol.* **189**, 5601–5607 (2007).
246. Wen, Y. *et al.* Measurement of Internal pH in *Helicobacter pylori* by Using Green Fluorescent Protein Fluorimetry. *J. Bacteriol.* **200**, (2018).
247. Kashket, E. R. The Proton Motive Force in Bacteria: A Critical Assessment of Methods. *Annu. Rev. Microbiol.* **39**, 219–242 (1985).
248. Tran, Q. H. & Unden, G. Changes in the proton potential and the cellular energetics of *Escherichia coli* during growth by aerobic and anaerobic respiration or by fermentation. *Eur. J. Biochem.* **251**, 538–543 (1998).
249. Hardiman, T., Lemuth, K., Keller, M. A., Reuss, M. & Siemann-Herzberg, M. Topology of the global regulatory network of carbon limitation in *Escherichia coli*. *J. Biotechnol.* **132**, 359–374 (2007).
250. Bender, R. A. Glycolysis. in *Brenner's Encyclopedia of Genetics (Second Edition)* (eds. Maloy, S. & Hughes, K.) 346–349 (Academic Press, 2013). doi:10.1016/B978-0-12-374984-0.00659-8.
251. Gunsalus, I. C. Bacterial Metabolism. *Annu. Rev. Microbiol.* **2**, 71–100 (1948).
252. Dolan, S. K. & Welch, M. The Glyoxylate Shunt, 60 Years On. *Annu. Rev. Microbiol.* **72**, 309–330 (2018).
253. Kumari, A. Chapter 2 - Citric Acid Cycle. in *Sweet Biochemistry* (ed. Kumari, A.) 7–11 (Academic Press, 2018). doi:10.1016/B978-0-12-814453-4.00002-9.
254. Fernie, A. R., Carrari, F. & Sweetlove, L. J. Respiratory metabolism: glycolysis, the TCA cycle and mitochondrial electron transport. *Curr. Opin. Plant Biol.* **7**, 254–261 (2004).
255. Bender, D. A. OXIDATIVE PHOSPHORYLATION. in *Encyclopedia of Food Sciences and Nutrition (Second Edition)* (ed. Caballero, B.) 4295–4301 (Academic Press, 2003). doi:10.1016/B0-12-227055-X/01407-3.
256. Unden, G. & Bongaerts, J. Alternative respiratory pathways of *Escherichia coli*: energetics and transcriptional regulation in response to electron acceptors. *Biochim. Biophys. Acta BBA - Bioenerg.* **1320**, 217–234 (1997).

257. Berrisford, J. M., Baradaran, R. & Sazanov, L. A. Structure of bacterial respiratory complex I. *Biochim. Biophys. Acta BBA - Bioenerg.* **1857**, 892–901 (2016).
258. Borisov, V. B., Gennis, R. B., Hemp, J. & Verkhovsky, M. I. The cytochrome bd respiratory oxygen reductases. *Biochim. Biophys. Acta BBA - Bioenerg.* **1807**, 1398–1413 (2011).
259. Gevorgyan, H., Trchounian, A. & Trchounian, K. Understanding the Role of Escherichia coli Hydrogenases and Formate Dehydrogenases in the FOF1-ATPase Activity during the Mixed Acid Fermentation of Mixture of Carbon Sources. *IUBMB Life* **70**, 1040–1047 (2018).
260. Almendro-Vedia, V. G. *et al.* Nonequilibrium fluctuations of lipid membranes by the rotating motor protein F1FO-ATP synthase. *Proc. Natl. Acad. Sci.* **114**, 11291–11296 (2017).
261. Junge, W. & Nelson, N. ATP Synthase. *Annu. Rev. Biochem.* **84**, 631–657 (2015).
262. D'Alessandro, M., Turina, P. & Melandri, B. A. Intrinsic uncoupling in the ATP synthase of Escherichia coli. *Biochim. Biophys. Acta BBA - Bioenerg.* **1777**, 1518–1527 (2008).
263. Wächter, A. *et al.* Two rotary motors in F-ATP synthase are elastically coupled by a flexible rotor and a stiff stator stalk. *Proc. Natl. Acad. Sci.* **108**, 3924–3929 (2011).
264. Walker, J. E. The NADH:ubiquinone oxidoreductase (complex I) of respiratory chains. *Q. Rev. Biophys.* **25**, 253–324 (1992).
265. Yagi, T. & Matsuno-Yagi, A. The Proton-Translocating NADH–Quinone Oxidoreductase in the Respiratory Chain: The Secret Unlocked. *Biochemistry* **42**, 2266–2274 (2003).
266. Ohnishi, T., Nakamaru-Ogiso, E. & Ohnishi, S. T. A new hypothesis on the simultaneous direct and indirect proton pump mechanisms in NADH-quinone oxidoreductase (complex I). *FEBS Lett.* **584**, 4131–4137 (2010).
267. Friedrich, T., Hellwig, P. & Einsle, O. On the Mechanism of the Respiratory Complex I. in *A Structural Perspective on Respiratory Complex I: Structure and Function of NADH:ubiquinone oxidoreductase* (ed. Sazanov, L.) 23–59 (Springer Netherlands, 2012). doi:10.1007/978-94-007-4138-6\_2.
268. Friedrich, T., Dekovic, D. K. & Burschel, S. Assembly of the Escherichia coli NADH:ubiquinone oxidoreductase (respiratory complex I). *Biochim. Biophys. Acta BBA - Bioenerg.* **1857**, 214–223 (2016).
269. Friedrich, T. Complex I: A Chimaera of a Redox and Conformation-Driven Proton Pump? *J. Bioenerg. Biomembr.* **33**, 169–177 (2001).
270. Friedrich, T. & Weiss, H. Modular Evolution of the Respiratory NADH:Ubiquinone Oxidoreductase and the Origin of its Modules. *J. Theor. Biol.* **187**, 529–540 (1997).
271. Jervis, A. J. *et al.* The O<sub>2</sub> sensitivity of the transcription factor FNR is controlled by Ser24 modulating the kinetics of [4Fe-4S] to [2Fe-2S] conversion. *Proc. Natl. Acad. Sci.* **106**, 4659–4664 (2009).
272. Sazanov, L. A., Carroll, J., Holt, P., Toime, L. & Fearnley, I. M. A Role for Native Lipids in the Stabilization and Two-dimensional Crystallization of the Escherichia coli NADH-Ubiquinone Oxidoreductase (Complex I)\*. *J. Biol. Chem.* **278**, 19483–19491 (2003).
273. Kita, K., Vibat, C. R., Meinhardt, S., Guest, J. R. & Gennis, R. B. One-step purification from Escherichia coli of complex II (succinate: ubiquinone oxidoreductase) associated with succinate-reducible cytochrome b556. *J. Biol. Chem.* **264**, 2672–2677 (1989).
274. Tomasiak, T. M., Maklashina, E., Cecchini, G. & Iverson, T. M. A Threonine on the Active Site Loop Controls Transition State Formation in Escherichia coli Respiratory Complex II\*. *J. Biol. Chem.* **283**, 15460–15468 (2008).

275. Shimizu, H. *et al.* Screening of detergents for solubilization, purification and crystallization of membrane proteins: a case study on succinate:ubiquinone oxidoreductase from *Escherichia coli*. *Acta Crystallograph. Sect. F Struct. Biol. Cryst. Commun.* **64**, 858–862 (2008).
276. Cecchini, G., Schröder, I., Gunsalus, R. P. & Maklashina, E. Succinate dehydrogenase and fumarate reductase from *Escherichia coli*. *Biochim. Biophys. Acta BBA - Bioenerg.* **1553**, 140–157 (2002).
277. Tseng, C. P., Albrecht, J. & Gunsalus, R. P. Effect of microaerophilic cell growth conditions on expression of the aerobic (cyoABCDE and cydAB) and anaerobic (narGHJI, frdABCD, and dmsABC) respiratory pathway genes in *Escherichia coli*. *J. Bacteriol.* **178**, 1094–1098 (1996).
278. Borisov, V. B. *et al.* Aerobic respiratory chain of *Escherichia coli* is not allowed to work in fully uncoupled mode. *Proc. Natl. Acad. Sci.* **108**, 17320–17324 (2011).
279. Puustinen, A., Finel, M., Haltia, T., Gennis, R. B. & Wikstrom, M. Properties of the two terminal oxidases of *Escherichia coli*. *Biochemistry* **30**, 3936–3942 (1991).
280. Jones, S. A. *et al.* Respiration of *Escherichia coli* in the Mouse Intestine. *Infect. Immun.* **75**, 4891–4899 (2007).
281. Loisel-Meyer, S., de Bagüés, M. P. J., Köhler, S., Liautard, J.-P. & Jubier-Maurin, V. Differential Use of the Two High-Oxygen-Affinity Terminal Oxidases of *Brucella suis* for In Vitro and Intramacrophagic Multiplication. *Infect. Immun.* **73**, 7768–7771 (2005).
282. Baughn, A. D. & Malamy, M. H. The strict anaerobe *Bacteroides fragilis* grows in and benefits from nanomolar concentrations of oxygen. *Nature* **427**, 441–444 (2004).
283. Shi, L. *et al.* Changes in energy metabolism of *Mycobacterium tuberculosis* in mouse lung and under in vitro conditions affecting aerobic respiration. *Proc. Natl. Acad. Sci.* **102**, 15629–15634 (2005).
284. Hill, J. J., Alben, J. O. & Gennis, R. B. Spectroscopic evidence for a heme-heme binuclear center in the cytochrome bd ubiquinol oxidase from *Escherichia coli*. *Proc. Natl. Acad. Sci.* **90**, 5863–5867 (1993).
285. Arutyunyan, A. M. *et al.* Strong Excitonic Interactions in the Oxygen-Reducing Site of bd-Type Oxidase: The Fe-to-Fe Distance between Hemes d and b595 is 10 Å. *Biochemistry* **47**, 1752–1759 (2008).
286. Vos, M. H., Borisov, V. B., Liebl, U., Martin, J.-L. & Konstantinov, A. A. Femtosecond resolution of ligand-heme interactions in the high-affinity quinol oxidase bd: A di-heme active site? *Proc. Natl. Acad. Sci.* **97**, 1554–1559 (2000).
287. Avetisyan, A. V., Bogachev, A. V., Murtasina, R. A. & Skulachev, V. P. Involvement of a d-type oxidase in the Na<sup>+</sup>-motive respiratory chain of *Escherichia coli* growing under low Δ<sup>gm</sup>H<sup>+</sup> conditions. *FEBS Lett.* **306**, 199–202 (1992).
288. Lindqvist, A., Membrillo-Hernández, J., Poole, R. K. & Cook, G. M. Roles of respiratory oxidases in protecting *Escherichia coli* K12 from oxidative stress. *Antonie Van Leeuwenhoek* **78**, 23–31 (2000).
289. Wall, D. *et al.* arc-dependent thermal regulation and extragenic suppression of the *Escherichia coli* cytochrome d operon. *J. Bacteriol.* **174**, 6554–6562 (1992).

290. Delaney, J. M., Wall, D. & Georgopoulos, C. Molecular characterization of the Escherichia coli htrD gene: cloning, sequence, regulation, and involvement with cytochrome d oxidase. *J. Bacteriol.* **175**, 166–175 (1993).
291. Bogachev, A. V., Murtazina, R. A. & Skulachev, V. P. Cytochrome d induction in Escherichia coli growing under unfavorable conditions. *FEBS Lett.* **336**, 75–78 (1993).
292. Borisov, V. B. *et al.* Redox control of fast ligand dissociation from Escherichia coli cytochrome bd. *Biochem. Biophys. Res. Commun.* **355**, 97–102 (2007).
293. Mason, M. G. *et al.* Cytochrome bd confers nitric oxide resistance to Escherichia coli. *Nat. Chem. Biol.* **5**, 94–96 (2009).
294. Forte, E. *et al.* Cytochrome bd, a key oxidase in bacterial survival and tolerance to nitrosative stress. **56**, 6 (2007).
295. Govantes, F., Albrecht, J. A. & Gunsalus, R. P. Oxygen regulation of the Escherichia coli cytochrome d oxidase (cydAB) operon: roles of multiple promoters and the Fnr-1 and Fnr-2 binding sites. *Mol. Microbiol.* **37**, 1456–1469 (2000).
296. Nakamura, H., Yamato, I., Anraku, Y., Lemieux, L. & Gennis, R. B. Expression of cyoA and cyoB demonstrates that the CO-binding heme component of the Escherichia coli cytochrome o complex is in subunit I. *J. Biol. Chem.* **265**, 11193–11197 (1990).
297. Shimada, T., Fujita, N., Yamamoto, K. & Ishihama, A. Novel Roles of cAMP Receptor Protein (CRP) in Regulation of Transport and Metabolism of Carbon Sources. *PLOS ONE* **6**, e20081 (2011).
298. Minghetti, K. C. *et al.* Modified, large-scale purification of the cytochrome o complex (bo-type oxidase) of Escherichia coli yields a two heme/one copper terminal oxidase with high specific activity. *Biochemistry* **31**, 6917–6924 (1992).
299. Bekker, M., de Vries, S., Ter Beek, A., Hellingwerf, K. J. & de Mattos, M. J. T. Respiration of Escherichia coli Can Be Fully Uncoupled via the Nonelectrogenic Terminal Cytochrome bd-II Oxidase. *J. Bacteriol.* **191**, 5510–5517 (2009).
300. Matsushita, K., Patel, L. & Kaback, H. R. Cytochrome o oxidase from Escherichia coli. Characterization of the enzyme and mechanism of electrochemical proton gradient generation. *Biochemistry* **23**, 4703–4714 (1984).
301. Melin, F. *et al.* Role of the tightly bound quinone for the oxygen reaction of cytochrome bo<sub>3</sub> oxidase from Escherichia coli. *FEBS Lett.* **592**, 3380–3387 (2018).
302. Dassa, J. *et al.* A new oxygen-regulated operon in Escherichia coli comprises the genes for a putative third cytochrome oxidase and for pH 2.5 acid phosphatase ( appA ). *Mol. Gen. Genet. MGG* **229**, 341–352 (1991).
303. Sturr, M. G., Krulwich, T. A. & Hicks, D. B. Purification of a cytochrome bd terminal oxidase encoded by the Escherichia coli app locus from a delta cyo delta cyd strain complemented by genes from Bacillus firmus OF4. *J. Bacteriol.* **178**, 1742–1749 (1996).
304. Atlung, T. & Brøndsted, L. Role of the transcriptional activator AppY in regulation of the cyx appA operon of Escherichia coli by anaerobiosis, phosphate starvation, and growth phase. *J. Bacteriol.* **176**, 5414–5422 (1994).
305. Senior, A. E. The Proton-Translocating ATPase of Escherichia Coli. *Annu. Rev. Biophys. Biophys. Chem.* **19**, 7–41 (1990).
306. Mitchell, P. Coupling of Phosphorylation to Electron and Hydrogen Transfer by a Chemi-Osmotic type of Mechanism. *Nature* **191**, 144–148 (1961).

307. Mitchell, P. Chemiosmotic coupling in oxidative and photosynthetic phosphorylation. *Biochim. Biophys. Acta BBA - Bioenerg.* **1807**, 1507–1538 (2011).
308. Guo, H., Suzuki, T. & Rubinstein, J. L. Structure of a bacterial ATP synthase. *eLife* **8**, e43128 (2019).
309. Trchounian, A. Escherichia coli proton-translocating FOF1-ATP synthase and its association with solute secondary transporters and/or enzymes of anaerobic oxidation–reduction under fermentation. *Biochem. Biophys. Res. Commun.* **315**, 1051–1057 (2004).
310. Rieger, B., Junge, W. & Busch, K. B. Lateral pH gradient between OXPHOS complex IV and FOF1 ATP-synthase in folded mitochondrial membranes. *Nat. Commun.* **5**, 3103 (2014).
311. Santo-Domingo, J., Giacomello, M., Poburko, D., Scorrano, L. & Demarex, N. OPA1 promotes pH flashes that spread between contiguous mitochondria without matrix protein exchange. *EMBO J.* **32**, 1927–1940 (2013).
312. Azarias, G. & Chatton, J.-Y. Selective Ion Changes during Spontaneous Mitochondrial Transients in Intact Astrocytes. *PLOS ONE* **6**, e28505 (2011).
313. Sel'kov, E. E. Self-Oscillations in Glycolysis 1. A Simple Kinetic Model. *Eur. J. Biochem.* **4**, 79–86 (1968).
314. Ghosh, A. & Chance, B. Oscillations of glycolytic intermediates in yeast cells. *Biochem. Biophys. Res. Commun.* **16**, 174–181 (1964).
315. Gehrman, E. *et al.* Robustness of glycolysis in yeast to internal and external noise. *Phys. Rev. E* **84**, 021913 (2011).
316. Sel'Kov, E. E. Stabilization of Energy Charge, Generation of Oscillations and Multiple Steady States in Energy Metabolism as a Result of Purely Stoichiometric Regulation. *Eur. J. Biochem.* **59**, 151–157 (1975).
317. Chandra, F. A., Buzi, G. & Doyle, J. C. Glycolytic Oscillations and Limits on Robust Efficiency. *Science* **333**, 187–192 (2011).
318. Cortassa, S., Aon, M. A. & Thomas, D. Thermodynamic and kinetic studies of a stoichiometric model of energetic metabolism under starvation conditions. *FEMS Microbiol. Lett.* **66**, 249–255 (1990).
319. Maria, G. In silico Determination of Some Conditions Leading to Glycolytic Oscillations and Their Interference With Some Other Processes in E. coli Cells. *Front. Chem.* **8**, 977 (2020).
320. Papagiannakis, A., Niebel, B., Wit, E. C. & Heinemann, M. Autonomous Metabolic Oscillations Robustly Gate the Early and Late Cell Cycle. *Mol. Cell* **65**, 285–295 (2017).
321. Zhang, Z., Miliadis-Argeitis, A. & Heinemann, M. Dynamic single-cell NAD(P)H measurement reveals oscillatory metabolism throughout the E. coli cell division cycle. *Sci. Rep.* **8**, 2162 (2018).
322. Martinez-Corral, R., Liu, J., Süel, G. M. & Garcia-Ojalvo, J. Bistable emergence of oscillations in growing Bacillus subtilis biofilms. *Proc. Natl. Acad. Sci.* **115**, E8333–E8340 (2018).
323. Kralj, J. M., Hochbaum, D. R., Douglass, A. D. & Cohen, A. E. Electrical Spiking in Escherichia coli Probed with a Fluorescent Voltage-Indicating Protein. *Science* **333**, 345–348 (2011).

324. Bruni, G. N., Weekley, R. A., Dodd, B. J. T. & Kralj, J. M. Voltage-gated calcium flux mediates *Escherichia coli* mechanosensation. *Proc. Natl. Acad. Sci.* **114**, 9445–9450 (2017).
325. Lee, J.-H. & Lee, J. Indole as an intercellular signal in microbial communities. *FEMS Microbiol. Rev.* **34**, 426–444 (2010).
326. Zarkan, A., Liu, J., Matuszewska, M., Gaimster, H. & Summers, D. K. Local and Universal Action: The Paradoxes of Indole Signalling in Bacteria. *Trends Microbiol.* **28**, 566–577 (2020).
327. DeMoss, R. D. & Moser, K. Tryptophanase in Diverse Bacterial Species. *J. Bacteriol.* **98**, 167–171 (1969).
328. Humphrey, G. R. & Kuethe, J. T. Practical Methodologies for the Synthesis of Indoles. *Chem. Rev.* **106**, 2875–2911 (2006).
329. Zarkan, A. *et al.* Indole Pulse Signalling Regulates the Cytoplasmic pH of *E. coli* in a Memory-Like Manner. *Sci. Rep.* **9**, 3868 (2019).
330. Chimere, C., Field, C. M., Piñero-Fernandez, S., Keyser, U. F. & Summers, D. K. Indole prevents *Escherichia coli* cell division by modulating membrane potential. *Biochim. Biophys. Acta BBA - Biomembr.* **1818**, 1590–1594 (2012).
331. Gaimster, H., Cama, J., Hernández-Ainsa, S., Keyser, U. F. & Summers, D. K. The Indole Pulse: A New Perspective on Indole Signalling in *Escherichia coli*. *PLOS ONE* **9**, e93168 (2014).
332. Lee, H. H., Molla, M. N., Cantor, C. R. & Collins, J. J. Bacterial charity work leads to population-wide resistance. *Nature* **467**, 82–85 (2010).
333. Vega, N. M., Allison, K. R., Khalil, A. S. & Collins, J. J. Signaling-mediated bacterial persister formation. *Nat. Chem. Biol.* **8**, 431–433 (2012).
334. Bansal, T. *et al.* Differential Effects of Epinephrine, Norepinephrine, and Indole on *Escherichia coli* O157:H7 Chemotaxis, Colonization, and Gene Expression. *Infect. Immun.* **75**, 4597–4607 (2007).
335. Nikaido, E. *et al.* Effects of indole on drug resistance and virulence of *Salmonella enterica* serovar Typhimurium revealed by genome-wide analyses. *Gut Pathog.* **4**, 5 (2012).
336. Han, T. H., Lee, J.-H., Cho, M. H., Wood, T. K. & Lee, J. Environmental factors affecting indole production in *Escherichia coli*. *Res. Microbiol.* **162**, 108–116 (2011).
337. Yanofsky, C. RNA-based regulation of genes of tryptophan synthesis and degradation, in bacteria. *RNA* **13**, 1141–1154 (2007).
338. Deeley, M. C. & Yanofsky, C. Transcription initiation at the tryptophanase promoter of *Escherichia coli* K-12. *J. Bacteriol.* **151**, 942–951 (1982).
339. Bordi, C., Théraulaz, L., Méjean, V. & Jourlin-Castelli, C. Anticipating an alkaline stress through the Tor phosphorelay system in *Escherichia coli*: Identification of the Tor regulon. *Mol. Microbiol.* **48**, 211–223 (2003).
340. Zheng, D. Identification of the CRP regulon using in vitro and in vivo transcriptional profiling. *Nucleic Acids Res.* **32**, 5874–5893 (2004).
341. Li, G. & Young, K. D. A cAMP-independent carbohydrate-driven mechanism inhibits *tnaA* expression and TnaA enzyme activity in *Escherichia coli*. *Microbiology* **160**, 2079–2088 (2014).
342. Monod, J. The Growth of Bacterial Cultures. *Annu. Rev. Microbiol.* **3**, 371–394 (1949).
343. Lagier, J.-C. *et al.* Current and Past Strategies for Bacterial Culture in Clinical Microbiology. *Clin. Microbiol. Rev.* **28**, 208–236 (2015).

344. Cabeen, M. T. & Losick, R. Single-cell Microfluidic Analysis of *Bacillus subtilis*. *J. Vis. Exp. JoVE* 56901 (2018) doi:10.3791/56901.
345. Taheri-Araghi, S., Brown, S. D., Sauls, J. T., McIntosh, D. B. & Jun, S. Single-Cell Physiology. *Annu. Rev. Biophys.* **44**, 123–142 (2015).
346. Jong, I. G. de, Beilharz, K., Kuipers, O. P. & Veening, J.-W. Live Cell Imaging of *Bacillus subtilis* and *Streptococcus pneumoniae* using Automated Time-lapse Microscopy. *JoVE J. Vis. Exp.* e3145 (2011) doi:10.3791/3145.
347. Patange, O. *et al.* *Escherichia coli* can survive stress by noisy growth modulation. 265801 (2018) doi:10.1101/265801.
348. de Jong, I. G., Veening, J.-W. & Kuipers, O. P. Single cell analysis of gene expression patterns during carbon starvation in *Bacillus subtilis* reveals large phenotypic variation. *Environ. Microbiol.* **14**, 3110–3121 (2012).
349. El Meouche, I., Siu, Y. & Dunlop, M. J. Stochastic expression of a multiple antibiotic resistance activator confers transient resistance in single cells. *Sci. Rep.* **6**, 19538 (2016).
350. Sackmann, E. K., Fulton, A. L. & Beebe, D. J. The present and future role of microfluidics in biomedical research. *Nature* **507**, 181–189 (2014).
351. Norman, T. M., Lord, N. D., Paulsson, J. & Losick, R. Memory and modularity in cell-fate decision making. *Nature* **503**, 481–486 (2013).
352. Wang, P. *et al.* Robust growth of *Escherichia coli*. *Curr. Biol. CB* **20**, 1099–1103 (2010).
353. Baltekin, Ö., Boucharin, A., Tano, E., Andersson, D. I. & Elf, J. Antibiotic susceptibility testing in less than 30 min using direct single-cell imaging. *Proc. Natl. Acad. Sci. U. S. A.* **114**, 9170–9175 (2017).
354. Kaiser, M. *et al.* Monitoring single-cell gene regulation under dynamically controllable conditions with integrated microfluidics and software. *Nat. Commun.* **9**, 212 (2018).
355. Weibel, D. B., DiLuzio, W. R. & Whitesides, G. M. Microfabrication meets microbiology. *Nat. Rev. Microbiol.* **5**, 209–218 (2007).
356. Whitesides, G. M., Ostuni, E., Takayama, S., Jiang, X. & Ingber, D. E. Soft Lithography in Biology and Biochemistry. *Annu. Rev. Biomed. Eng.* **3**, 335–373 (2001).
357. Taheri-Araghi, S. *et al.* Cell-size control and homeostasis in bacteria. *Curr. Biol. CB* **25**, 385–391 (2015).
358. Amir, A., Babaeipour, F., McIntosh, D. B., Nelson, D. R. & Jun, S. Bending forces plastically deform growing bacterial cell walls. *Proc. Natl. Acad. Sci. U. S. A.* **111**, 5778–5783 (2014).
359. Kostylev, M., Otwell, A. E., Richardson, R. E. & Suzuki, Y. Cloning Should Be Simple: *Escherichia coli* DH5 $\alpha$ -Mediated Assembly of Multiple DNA Fragments with Short End Homologies. *PLOS ONE* **10**, e0137466 (2015).
360. Baba, T. *et al.* Construction of *Escherichia coli* K-12 in-frame, single-gene knockout mutants: the Keio collection. *Mol. Syst. Biol.* **2**, 2006.0008 (2006).
361. Gaimster, H. & Summers, D. Regulation of Indole Signalling during the Transition of *E. coli* from Exponential to Stationary Phase. *PLOS ONE* **10**, e0136691 (2015).

362. Kotte, O., Volkmer, B., Radzikowski, J. L. & Heinemann, M. Phenotypic bistability in *Escherichia coli*'s central carbon metabolism. *Mol. Syst. Biol.* **10**, 736 (2014).
363. Gibson, D. G. *et al.* Creation of a Bacterial Cell Controlled by a Chemically Synthesized Genome. *Science* **329**, 52–56 (2010).
364. Untergasser, A. *et al.* Primer3Plus, an enhanced web interface to Primer3. *Nucleic Acids Res.* **35**, W71–W74 (2007).
365. Goode, O. *et al.* Persister *Escherichia coli* Cells Have a Lower Intracellular pH than Susceptible Cells but Maintain Their pH in Response to Antibiotic Treatment. *mBio* (2021) doi:10.1128/mBio.00909-21.
366. Hochbaum, D. R. *et al.* All-optical electrophysiology in mammalian neurons using engineered microbial rhodopsins. *Nat. Methods* **11**, 825–833 (2014).
367. Shen, Y. *et al.* Genetically encoded fluorescent indicators for imaging intracellular potassium ion concentration. *Commun. Biol.* **2**, 1–10 (2019).
368. Mattis, J. *et al.* Principles for applying optogenetic tools derived from direct comparative analysis of microbial opsins. *Nat. Methods* **9**, 159–172 (2012).
369. Shen, Y., Rosendale, M., Campbell, R. E. & Perrais, D. pHuji, a pH-sensitive red fluorescent protein for imaging of exo- and endocytosis. *J. Cell Biol.* **207**, 419–432 (2014).
370. Dammeyer, T., Timmis, K. N. & Tinnefeld, P. Broad host range vectors for expression of proteins with (Twin-) Strep-tag, His-tag and engineered, export optimized yellow fluorescent protein. *Microb. Cell Factories* **12**, 49 (2013).
371. Si, F. *et al.* Invariance of Initiation Mass and Predictability of Cell Size in *Escherichia coli*. *Curr. Biol.* **27**, 1278–1287 (2017).
372. Arganda-Carreras, I. *et al.* Trainable Weka Segmentation: a machine learning tool for microscopy pixel classification. *Bioinformatics* **33**, 2424–2426 (2017).
373. Tinevez, J.-Y. *et al.* TrackMate: An open and extensible platform for single-particle tracking. *Methods* **115**, 80–90 (2017).
374. Eren, E. *et al.* Substrate Specificity within a Family of Outer Membrane Carboxylate Channels. *PLOS Biol.* **10**, e1001242 (2012).
375. Cama, J. *et al.* Single-cell microfluidics facilitates the rapid quantification of antibiotic accumulation in Gram-negative bacteria. *Lab. Chip* **20**, 2765–2775 (2020).
376. Jarzembowski, T., Wiśniewska, K., Józwiak, A., Bryl, E. & Witkowski, J. Flow Cytometry as a Rapid Test for Detection of Penicillin Resistance Directly in Bacterial Cells in *Enterococcus faecalis* and *Staphylococcus aureus*. *Curr. Microbiol.* **57**, 167–169 (2008).
377. Hamilton, K. E., Bouwer, M. F., Louters, L. L. & Looyenga, B. D. Cellular binding and uptake of fluorescent glucose analogs 2-NBDG and 6-NBDG occurs independent of membrane glucose transporters. *Biochimie* **190**, 1–11 (2021).
378. Jeon, A. B. *et al.* 2-aminoimidazoles potentiate  $\beta$ -lactam antimicrobial activity against *Mycobacterium tuberculosis* by reducing  $\beta$ -lactamase secretion and increasing cell envelope permeability. *PLOS ONE* **12**, e0180925 (2017).
379. Fenno, L., Yizhar, O. & Deisseroth, K. The Development and Application of Optogenetics. *Annu. Rev. Neurosci.* **34**, 389–412 (2011).
380. Nagata, T. *et al.* The counterion–retinylidene Schiff base interaction of an invertebrate rhodopsin rearranges upon light activation. *Commun. Biol.* **2**, 1–9 (2019).

381. Volkmer, B. & Heinemann, M. Condition-Dependent Cell Volume and Concentration of *Escherichia coli* to Facilitate Data Conversion for Systems Biology Modeling. *PLOS ONE* **6**, e23126 (2011).
382. New England Biolabs. High Efficiency Transformation Protocol (C2987H) v1. doi:10.17504/protocols.io.chgt3v.
383. Olsson, M. H. M., Søndergaard, C. R., Rostkowski, M. & Jensen, J. H. PROPKA3: Consistent Treatment of Internal and Surface Residues in Empirical pKa Predictions. *J. Chem. Theory Comput.* **7**, 525–537 (2011).
384. Westfall, D. A. *et al.* Bifurcation kinetics of drug uptake by Gram-negative bacteria. *PLOS ONE* **12**, e0184671 (2017).
385. Lang, Y. *et al.* Combating Multidrug-Resistant Bacteria by Integrating a Novel Target Site Penetration and Receptor Binding Assay Platform Into Translational Modeling. *Clin. Pharmacol. Ther.* **109**, 1000–1020 (2021).
386. Coldham, N. G., Webber, M., Woodward, M. J. & Piddock, L. J. V. A 96-well plate fluorescence assay for assessment of cellular permeability and active efflux in *Salmonella enterica* serovar Typhimurium and *Escherichia coli*. *J. Antimicrob. Chemother.* **65**, 1655–1663 (2010).
387. Chow, B. Y. *et al.* High-Performance Genetically Targetable Optical Neural Silencing via Light-Driven Proton Pumps. *Nature* **463**, 98–102 (2010).
388. Natarajan, A. & Srienc, F. Dynamics of Glucose Uptake by Single *Escherichia coli* Cells. *Metab. Eng.* **1**, 320–333 (1999).
389. Khandogin, J. & Brooks, C. L. Constant pH Molecular Dynamics with Proton Tautomerism. *Biophys. J.* **89**, 141–157 (2005).
390. Kots, E., Shore, D. M. & Weinstein, H. An equilibrium constant pH molecular dynamics method for accurate prediction of pH-dependence in protein systems: Theory and application. 2020.11.23.394015  
<https://www.biorxiv.org/content/10.1101/2020.11.23.394015v1> (2020)  
 doi:10.1101/2020.11.23.394015.
391. Swails, J. M., York, D. M. & Roitberg, A. E. Constant pH Replica Exchange Molecular Dynamics in Explicit Solvent Using Discrete Protonation States: Implementation, Testing, and Validation. *J. Chem. Theory Comput.* **10**, 1341–1352 (2014).
392. Huang, Y., Henderson, J. A. & Shen, J. Continuous constant pH Molecular Dynamics Simulations of Transmembrane Proteins. *Methods Mol. Biol. Clifton NJ* **2302**, 275–287 (2021).
393. de Me & Cedex, M.-S.-A. Alteration of pore properties of *Escherichia coli* OmpF induced by mutation of key residues in anti-loop 3 region. **8** (2002).
394. Nikaido, H. Molecular Basis of Bacterial Outer Membrane Permeability Revisited. *Microbiol. Mol. Biol. Rev.* **67**, 593–656 (2003).
395. Dodd, B. J. T. & Kralj, J. M. Live Cell Imaging Reveals pH Oscillations in *Saccharomyces cerevisiae* During Metabolic Transitions. *Sci. Rep.* **7**, 13922 (2017).
396. Dammeyer, T. Biomedicals from a soil bug: Expanding scFv production host range. *Bioengineered* **3**, 67–71 (2012).

397. Zilberstein, D., Schuldiner, S. & Padan, E. Proton electrochemical gradient in *Escherichia coli* cells and its relation to active transport of lactose. *Biochemistry* **18**, 669–673 (1979).
398. Ramos, S., Schuldiner, S. & Kaback, H. R. The electrochemical gradient of protons and its relationship to active transport in *Escherichia coli* membrane vesicles. *Proc. Natl. Acad. Sci.* **73**, 1892–1896 (1976).
399. Booth, I. R. Regulation of cytoplasmic pH in bacteria. *MICROBIOL REV* **49**, 20 (1985).
400. Krulwich, T. A., Sachs, G. & Padan, E. Molecular aspects of bacterial pH sensing and homeostasis. *Nat. Rev. Microbiol.* **9**, 330–343 (2011).
401. Slonczewski, J. L., Rosen, B. P., Alger, J. R. & Macnab, R. M. pH homeostasis in *Escherichia coli*: measurement by <sup>31</sup>P nuclear magnetic resonance of methylphosphonate and phosphate. *Proc. Natl. Acad. Sci.* **78**, 6271–6275 (1981).
402. Brooks, M., E. *et al.* glmmTMB Balances Speed and Flexibility Among Packages for Zero-inflated Generalized Linear Mixed Modeling. *R J.* **9**, 378 (2017).
403. Kuo, M. M.-C., Saimi, Y. & Kung, C. Gain-of-function mutations indicate that *Escherichia coli* Kch forms a functional K<sup>+</sup> conduit in vivo. *EMBO J.* **22**, 4049–4058 (2003).
404. Dammeyer, T. & Tinnefeld, P. Engineered fluorescent proteins illuminate the bacterial periplasm. *Comput. Struct. Biotechnol. J.* **3**, e201210013 (2012).
405. Dammeyer, T. & Tinnefeld, P. Engineered fluorescent proteins illuminate the bacterial periplasm. *Comput. Struct. Biotechnol. J.* **3**, e201210013 (2012).
406. Yang, M. *et al.* Biocompatible click chemistry enabled compartment-specific pH measurement inside *E. coli*. *Nat. Commun.* **5**, 4981 (2014).
407. O’Neill, J. Tackling drug-resistant infections globally: final report and recommendations. <https://apo.org.au/node/63983> (2016).
408. Cama, J., Henney, A. M. & Winterhalter, M. Breaching the Barrier: Quantifying Antibiotic Permeability across Gram-negative Bacterial Membranes. *J. Mol. Biol.* **431**, 3531–3546 (2019).
409. Lopatkin, A. J. *et al.* Clinically relevant mutations in core metabolic genes confer antibiotic resistance. *Science* **371**, eaba0862 (2021).
410. Lopatkin, A. J. *et al.* Bacterial metabolic state more accurately predicts antibiotic lethality than growth rate. *Nat. Microbiol.* **4**, 2109–2117 (2019).
411. Dai, J., Suh, S.-J., Hamon, M. & Hong, J. W. Determination of antibiotic EC50 using a zero-flow microfluidic chip based growth phenotype assay. *Biotechnol. J.* **10**, 1783–1791 (2015).
412. Methods for dilution antimicrobial susceptibility tests for bacteria that grow aerobically: M07-A10 ; approved standard. (Committee for Clinical Laboratory Standards, 2015).
413. Ritz, C., Baty, F., Streibig, J. C. & Gerhard, D. Dose-Response Analysis Using R. *PLOS ONE* **10**, e0146021 (2015).
414. Baudry-Simner, P. J., Singh, A., Karlowsky, J. A., Hoban, D. J. & Zhanel, G. G. Mechanisms of reduced susceptibility to ciprofloxacin in *Escherichia coli* isolates from Canadian hospitals. *Can. J. Infect. Dis. Med. Microbiol.* **23**, e60–e64 (2012).
415. Choi, U. & Lee, C.-R. Distinct Roles of Outer Membrane Porins in Antibiotic Resistance and Membrane Integrity in *Escherichia coli*. *Front. Microbiol.* **10**, 953 (2019).

416. Cama, J., Chimere, C., Pagliara, S., Javer, A. & Keyser, U. F. A label-free microfluidic assay to quantitatively study antibiotic diffusion through lipid membranes. *Lab. Chip* **14**, 2303–2308 (2014).
417. Smirnova, G. V. & Oktyabrsky, O. N. Relationship between *Escherichia coli* growth rate and bacterial susceptibility to ciprofloxacin. *FEMS Microbiol. Lett.* **365**, fnx254 (2018).
418. Meylan, S. *et al.* Carbon Sources Tune Antibiotic Susceptibility in *Pseudomonas aeruginosa* via Tricarboxylic Acid Cycle Control. *Cell Chem. Biol.* **24**, 195–206 (2017).
419. Solopova, A. *et al.* Bet-hedging during bacterial diauxic shift. *Proc. Natl. Acad. Sci.* **111**, 7427–7432 (2014).
420. Hartline, C. J., Zhang, R. & Zhang, F. Transient Antibiotic Tolerance Triggered by Nutrient Shifts From Gluconeogenic Carbon Sources to Fatty Acid. *Front. Microbiol.* **13**, (2022).
421. Shapiro, H. M. Flow Cytometry of Bacterial Membrane Potential and Permeability. in *New Antibiotic Targets* (ed. Champney, W. S.) 175–186 (Humana Press, 2008). doi:10.1007/978-1-59745-246-5\_14.
422. Goode, O. *et al.* Persister *Escherichia coli* Cells Have a Lower Intracellular pH than Susceptible Cells but Maintain Their pH in Response to Antibiotic Treatment. *mBio* (2021) doi:10.1128/mBio.00909-21.
423. Sankaranarayanan, S., De Angelis, D., Rothman, J. E. & Ryan, T. A. The Use of pHluorins for Optical Measurements of Presynaptic Activity. *Biophys. J.* **79**, 2199–2208 (2000).
424. Shapiro, H. M. *Practical Flow Cytometry*. (Wiley, 2003). doi:10.1002/0471722731.
425. Novo, D., Perlmutter, N. G., Hunt, R. H. & Shapiro, H. M. Accurate flow cytometric membrane potential measurement in bacteria using diethyloxycarbocyanine and a ratiometric technique. *Cytometry* **35**, 55–63 (1999).
426. Kuwada, N. J., Traxler, B. & Wiggins, P. A. Genome-scale quantitative characterization of bacterial protein localization dynamics throughout the cell cycle. *Mol. Microbiol.* **95**, 64–79 (2015).
427. Torres Cabán, C. C. *et al.* Tuning the sensitivity of genetically encoded fluorescent potassium indicators through structure-guided and genome mining strategies. <http://biorxiv.org/lookup/doi/10.1101/2021.10.07.463355> (2021) doi:10.1101/2021.10.07.463355.
428. Gengenbacher, M. & Kaufmann, S. H. E. *Mycobacterium tuberculosis*: success through dormancy. *FEMS Microbiol. Rev.* **36**, 514–532 (2012).
429. Lewis, K. Persister Cells. *Annu. Rev. Microbiol.* **64**, 357–372 (2010).